The Role of MYO7A in Tuning Sensory Hair Cell Sensitivity

Sihan Li
Shijiazhuang, Hebei, China

M.S. Biological and Physical Sciences, University of Virginia, 2021
B.S. Biotechnology, Hebei Normal University, 2015

A Dissertation presented to the Graduate Faculty
of the University of Virginia in Candidacy for the Degree of
Doctor of Philosophy

Dissertation committee member:
Dr. Hao Jiang (Chair)
Dr. Jung-Bum Shin
Dr. Edward Egelman
Dr. Xiaowei Lu

Department of Biochemistry and Molecular Genetics
University of Virginia
May 2023

Abstract:

Hair cells, the sensory receptors of the auditory and vestibular system, transduce mechanical stimuli from sound and head movement into an electrochemical signal. The mechanosensory hair bundle, consisting of an array of elongated microvilli called stereocilia, harbors the mechano-electrical transduction complex (MET). The tip link, an extracellular filament bridging two adjacent stereocilia, connects the MET channel complex at its lower end with the side of the stereocilium in the next tallest row. Deflection of the hair bundle increases tension in the tip links, which opens MET channels at its lower end, leading to the hair cell depolarization of hair cells. Thus, setting up the correct amount of tip-link tension is essential for the sensitivity of and dynamic range of auditory hair cells.

The upper end of the tip link is hypothesized to house a tension-generating element that anchors and pulls the tip link upwards along the F-actin core. Several myosin motors have been proposed to fulfill this function, and one of the candidates is an unconventional myosin - myosin-VIIa (MYO7A). However, functional evidence establishing MYO7A as the tension generator has been challenging to obtain, because hair bundle development is affected in knockout and knockdown mouse models of MYO7A, precluding isolated loss-of-function analyses.

Our study provided evidence that MYO7A is the molecular motor that tensions the MET complex. We further discovered that MYO7A is expressed in two major isoforms with unique N-terminal extensions. These isoforms are differentially expressed in inner and outer hair cells (IHCs and OHCs), correlating with reported differences in tip-link tension. This differential expression pattern of MYO7A isoforms with distinct motor properties might contribute to the tip-link tension variability in different population of hair cells, with potential importance for establishing the remarkable frequency range of mammalian hearing. Last, we identified novel regulatory elements for *Myo7a* expression, providing the mechanism of the differential expression pattern of MYO7A isoforms in auditory hair cells.

Acknowledgment

I have been always grateful to my advisor Dr. Jung-Bum Shin for the mentorship that he gave me over the past 7 years. For me, Dr. Shin is more than a great scientist, a team leader, and a mentor. He is a father to my scientific career and adventure in the U.S. Dr. Shin is always supportive and encouraging: he never rejects a crazy idea that I want to test, and never turns down a bad result from my experiment and my bad writing. You gave me invaluable support, advice and courage to pursue a career path that I like. Here, I really would like to say one more time:" Thank you, Boss!"

I also want to thank to Dr. Xiaowei Lu and Dr. Jeffery Corwin for teaching me knowledge of the inner ear field. You are really great mentors and it is lucky to be your student. Also many thanks to my dissertation committee members: Dr. Edward Egelman, and Dr. Hao Jiang for the great guidance for my study. Thanks to our collaborators: Dr. Anthony Peng, Dr. Jonathan Bird, and Dr. Bechara Kachar (and their team members). I could not finish my research without your help.

I will never forget the time I spent with amazing Shin lab members: Tingting, Beth, Saman, Jun-Sub, Kat, Ted, David, and Super Dan. Thank you for the skills that you taught, the ideas that you shared, and the joyful lab environment that you created. Tingting, you are my teacher of many techniques. Beth, you are a true friend that is always cheerful and supportive. And thanks to Andre and Shaylyn from Lu lab and Mark from Corwin lab. It is so great to have wonderful friends like you. Jeewoo and Tobey, I always enjoy working with you, and thanks for your hard work on our projects. Best wishes for your future careers.

Many thanks to the Department of Biochemistry and Molecular Genetics, the Department of Neuroscience, and the Center for Brain Immunology and Glia. Thank you for providing all the resources and support for my study and research. And thanks to the department administrators: Debra Site, William Garmer, Tesha Westbrook, Wendy Baker, and Margaret Heine. For all the events you arranged, and all the support you gave me. Thanks to my friends Kevin Cox, Chantile Bailey, Chao Guo, Fengjiao Li, and Yinyu Wu. You always got my back for the struggling moments that I had. I will always remember the time that we spent in Charlottesville.

Last, I would like to thank my family, especially my parents, Xiaoyan and Hui, for all the support that you gave me. I could never have had a chance to study abroad without open-minded parents like you. Always love you! (And Prince.)

Contents

1. Chapter 1: Introduction 1

1.1. Overview of hair cells and mechano-electrical transduction 1

1.1.1. Sound and the sound-detecting cochlea 1

1.1.2. Sensory hair cells 1

1.1.3. Two types of hair cells in the mammalian cochlea. 2

1.1.4. Tonotopy of cochlear hair cells 3

1.1.5. Hair cell mechano-electrical transduction 4

1.1.6. The molecular identity of the tip link 5

1.2. Myosins and their function in the auditory epithelium 6

1.2.1. Myosin and its powerstroke cycle 6

1.2.2. Function of unconventional myo7a: myosin-VIIa 7

2. Chapter 2: Method: 9

2.1. Animal care and handling 9

2.2. Generation of *Myo7a-ΔC*, *Myo7a-ΔN*, *Myo7a-ΔS*, *Myo7a-ΔCN*, *Myo7a* full KO, *HA-Myo7a-N*, *HA-Myo7a-C*, and *Myo7a-ΔEnhancerA* mice: 9

2.3. Immunofluorescence 12

2.4. Hearing tests in mice 13

2.5. Whole-cell voltage-clamp electrophysiology recordings 14

2.5.1. Animals: 14

2.5.2. Electrophysiological recordings: 14

2.5.3. Hair bundle stimulation and motion recording: 15

2.5.4. Analysis: 15

2.5.5. Hair bundle motion analysis: 15
2.5.6. Electrophysiological data analysis:....16
2.5.7. Analysis of MET current and hair bundle rise kinetics: 16
2.6. Scanning electron microscopy 17
2.7. Stereocilia Length Quantification: 17
2.7.1. Details of the calculation of the length of fully visible stereocilia, tilted in any direction: 18
2.7.2. Calculation of the length of stereocilia with obstructed bases:....19
3. Chapter 3: Myosin-VIIa is expressed in multiple isoforms and essential for tensioning the hair cell mechanotransduction complex....23
3.1. Multiple isoforms of MYO7A are expressed in the organ of Corti 23
3.2. Deletion of MYO7A-C primarily affects MYO7A in cochlear IHCs 26
3.3. Reduced MYO7A levels at the UTLD and stereocilia base of *Myo7a-ΔC* IHCs....33
3.4. Harmonin and ADGRV1 localization is not decreased in *Myo7a-ΔC* IHCs....37
3.5. Reduced MET resting open probability and slowed MET current kinetics in *Myo7a-ΔC* IHCs 40
3.6. *Myo7a-ΔC* mice exhibit progressive elevation of ABR thresholds, while DPOAE output is unaffected. 46
3.7. Transducing rows of IHC stereocilia degenerate in *Myo7a-ΔC* mice....50
4. Chapter 4: Identification of a novel isoform of *Myo7a* in sensory hair cells....51
4.1. Survey of novel *Myo7a* isoform:....51
4.2. MYO7A-C and MYO7A-N are major isoforms in the cochlea: 55
4.3. Expression of *Myo7a-C* and *Myo7a-N* are inversely correlated in the cochlea. 60
4.4. MYO7A-C and MYO7A-N localize to UTLDs of IHCs and OHCs: 63

4.5. Hearing function deterioration and hair cell loss of adult *Myo7a-ΔN* mice. 67

5. Chapter 5: Identification of new regulatory mechanisms of *Myo7a*. 70

5.1. Revisiting published regulatory mechanisms of MYO7A 70

5.2. The identification of new MYO7A gene regulatory units. 73

5.3. SIX2 – a transcription factor potentially regulates *Myo7a* expression 77

5.4. SIX2 is important for hair cell maintenance. 80

6. Chapter 6: Discussion and future directions 84

6.1. Identification of MYO7A isoforms in cochlear hair cells. 84

6.2. *Myo7a* is essential for tensioning the MET complex. 85

6.3. Function of MYO7A-N isoform in the auditory system. 89

6.4. Functional difference between MYO7A-C and MYO7A-N isoforms 90

6.5. Expression regulation of *Myo7a* isoforms 92

6.5.1. Regulatory mechanism of MYO7A-C isoform 92

6.5.2. Regulatory mechanism of MYO7A-N isoform 92

6.5.3. *EnhancerA*, a newly discovered enhancer of *Myo7a*. 93

6.5.4. The function of SIX2 in *Myo7a* expression and hair cell maintenance. 94

Abbreviations: 97

References: 101

1. Chapter 1: Introduction

1.1. Overview of hair cells and mechano-electrical transduction

1.1.1. Sound and the sound-detecting cochlea

A vibrating object causes compression and rarefaction of its surrounding medium (air, water, etc.). The resulting vibrations, termed sound, are propagated in a sinusoidal mechanical wave. Animals have evolved diverse sensory apparatuses for detecting environmental sounds, which are critical for communication, prey-seeking, and predator evasion. The sound-sensing organ in mammals, the cochlea, can detect sound with a remarkable range of intensities and frequencies. For example, the human cochlea can detect sound with a frequency range from 20 to 20000 Hz and a high dynamic intensity range of up to 120dB. The function of the cochlea is essential for daily life, allowing us to do everything from appreciating music to communicating with others.

1.1.2. Sensory hair cells

Hair cells, the sensory receptors of the inner ear, convert mechanical vibrations into electrochemical signals, which are then transmitted through the auditory pathway to the auditory cortex. Hair cells are present in the cochlea and vestibular system, varying in shapes, sensitivities, and molecular components. However, these different types of hair cells utilize the same fundamental mechanism to respond to mechanical stimulations, a process called mechano-electrical transduction (MET). Critical to the hair cell's MET is the mechanosensory hair bundle located at its apical surface. The hair bundle is modeled as a series of stereocilia, arranged at different heights to form a staircase-like structure[1], which gives the hair cell the ability to respond to a mechanical deflection of its hair bundle in a directional manner.

1.1.3. Two types of hair cells in the mammalian cochlea.

The human and mouse organ of Corti, the auditory receptor organ located in the cochlea, harbors three rows of outer hair cells (OHCs) and one row of inner hair cells (IHCs). These two types of hair cells have distinct functions in hearing. IHCs are the principal sound receptors of the cochlea. The deflection of their hair bundles leads to the depolarization of the cell body, and this electrical signal is transmitted along the auditory pathway to the auditory cortex for subjective perception of sound. OHCs have an assistive yet critical role in the audition. They are essential for a process called cochlear amplification, which is an active mechanical feedback process that contributes to a higher sensitivity to sound and sharpened frequency tuning[2,3]. Disruption of OHC function results in a 40~50dB reduction in mouse hearing[4]. The protein Prestin was identified as the molecular motor enabling OHC electromotility[5,6]. Prestin undergoes a series of conformational changes in response to sound-induced depolarization-hyperpolarization cycles. This process leads to contraction-relaxation cycles of the OHC cell body along the longitudinal axis, feeds back into the motion of the basilar membrane, and enhances its vibration[5,7,8]. The OHC-amplified vibration in turn stimulates the hair bundles of IHCs.

IHCs and OHCs differ in many aspects, such as hair bundle morphology, stereocilia length and diameter, and properties of the MET complex (channel conductance, calcium permeability, maximum current, etc.)[9–11]. It was shown that OHCs have higher resting open probability and gating spring stiffness than IHCs; this suggests that OHCs are more readily activated and have a higher current response to specific amounts of force[12].

1.1.4. Tonotopy of cochlear hair cells

Tonotopy refers to the spatial arrangement of cells in the auditory system, such as hair cells and spiral ganglia neurons in the cochlea and the neurons in the brainstem and auditory cortex. This spatial organization of cells is essential for the frequency-specific detection of sound. In the cochlea, the basal region is responsible for high-frequency hearing, and the apex is geared toward low-frequency hearing[13–16]. In the mammalian organ of Corti, hair cells are located on top of a resonant structure called the basilar membrane. The basilar membrane's stiffness and width vary along the tonotopic axis of the cochlea, its stiffness decreasing from the base to the apex of the cochlea. This gradient in stiffness and width allows the basilar membrane to resonate in a frequency-dependent manner, in that only a certain region of the basilar membrane will have the highest amplitude of vibration in response to specific frequencies. Although the aforementioned physical properties and the resulting resonant gradient along the basilar membrane are the primary mechanism underlying tonotopy, other factors, also referred to as additional filters, are believed to contribute to sharpening the frequency selectivity of auditory detection. For example, basal hair cells are shown to have shorter stereocilia[9,17], stiffer hair bundle rigidity[12], and higher tip-link tension than hair cells at the apex region[10–12]. These properties of the basal hair cells are believed to represent an adaptation for their high-frequency sound perception.

The developmental establishment of the tonotopy in the cochlea and other parts of the auditory pathway is a topic of active research. For example, BMP7 and retinoic acid signaling pathways regulate the tonotopic pattern of chicken basilar papilla[18,19]. The Sonic-hedgehog pathway is also essential for the temporal formation of the cochlea tonotopy, and the disruption of this pathway results in shortened cochlea duct and underdevelopment of hair cells[20,21]. In the spiral ganglia neurons, ISL regulates the neurogenesis, migration, and the formation of the tonotopic patterns[22].

1.1.5. Hair cell mechano-electrical transduction

Much of the hair bundle's structural beauty derives from its clear reflection of its function. Pickles' discovery of the tip link[23], which connected the tips of the shorter stereocilium with the side of its next taller stereocilium, allowed the pioneering work by Flock, Hudspeth, and others to crystallize into a working model for hair cell[24–28]. In this model, the tip link is connected to a stretch-sensitive ion channel complex, and deflection of the hair bundle along the axis of the tip link initiates MET. Initially, based on calcium imaging studies with inadequate temporal and spatial resolution, it was believed that the MET channel complex is located at both sides of the tip link[29,30]. In 2009, however, Beurg et al. used high-speed calcium imaging and observed that the Ca^{2+} signal first appears at the tips of the stereocilia upon hair bundle deflection, indicating that the MET channel is localized only at the lower end of the tip link[31] (or the tips of the shorter stereocilia). Their study provided the start signal and correct qualifying criteria for the molecular characterization of the hair cell MET complex.
With the advent of powerful human and mouse genetic studies and targeted candidate approaches, multiple proteins crucial for MET were identified. Most importantly, it is now well-accepted that TMC1/2 is the pore-forming subunit of the MET channel[32,33]. Besides TMC1/2, other auxiliary proteins have also been shown to have essential roles in the MET process; TMIE is a crucial subunit of the MET channel, defining the gating properties of the channel[34,35]. CIB2/3 are auxiliary subunits of the MET channel, essential for the function and localization of the MET channel complex[36–38]. LHFPL5 is an integral component of the MET complex[39,40]. LHFPL5 is shown to interact with TMC1/2 and PCDH15, which is proposed to serve as the connection between the core-forming subunits of the MET channel and the tip link[41,42]. Deletions or mutations of these genes are known to cause severe MET defects of hair cells and profound hearing loss in humans and mice

1.1.6. The molecular identity of the tip link

Early electron microscopy imaging studies have discovered that different types of stereociliary links connect stereocilia with each other. These extracellular links contribute to the hair bundle's stiffness and synchronize stereocilia's movement upon stimulation. Most importantly, the tip link connects the MET channel complex to the lateral side of the adjacent taller stereocilium[23,43]. The tip link consists of two types of cadherin family proteins: protocadherin15 (PCDH15)[44–46] and cadherin23 (CDH23)[47,48], which form a double-stranded extracellular protein filament[49,50]. PCDH15 is at the lower part of the tip link, which is connected to the MET channel by a protein named LHFPL5[39,40]. CDH23 is the upper part of the tip link, which is connected to the lateral side of the next taller stereocilium. Each PCDH15 and CDH23 forms a homodimer and interacts with each other at their C-terminus end through a "handshake" interaction[49–52]. The tip link is under tonic tension at the resting stage, which is important for the properties of the MET channels. Upon the deflection of the hair bundle in the excitatory direction towards the longer end of the hair bundle, tip-link tension increases and further activates the mechanically gated MET channels. Tip-link tension at the resting state is therefore crucial for the sensitivity of hair cell MET. For example, OHCs are shown to have a higher tip-link tension, of which the MET channels are more readily activated than IHCs[12].

At the upper end of the tip link is the so-called upper tip link density (UTLD)[23,53–56]. This protein complex is believed to be the anchor site of the tip link to the F-actin core of stereocilia. According to the prevailing model, the UTLD contains a motor complex that pulls the tip link and the MET complex on the other side upwards, thus setting up the tip-link tension. Recent studies have shown that Harmonin and Sans serve as scaffold proteins in UTLDs, which directly connect the N-terminus of CDH23 to the stereocilium F-actin core[57–60]. However, the molecular identity of the most critical part of the UTLD –

the molecular motor – remained unresolved. Because the stereocilia core consists of F-actin, it was suspected that this function must be fulfilled by a myosin.

1.2. Myosins and their function in the auditory epithelium

1.2.1. Myosin and its powerstroke cycle

Myosins belong to a superfamily of cytoskeleton motor proteins. The motor domain of myosin has actin binding sites, allowing it to translocate on actin filaments[58]. The motor domain of myosin also has ATPase activity; upon the hydrolysis of ATP, the motor domain undergoes a series of conformational changes, which convert the chemical energy into mechanical movements. The process is known as the "powerstroke cycle" of myosin[61–64]. All myosins share the same powerstroke cycles but have different biochemical rates for each step, allowing different types of myosins to fine-tune their motor activities. The diversity of myosin motor biochemical properties contributes to various cellular functions, such as vesicle transport, cell migration, and cell signaling [63–66].

The first myosin discovered was myosin II is the first discovered myosin by Kühne in the skeleton muscle at 1864[67]. It is the most extensively studied myosin is highly expressed in the sarcomere and essential for skeleton muscle contraction. Besides myosin II, around 40 different types of myosin have been identified in the human genome. All myosins other than myosin-II are clustered into a group of unconventional myosins[67,68]. Unconventional myosins differ in many aspects, including motor domain activities, cargos, and cellular functions. Notably, several unconventional myosins are known to be essential for auditory hair cell functions[64]. At least nine types of myosin proteins have been identified in hair cells, and six are linked to hearing loss[64,69]. For example, myosin-XVa (MYO15) is shown to regulate the length of the stereocilia, and the mutations of MYO15a cause a reduction in the length of stereocilia[70–72]. Myosin-III (MYO3) is also

shown to be localized to the stereocilia tip, which regulates the length of stereocilia and the formation of the staircase-like structure of the hair bundle by transporting espin[73–75]. Myosin Ic (MYO1C) was proposed to be the motor protein responsible for the slow adaptation in vestibular hair cells[76–81]. However, this function is challenged by a recent study which suggests that other factors maybe also involved in slow adaptation[82]. Moreover, the mutation of many other unconventional myosins (i.e., myosin-VI[83–85] and myosin-IX[86,87]) are shown to cause deafness, but their function remains to be explored. Overall, multiple studies have shown the functional significance of unconventional myosins in auditory hair cells[88].

1.2.2. Function of unconventional myo7a: myosin-VIIa

Usher syndrome is the most common deaf-blindness disease in humans. The most severe type of Usher syndrome (type I) is characterized by congenital hearing loss, early onset vision loss, and deterioration of balance[89,90]. Multiple genes are identified to be responsible for Usher syndrome type I, and most of these genes encode MET complex proteins such as TMIE, Sans[91,92], and Harmonin[93]. One of these genes, USH1B, accounts for about 75% of Usher syndrome type I cases[94]. In 1995, Christine Petit Lab first reported that this deafness gene encodes an unconventional myosin – myosin VIIA (MYO7A)[94]. MYO7A is involved in multiple functions in hair cells, including hair bundle development, planar cell polarity, and MET of hair cells. The deletion of MYO7A results in hair bundle disorganization, making it difficult to study the role of MYO7A in the MET complex[95].

Over the past decades, intensive studies have been conducted to investigate the function of MYO7A in the MET complex hair cells. In 2011, M'hamed et al. showed that MYO7A, Sans, and Harmonin are localized to UTLDs of cochlea and utricle hair cells[57]. In 2017, a structural analysis from I-Mei et al. showed that MYO7A forms a triplex with

San and Harmonin. This protein complex directly connects CDH23 to the F-actin core of stereocilium[58]. One recent study revealed that the loss of MYO7A in mature IHC results in a reduction of MET sensitivity[96]. These results are consistent with the prevalent hypothesis that MYO7A is the motor protein that generates tip-link tension at UTLD. However, the critical evidence to answer this question was still missing. In my work, I made the unexpected discovery that IHCs and OHCs preferentially express different isoforms of the candidate tip-link motor protein MYO7A. Analysis of isoform-specific KO and KI mice provided evidence for a direct role of MYO7A in tensioning the hair cell MET complex.

2. Chapter 2: Method:

2.1. Animal care and handling

The care and use of animals for all experiments described conformed to NIH guidelines. Experimental mice were housed in a 12:12 hour light:dark cycle with free access to chow and water in standard laboratory cages in a temperature and humidity-controlled vivarium. The protocols for the care and use of animals were approved by the Institutional Animal Care and Use Committees at the University of Virginia, the University of Colorado Denver, and the National Institute on Deafness and Other Communication Disorders. All the institutions mentioned above are accredited by the American Association for the Accreditation of Laboratory Animal Care. C57BL/6J (Bl6, from Jackson Laboratory, ME, USA) mice and sibling mice served as control mice for this study. Neonatal mouse pups (P0–P5) were sacrificed by rapid decapitation. Mature mice were euthanized by CO_2 asphyxiation followed by cervical dislocation. The *Myo7a::beta-actin-GFP* mouse line expressing beta-actin-GFP from a *Myo7a* BAC transgene[97,98] was a gift from Dr. Haydn Prosser (Wellcome Trust Sanger Institute, UK).

2.2. Generation of *Myo7a-ΔC*, *Myo7a-ΔN*, *Myo7a-ΔS*, *Myo7a-ΔCN*, *Myo7a* full KO, *HA-Myo7a-N*, *HA-Myo7a-C*, and *Myo7a-ΔEnhancerA* mice:

For CRISPR/Cas mediated generation of the mouse models, we used the online tool CRISPR (http://crispor.tefor.net/crispor.py)[99] to select suitable target sequences to ablate *Myo7a* isoforms. To generate the corresponding single-guide (sg)RNAs, a PCR product from overlapping oligonucleotides (as described in the CRISPR online tool) was generated by T7 in vitro transcription. In vitro transcription was performed using the MAXIscript T7 kit (Life Technologies), and RNA was purified using the MEGAclear kit (Thermo Fisher

Scientific, Waltham, MA). To produce genetically engineered mice, fertilized eggs were coinjected with Cas9 protein (PNA Bio, 50 ng/μl) and the sgRNA (30 ng/μl). Two-cell stage embryos were implanted on the following day into the oviducts of pseudopregnant ICR female mice (Envigo). Genotyping was performed by PCR amplification of the region of interest. Target sequences, sgRNAs, repair templates, and genotyping primers are listed below:

Myo7a-ΔC and *HA-Myo7a-C* mice:

sgRNA: AAGCATGGTTATTCTGCAGA**AGG**, targeting the second exon of *Myo7a-C* (1st coding exon).

Repair template for *HA-Myo7a-C* mice:

GCCTGGGCTCAGGGCGTGCCATGGTCTCTTCCCACAGAGCTGTGTCTGGTCACTCC
GGCAGGTGTGCTGACGTAGAAGCATGTACCCATACGATGTTCCAGATTACGCTGTTA
TTCTGCAAAAGGTGAGTGCGTCTCCTCTCTCTCAGAGCTGCAGAGGGCCATGCTGG
GTACCTCACATCCCACCCTGCA.

Genotyping primers: GCTCTGGTCACATAGACTGAGCT (forward), and GGGATGAATCATCACTCCTGC (reverse).

Myo7a-ΔN and *HA-Myo7a-N* mice:

sgRNA: AGGGCTTCCGGGGGACTCCA**TGG**. This sgRNA targets the first coding exon of *Myo7a-N* (exon1).

HA-Myo7a-N Repair template:

GTTTAGGGTTCCCAAGCGGGTGGCGTGCGGGATTAGGTGAATTAGGAGCCCGCTTC
GTGTCGTGAGGCCACCAGACCCAGCGCACCATGTACCCATACGATGTTCCAGATTAC
GCTGAGTCCCCCGGAAGCCCTGCTGACCCAGGCGAGGCACCCGCCCCGCCGCCTG
GCAAGTGGGCTCTGGTGCGAAACTTGAACCAA

Genotyping primers: GTGCTCCCTCCCCTACAGTA (forward), CTTTGGTGTGAACTTGGCCG (reverse).

Myo7a-ΔCN mice:

sgRNA: CAAACTCCTGGCCTGACTTC**AGG**, targeting the common exon of *Myo7a-C* (exon 3), *Myo7a-N* (exon 2), and *Myo7a-S* (exon 2).

Repair template for *Myo7a-ΔCN* mice: we deleted one thymine in the reading frame of *Myo7a-C* and *Myo7a-N*. This T deletion is in the untranslated region of *Myo7a-S*.

GGTAGTGGGAGAGAGGGGCTCAACTTCAGGATCTCCTGCCTACAGGGGGACTATGA TGGATGGACCTGAAGTCAGGCCAGGAGTTTGATGTGCCCATCGGGGCCGTGGTGAA GCTCTGCGAC.

Genotyping primers: TTGGTGTGCCTGCCTTAGT (forward), and ACCTGCCATTGTAGCCTTCC (reverse).

Myo7a full KO:

sgRNA: GCCTGATGAAGACGAGGAGGACC. This sgRNA created a 26bp deletion in exon 24

Genotyping primer: CCAGCCTAACGGTTAAGACA (forward), AGCTGGTCACCCTCATCGT (reverse).

Myo7a-ΔS mice:

We designed two sgRNAs that flank the entire first exon of *Myo7a-S*. This method created two DNA double-strand breaks and deleted 275bp, which covers the first exon of *Myo7a-S* (this exon is 107bp).

sgRNAs: CAGCCCTGCCTAAGACAGTG**TGG** (beginning of the exon), GGGGTGTAGTTTGTGGGGTC**AGG** (end of the exon).

Genotyping primers: CAGAGCCTATCTATAGCCTTGTGC (forward), AAGGATGACCTCCCTTCCAT (reverse).

Myo7a-ΔEnhancerA mice:

sgRNAs: ACAACAGCGACTTCCCTGCA**TGG** and GCGAGACTGGCTAGGAACGT**AGG**. Similar strategy with *Myo7a-ΔS* mice, we created an approximately 400bp deletion that covers the entire *EnhancerA*.

Genotyping primers: ACCATGACCCCATAAGGTTC (forward), AGTGTTCTCCCGAGAGCCTTTC (Reverse).

2.3. Immunofluorescence

Inner ear organs were fixed in 3% paraformaldehyde (PFA, Electron Microscopy Sciences, PA) immediately after dissection for 20 min. Samples were washed three times with phosphate-buffered saline (GIBCO® PBS, Thermo Fisher Scientific, Waltham, MA) for 5 min each. After blocking for 2 h with blocking buffer (1% bovine serum albumin, 3% normal donkey serum, and 0.2% saponin in PBS), tissues were incubated in blocking buffer containing primary antibody at 4 °C overnight. The following antibodies were used in this study: rabbit polyclonal Myosin-VIIa antibody (catalog#: 25-6790, Proteus Biosciences Inc, Ramona, CA. 1:100), mouse monoclonal Myosin-VIIa antibody (Developmental Studies Hybridoma Bank, MYO7A 138-1, concentrate, 1:100), mouse monoclonal Myosin-VI antibody (A-9, Santa Cruz, 1:100), rabbit anti-Harmonin antibody (H3, obtained from Ulrich Mueller's lab)[100], rabbit anti-ADGRV1 antibody (obtained from Dominic Cosgrove's lab)[101], rabbit polyclonal Myosin-VIIa antibody used in Fig. 2 (PB206) was custom-generated and affinity purified against the immunizing MYO7A peptide LPGQEGQAPSGFEDLERGR[57], and rabbit anti-HA antibody (C29F4, Cell Signaling Technologies, Danvers, MA). Fluorescence imaging was performed using a Zeiss LSM880 or a Nikon microscope equipped with a 100×, 1.45NA objective and a Yokogawa confocal spinning disk attachment. Images were acquired with an Andor EMCCD camera using Nikon Elements software.

2.4. Hearing tests in mice

ABRs of WT and *Myo7a-ΔC* mice at P17, 4-week, 6-week, and 9-week were determined. Mice were anesthetized with a single intraperitoneal injection of 100 mg/kg ketamine hydrochloride (Fort Dodge Animal Health) and 10 mg/kg xylazine hydrochloride (Lloyd Laboratories). ABR and DPOAE were performed in a sound-attenuating cubicle (Med-Associates, product number: ENV-022MD-WF), and mice were kept on a Deltaphase isothermal heating pad (Braintree Scientific) to maintain body temperature. ABR recording equipment was purchased from Intelligent Hearing Systems (Miami, Fl). Recordings were captured by subdermal needle electrodes (FE-7; Grass Technologies). The non-inverting electrode was placed at the vertex of the midline, the inverting electrode over the mastoid of the right ear, and the ground electrode on the upper thigh. Stimulus tones (pure tones) were presented at a rate of 21.1/s through a high-frequency transducer (Intelligent Hearing Systems). Responses were filtered at 300–3000 Hz, and threshold levels were determined from 1024 stimulus presentations at 8, 11.3, 16, 22.4, and 32 kHz. Stimulus intensity was decreased in 5–10 dB steps until a response waveform could no longer be identified. Stimulus intensity was then increased in 5 dB steps until a waveform could again be identified. If a waveform could not be identified at the maximum output of the transducer, a value of 5 dB was added to the maximum output as the threshold.

DPOAEs of the same group of WT and *Myo7a-ΔC* mice were recorded. While under anesthesia for ABR testing, DPOAE was recorded using SmartOAE ver. 5.20 (Intelligent Hearing Systems). A range of pure tones from 8 to 32 kHz (16 sweeps) was used to obtain the DPOAE for the right ear. DPOAE recordings were made for $f2$ frequencies from 8.8 to 35.3 kHz using a paradigm set as follows: $L1 = 65$ dB, $L2 = 55$ dB SPL, and $f_2/f_1 = 1.22$.

2.5. Whole-cell voltage-clamp electrophysiology recordings

2.5.1. Animals:

For electrophysiology and hair bundle motion recordings, C57BL/6J wild type and *Myo7a-ΔC* mutant mice of both sexes were used for experiments. All experiments were performed on mice aged postnatal day (P) 7–8. *Myo7a-ΔC* animals were bred in-house at 12/12 h light/dark cycle and had access to food and water ad libitum. *Preparation and recordings*: Animals were euthanized by decapitation using methods approved by the University of Colorado IACUC. Organs of Corti were acutely dissected from P7–8 mice and placed in recording chambers as previously described[31]. Tissue was viewed using a 100× (1.0 NA, Olympus or 1.1 NA, Nikon) water-immersion objective with a Phantom Miro 320s or Veo 410L (Vision Research) camera on a Slicescope (Scientifica) or FN1 (Nikon) illuminated with a TLED+ 525 nm LED (Sutter Instruments). Tissue was dissected and perfused with extracellular solution containing (in mM): 140 NaCl, 2 KCl, 2 $CaCl_2$, 2 $MgCl_2$, 10 HEPES, 2 creatine monohydrate, 2 Na-pyruvate, 2 ascorbic acid, 6 dextrose, pH = 7.4, 300–310 mOsm. In addition, apical perfusion, with pipette tip sizes of 150–300 µm, provided local perfusion to the hair bundles.

2.5.2. Electrophysiological recordings:

Whole-cell patch-clamp was achieved on IHCs from middle to apical cochlear turns or basal OHCs using an Axon 200B or Multiclamp 700B amplifier (Molecular Devices) with thick-walled borosilicate patch pipettes (2–6 MΩ) filled with an intracellular solution containing (in mM): 92 CsCl, 3.5 $MgCl_2$, 5 ATP, 5 creatine phosphate, 10 HEPES, 10 cesium BAPTA, 3 ascorbic acid, pH = 7.2, 280–290 mOsm. Experiments were performed at 18–22 °C. Whole-cell currents were filtered at 10 kHz and sampled at 100 kHz using a USB-6356 or USB-6366 (National Instruments) controlled by jClamp (SciSoft Company).

All experiments used −80 mV holding potential, uncorrected for liquid junction potential. Only cells with initially <200 A of leak current were kept for data analysis.

2.5.3. Hair bundle stimulation and motion recording:

Hair bundles are stimulated with a custom 3D printed fluid jet driven by a piezoelectric disc bender (27 mm 4.6 kHz; Murata Electronics 7BB-27-4L0). Thin-wall borosilicate pipettes were pulled to tip diameters of 5–20 µm, filled with extracellular solution, and mounted in the fluid-jet stimulator. The piezo disc bender was driven by waveforms generated using jClamp and the signals were filtered with an eight-pole Bessel filter at 1 kHz (L8L 90PF, Frequency Devices Inc.) or 2 kHz (3382, Krohn-Hite Corporation) and variably attenuated (PA5, Tucker Davis) before being sent to a high voltage/high current amplifier (Crawford Amplifier) to drive the piezoelectric disc. During stimulations, videos were taken of the hair bundle motion with high-speed imaging at 10,000 frames per second using the Phantom Miro 320s or Veo 410L. Videos were saved for each stimulation and analyzed offline.

2.5.4. Analysis:

All data were analyzed offline using jClamp (SciSoft), Matlab (MathWorks), Excel (Microsoft), and Prism 7 (GraphPad). Figures were generated using Matlab, Prism 7, and Adobe Illustrator.

2.5.5. Hair bundle motion analysis:

Custom Matlab (Mathworks) scripts were used for analysis of the hair bundle motion. Video frames were imported into Matlab and the position of the hair bundle was extracted using a Gaussian fit to a band-pass filtered hair bundle image[102] for a given vertical row of pixels in the image to yield subpixel resolution. For 50 ms fluid-jet stimulus steps, the motion of the hair bundle was fit with a double exponential, with the onset of the fit occurring after the force of the fluid-jet stimulus plateaus:

$$y = y_0 + A_1 e^{-\frac{x-x_0}{\tau_1}} + A_2 e^{-\frac{x-x_0}{\tau_2}}, \quad (1)$$

where τ_1 and τ_2 are the decay constants and A_1 and A_2 are the respective amplitudes. For a majority of cells, the center of the hair bundle was used to analyze motion.

2.5.6. Electrophysiological data analysis:

The resting open probability of MET channels (defined as P_{open}, or P_o) was determined from sine wave stimulation of the hair bundle and calculated using Eq. (2), where I_{max} is the current elicited during maximum positive stimulation, I_{leak} is the current remaining during maximum negative stimulation, and $I_{resting}$ is the resting mechanosensitive current (defined as the current in the absence of stimulation, subtracted by I_{leak}). We assumed we could observe a P_o of 0% and 100% during the maximum negative and positive stimulations, respectively,

$$P_0 = \frac{\mathrm{I_{resting}}}{\mathrm{I_{max}} - \mathrm{I}_{leak}}, \quad (2)$$

Current–displacement (IX) plots used the displacement data from the high-speed imaging analysis. To generate the IX plot, displacement values were taken when the maximum current occurred for each 50 ms step in a 13-step family of stimulations. Normalized currents (I/I_{max}) were generated by subtracting I_{leak} and normalizing to the maximum current recorded for the entire stimulus family, which typically occurred on the 12th or 13th stimulus. IX plots were fit with a double Boltzmann equation

$$y = \frac{\mathrm{I_{max}}}{1 + e^{Z_2(x_0 - x)}\left(1 + e^{Z_1(x_0 - x)}\right)}, \quad (3)$$

where Z_1 and Z_2 are the slope factors and x_o is the set point.

2.5.7. Analysis of MET current and hair bundle rise kinetics:

For analysis of the MET current and hair bundle displacement rise kinetics, the time for 10 and 90% of the maximum motion or current to rise for each 50 ms stimulus step was determined from the raw displacement data obtained from the high-speed imaging, or

the raw MET current data. In the text and figures, $t_{10\%}$ and $t_{90\%}$ refer to the time (in milliseconds) for 10% and 90% of the motion or current to rise, respectively. The $t_{10-90\%}$ is defined as the time for between 10 and 90% of the motion or current to rise, and is calculated by subtracting $t_{10\%}$ from $t_{90\%}$.

2.6. Scanning electron microscopy

Adult mice were euthanized by CO_2 asphyxiation before intracardiac perfusion with 2.5% glutaraldehyde (Electron Microscopy Sciences, Hatfield, PA) and 2% PFA. The otic capsule was dissected and incubated in postfixation buffer at 4 °C overnight (2.5% glutaraldehyde, in 0.1 M cacodylate buffer, with 3 mM $CaCl_2$). For neonatal mouse pups, the samples were dissected and treated with postfixation buffer immediately. The otic capsules from adult mice were incubated for two weeks in 4.13% EDTA for decalcification and then further dissected to expose the organ of Corti. Samples underwent the OTOTO procedure and were dehydrated using gradient ethanol and critical point drying. After sputter coating with platinum, the samples were imaged on Zeiss Sigma VP HD field emission SEM using the in-lens secondary electron detector.

2.7. Stereocilia Length Quantification:

Previous studies have reported methods to calculate stereocilia length from SEM stereo images[103,104]. Building on those existing methods, we developed a mathematical model that allows us to determine the lengths of stereocilia tilted in any direction and determine the lengths of stereocilia in which their stereocilia bases (insertion point into the cuticular plate) is obstructed by front row stereocilia.

SEM stereo-images provide two different imaging planes with a known angle between them. This allows the reconstruction of the three-dimensional coordinates of all visible points (stereocilia tips and insertion points) using basic linear algebra. This in turn is used to calculate the actual lengths of the stereocilia employing Euclidean metric in three

dimensions. For calculating the lengths of stereocilia with obstructed stereocilia bases, we use one image and the angle between the oxy plane and the cell surface (assuming that locally it is close to a plane). We continue the vector between two visible points of the stereocilia and find its intersection with the cell surface using basic linear algebra. Using this calculated invisible point, we find the length using the Euclidean metric in three dimensions.

2.7.1. Details of the calculation of the length of fully visible stereocilia, tilted in any direction (Illustrated in a and b):

A stereo-pair of SEM images was taken with a tilt of α degrees (5 degree in the image pair). For the optimal application of this method, eucentric stereo-pairs of hair cells should be taken (hair bundle base lies parallel to the rotation axis of the SEM stage). With this assumption in place, we can measure each stereocilium as a vector. In the model described in Fig2-1B, vector OA represents a stereocilium, and vector OB the same stereocilium tilted at an angle α. Their corresponding projections onto the image plane are OA' and OB' (the side edge of the SEM image corresponds to the y-axis), respectively. The lengths of these projections P_a and P_b (length of the stereocilia as they project onto the image plane), and the angles θ_a and θ_b (angles between vectors A' and B' and the x-axis) were measured in ImageJ. The coordinates of vector A' and B' were then calculated using the equations below:

$$\begin{cases} x_a = P_a \cdot \cos\theta_a \\ y_a = P_a \cdot \sin\theta_a \end{cases}$$

$$\begin{cases} x_b = P_b \cdot \cos\theta_b \\ y_b = P_b \cdot \sin\theta_b \end{cases}$$

By using the coordinates of A' and B', the length of the stereocilia can be calculated using the formula below:

$$\delta = \cos\alpha$$

$$Stereocilia\ Length =$$

$$\sqrt{\frac{x_a^2 + x_b^2 + y_a^2 + y_b^2 - 2\delta x_a x_b - 2\delta y_a y_b + \sqrt{-4(-1+\delta^2)(x_a x_b - \delta(x_a^2 + y_a^2) + y_a y_b + ((-1+2\delta^2)x_a^2 + x_b^2 - y_a^2 + y_b^2 + 2\delta^2 y_a^2 - 2\delta x_a x_b - 2\delta y_a y_b)^2}}{2(-1+\delta^2)}}$$

2.7.2. Calculation of the length of stereocilia with obstructed bases:

Five parameters are needed: (1) the angle of the shorter row stereocilium (θ_a) to the x-axis, (2) the length of the projection of the shorter row stereocilium (P_a), (3) the angle of the longer row stereocilium (θ_c) to the x-axis, and (4) the length of the projection of the step of the longer row stereocilium (P_c), defined as the distance between the tip of the longer row stereocilium and the tip of the shorter row stereocilium in front of it (segment AC and A'C')), (5) the angle between cell surface and image plane. Using the method shown above, the length of the stereocilium and the step can be also calculated (L_a, L_c). The coordinates of the tips of the shorter and longer row stereocilia (Point A and Point C in the figure D) can then be calculated using the formulae below:

$$\begin{cases} x_a = P_a \cdot \cos\theta_a \\ y_a = P_a \cdot \sin\theta_a \\ z_a = \sqrt{L_a^2 - P_a^2} \end{cases}$$

$$\begin{cases} x_c = P_c \cdot \cos\theta_c + x_a \\ y_c = P_c \cdot \sin\theta_c + y_a \\ z_c = \sqrt{L_c^2 - P_c^2} + z_a \end{cases}$$

To calculate the angle between the cell surface and the image plane (angle φ), two landmarks on the cell surface are selected (point M and point N). The vector MN should be perpendicular to the x-axis. The length of the projection of MN can be measured using ImageJ. Then, the same points are selected on the stereo-pair of the SEM. Using the same method as used to determine the length of the shorter row stereocilia, the length of the vector MN can be calculated. And the angle φ can be calculated by using the equation below:

$$\varphi = \arccos\left(\frac{Projection_{MN}}{Length_{MN}}\right)$$

With angle φ known, the coordinate of the point Q, which represents the (invisible) root of the longer row stereocilium, will be calculated as the intersection between vector AC and the cell surface.

$$\begin{cases} x_q = \dfrac{x_a y_c \tan\varphi - x_c y_a \tan\varphi - x_c z_a + x_a z_c}{y_c \tan\varphi - y_a \tan\varphi - z_a + z_c} \\ y_q = \dfrac{-y_c z_a + y_c z_a}{(y_c - y_a)\tan\varphi - z_a + z_c} \\ z_q = y_q \tan\varphi \end{cases}$$

After calculating the coordinates of Q, the length of vector CQ, representing the length of the longer row stereocilium, can be calculated using the equation below:

$$Stereocilia\ length = \sqrt{(x_q - x_c)^2 + (y_q - y_c)^2 + (z_q - z_c)^2}$$

The calculations were performed in R.

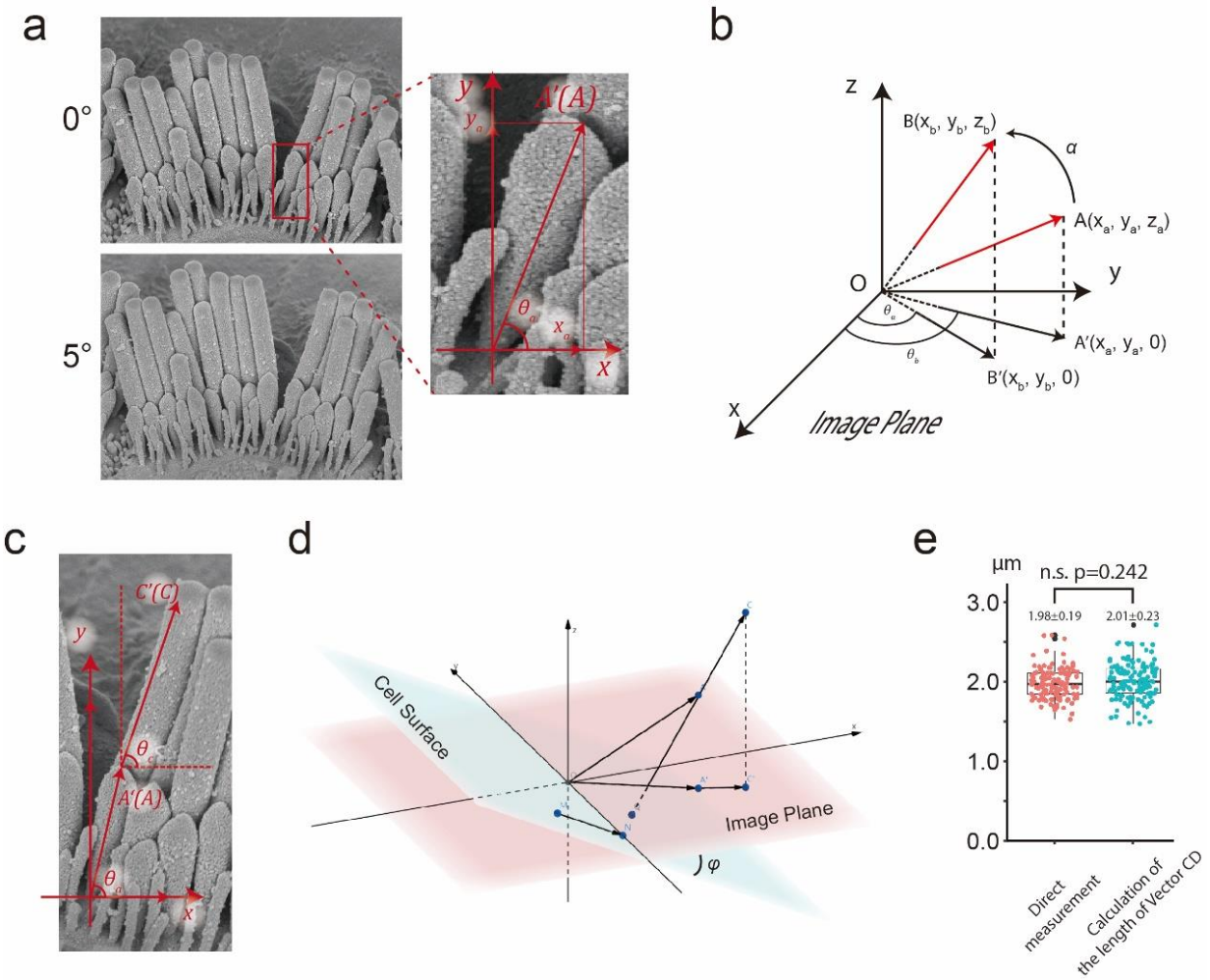

Figure 2-1: Quantification of stereocilia length using a pair of stereo images from SEM.

A. A representative pair of stereo images of hair bundle. The angle differences between these two images is 5º. The right panel shows the stereocilia, which is represented as vector OA(x_a, y_a). The angle between OA and x-axis is angle θ_a. Correspondingly, in the images that is rotated 5º, the new vector of the same stereocilia is OB(x_b, y_b). The angle between OB and x-axis is θ_b. **B**. A simplified model of stereocilia OA and OB in a three dimension coordinate system. The projection of vector OA(x_a, y_a, z_a) and OB(x_b, y_b, z_b) on the plane of *xoy* is represented as OA'(x_a, y_a, 0) and OB'(x_b, y_b, 0). Angle α is the angle of two stereo images (5º in this example). The z_a of vector OA can be calculated by applying the formula provided above. Then, the length of the stereocilia can be calculated as the length of vector OA. **C**. After vector OA is calculated, the

similar method can be applied to calculate the length of the third row of the stereocilium, of which the root of the stereocilia is hidden in the image. **D**. A simplified three-dimension coordinate system of the relationship between cell surface and image plane of scanning electron microscope. Point N represents the root of third row stereocilia on the cell surface. **E**. To validate the method described in C and D, we compared the lengths of the longest row of stereocilia in 6-week old apical OHC stereocilia as determined by two different methods: For stereocilia with visible stereocilia bases, we directly calculated their length by using the method described in panel a and b. For the stereocilia with invisible bases, we used the method described in panel c and d. T-test indicated no significant difference between these two methods (# of stereocilia: directly measurement=129, vector length calculation=139).

3. Chapter 3: Myosin-VIIa is expressed in multiple isoforms and essential for tensioning the hair cell mechanotransduction complex

3.1. Multiple isoforms of MYO7A are expressed in the organ of Corti

Analysis of genomic sequence databases revealed the existence of multiple MYO7A isoforms. Two such isoforms are generated by alternative transcription and translation start sites (Fig. 3-1B, C). The translation start site (ATG) of the canonical isoform (MYO7A-C) is in exon 2, while the start site of a shorter isoform (*MYO7A-S*), as predicted in the database, is located two exons downstream. Despite the 10 kb-long intervening genomic sequence between the two start sites, MYO7A-C is distinguished from *MYO7A-S* only by an eleven amino acid (aa) N-terminal extension to the myosin head domain (Fig. 3-1B).

To investigate the expression and functional relevance of these two MYO7A isoforms in hair cells, we generated a mouse line in which the canonical isoform was specifically deleted (*Myo7a-ΔC* mouse). Using CRISPR/Cas9 genome editing, a truncating frameshift mutation (1 bp insertion) in exon 2 (ten bases downstream of the start codon) of the mouse *Myo7a* gene was introduced (Fig. 3-1B-D). *Myo7a-ΔC* mice had no overt behavioral phenotype, and all parts of the inner ear developed normally.

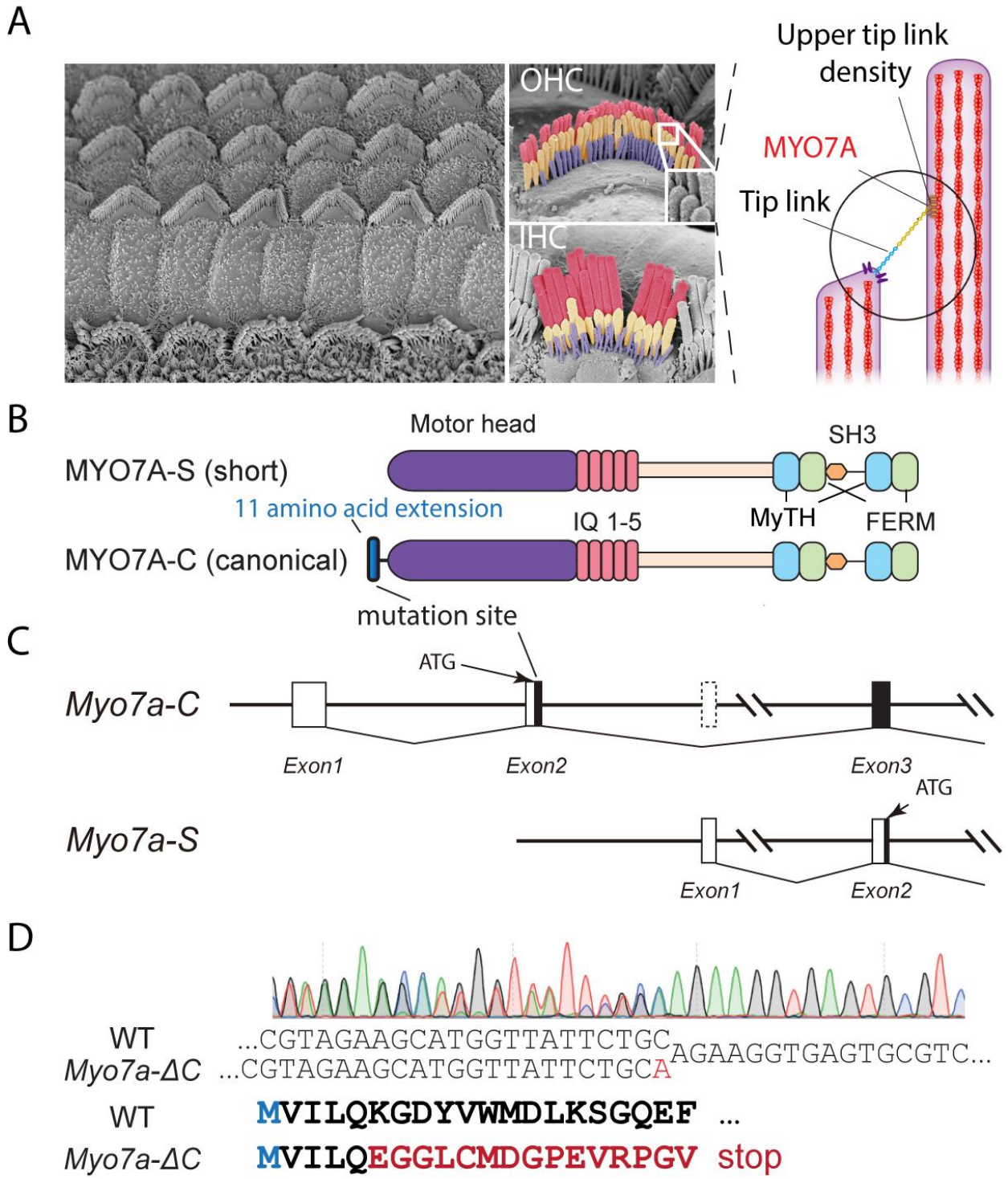

Figure 3-1. Specific deletion of the canonical MYO7A-C isoform

A. Scanning electron micrographs depicting IHCs and OHCs in the mouse organ of Corti and a schematic illustration of the proposed function of MYO7A at the upper tip-link density of the mechanotransduction complex. **B-C**. Graphical illustration of the canonical and the presumed

short MYO7A protein isoforms (MYO7A-C and MYO7A-S, respectively) and corresponding genomic structures. The site of the deleterious mutation in the *Myo7a-ΔC* mouse is indicated. **D**. Sanger sequencing result of the heterozygous *Myo7a-ΔC* founder mouse. An adenine insertion (shown in red) introduces a deleterious mutation in the reading frame of *Myo7a-C*. Sequencing was performed from the reverse direction.

3.2. Deletion of MYO7A-C primarily affects MYO7A in cochlear IHCs

We examined the spatiotemporal expression of MYO7A in *Myo7a-ΔC* mice. Strikingly, MYO7A immunoreactivity was strongly diminished in IHCs, while expression in OHCs was not overtly affected (Fig. 3-2A, C). Despite the significant reduction in MYO7A levels, IHCs in the *Myo7a-ΔC* mice had WT-like bundle morphology at postnatal day 5 (P5). These observations were in significant contrast to the severe morphological defects present in the hair bundles of *Myo7a* full KO mice (Fig. 3-2C), which we generated independently by introducing a deleterious mutation in exon 24. Hair bundle morphology was analyzed in more detail in P7 hair cells: the lengths of the longest and second row IHC stereocilia were measured in volume-rendered phalloidin fluorescence confocal images. No significant differences between *Myo7a-ΔC* and WT counterparts were observed ($p=0.706$ and $p=0.936$ for the first and second row, respectively) (Fig. 3-2E). Additional analyses of stereocilia morphologies using stereo-pairs of scanning electron micrographs (SEMs) using a modified version of previously described methods[103,105] also revealed no significant differences between *Myo7a-ΔC* and WT IHCs ($p=0.563$ and $p=0.364$ for first and second row, respectively) and OHCs ($p=0.248$, $p=0.755$, $p=0.64$ for first, second and third row, respectively) (Fig. 3-2F, G). We suggest that the seemingly normal hair bundle development in cochlear IHCs is due to the residual and redundant expression of unaffected MYO7A isoforms, presumably *MYO7A-S*, in the *Myo7a-ΔC* mice. Additionally, in the vestibular utricle of *Myo7a-ΔC* mice, MYO7A expression in all hair cells, as determined by relative immunofluorescence to MYO6, was reduced by 63% (1.35 ± 0.19 in WT; n=9 utricles compared to 0.52 ± 0.11 in *Myo7a-ΔC*; n=9 utricles; $p < 1e\text{-}4$), without cell-type specific distinction (Fig. 3-2B).

A more detailed analysis of the remaining cellular expression pattern of MYO7A in the *Myo7a-ΔC* mice uncovered tonotopic differences in OHCs: MYO7A levels in OHCs of

Myo7a-ΔC mice were similar to WT levels in basal regions of the cochlea but decreased in the middle and apical turns by ~30% and 52% ($p<1e-3$ and $<1e-4$), respectively (Fig. 3-3A, B). The quantification was conducted by normalizing the MYO7A immunoreactivity to MYO6 immunoreactivity, which was invariable between *Myo7a-ΔC* and WT mice and along the tonotopic axis. We therefore inferred that MYO7A-C is predominantly expressed in all IHCs and in a tonotopic gradient in OHCs, decreasing from the apex towards the base of the cochlea. The presumed alternative isoform *MYO7A-S*, which cannot be specifically detected due to sequence overlap with MYO7A-C (Fig 3-1B, C), is hypothesized to be expressed weakly in IHCs (constituting ~15% of overall MYO7A expression level) and in OHCs in a tonotopic gradient that runs counter to that of MYO7A-C.

Attempts to generate an MYO7A-C-specific antibody failed due to the low antigenicity of the 11-aa N-terminal peptide. To obtain direct evidence for the cellular expression of MYO7A-C, we generated the *HA-Myo7a-C* KI mouse line, by knocking in an HA-tag immediately after the MYO7A-C start codon (Fig. 3-3C). Consistent with the phenotype of the *Myo7a-ΔC* mouse, HA-MYO7A-C immunoreactivity was strong in all IHCs, and in OHCs, decreased towards the base of the cochlea (Fig. 3-3D). The same expression pattern was observed in mature (P30) *HA-Myo7a-C* KI mice, demonstrating that this expression is not a transient phenomenon during development.

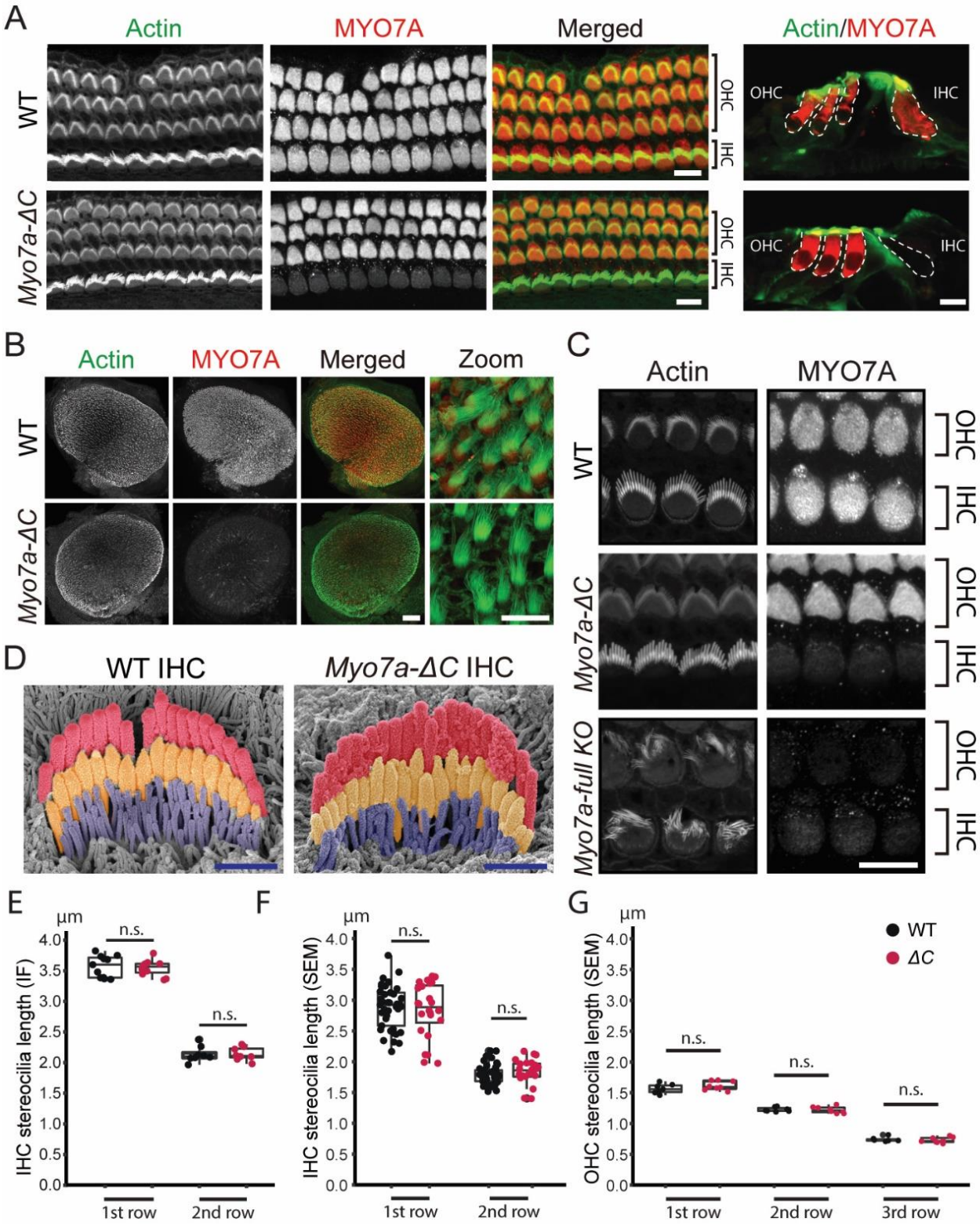
A
Actin
MYO7A
Merged
Actin/MYO7A
WT
Myo7a-ΔC
OHC
IHC
B
Zoom
C
Myo7a-full KO
D
WT IHC
Myo7a-ΔC IHC
E
F
G
µm
IHC stereocilia length (IF)
IHC stereocilia length (SEM)
OHC stereocilia length (SEM)
n.s.
1st row
2nd row
3rd row
WT
ΔC

Figure 3-2. Deletion of MYO7A-C primarily affects MYO7A expression in IHCs and utricle hair cells

A. MYO7A immunoreactivity in WT and *Myo7a-ΔC* organ of Corti (P5), counterstained with phalloidin (F-actin). MYO7A immunoreactivity is predominantly decreased in the IHCs of *Myo7a-ΔC* cochleae (scale bars 10 μm). The reduction of MYO7A immunoreactivity in IHCs have been observed in more than 15 individual experiments and the quantification is shown in figure 3B. **B**. Utricles (P5) were stained for MYO7A and phalloidin. MYO7A immunoreactivity is significantly reduced in all utricle hair cells (by 63%, P-value < 1e-4) (scale bars: 100 μm left, 10 μm right). **C**. MYO7A immuno- and phalloidin-reactivity in IHCs and OHCs in WT, *Myo7a-ΔC* and *Myo7a full KO* mice (scale bar 10 μm). Although MYO7A levels are significantly depleted in *Myo7a-ΔC* IHCs, hair bundle morphology is not affected. **D**. Representative SEMs of IHCs of P7 WT and *Myo7a-ΔC* (scale bar 1 μm). **E**. Quantification of stereocilia length in P7 IHCs by immunofluorescence (using Imaris 3D module) found no significant differences between WT and *Myo7a-ΔC* mice (Length of the first row: WT =3.57±0.18; *Myo7a-ΔC* =3.54±0.13, p = 0.706. The number of cells: WT=11, *Myo7a-ΔC* =11; the number of animals: WT=6, *Myo7a-ΔC*=4. Length of second row: WT =2.13±0.13, *Myo7a-ΔC* =2.14±0.11, p = 0.936. The number of cells: WT=8, *Myo7a-ΔC* =8; the number of animals: WT=4, *Myo7a-ΔC*=3. **F**. Quantification of stereocilia length in P7 IHCs by SEM found no significant differences between WT and *Myo7a-ΔC* mice (Length of the first row: WT =2.88±0.35, *Myo7a-ΔC* =2.83±0.45, p = 0.664. Length of second row: WT =1.80±0.16, *Myo7a-ΔC* =1.84±0.19, p = 0.363. Number of stereocilia: WT=141, *Myo7a-ΔC* =123, Number of cells: WT=41, *Myo7a-ΔC* =24; number of animals: WT=10, *Myo7a-ΔC*=7). **G**. Quantification of stereocilia length in P7 OHCs by SEM found no significant differences between WT and *Myo7a-ΔC* mice (Length of the first row: WT =1.57±0.077, *Myo7a-ΔC* =1.61±0.074, p = 0.23. Length of second row: WT =1.23±0.036, *Myo7a-ΔC* =1.22±0.052, p = 0.80. Length of third row: WT =0.74±0.036, *Myo7a-ΔC* =0.73±0.045, p = 0.64. Number of stereocilia: WT=73, *Myo7a-ΔC* =70, number of cells: WT=7, *Myo7a-ΔC* =8; the number of animals: WT=3, *Myo7a-ΔC*=3). P-values of

E-G were derived from two-tailed, unpaired t-tests. Boxplots show medians, 25th, and 75th percentiles as box limits, and minima and maxima as whiskers.

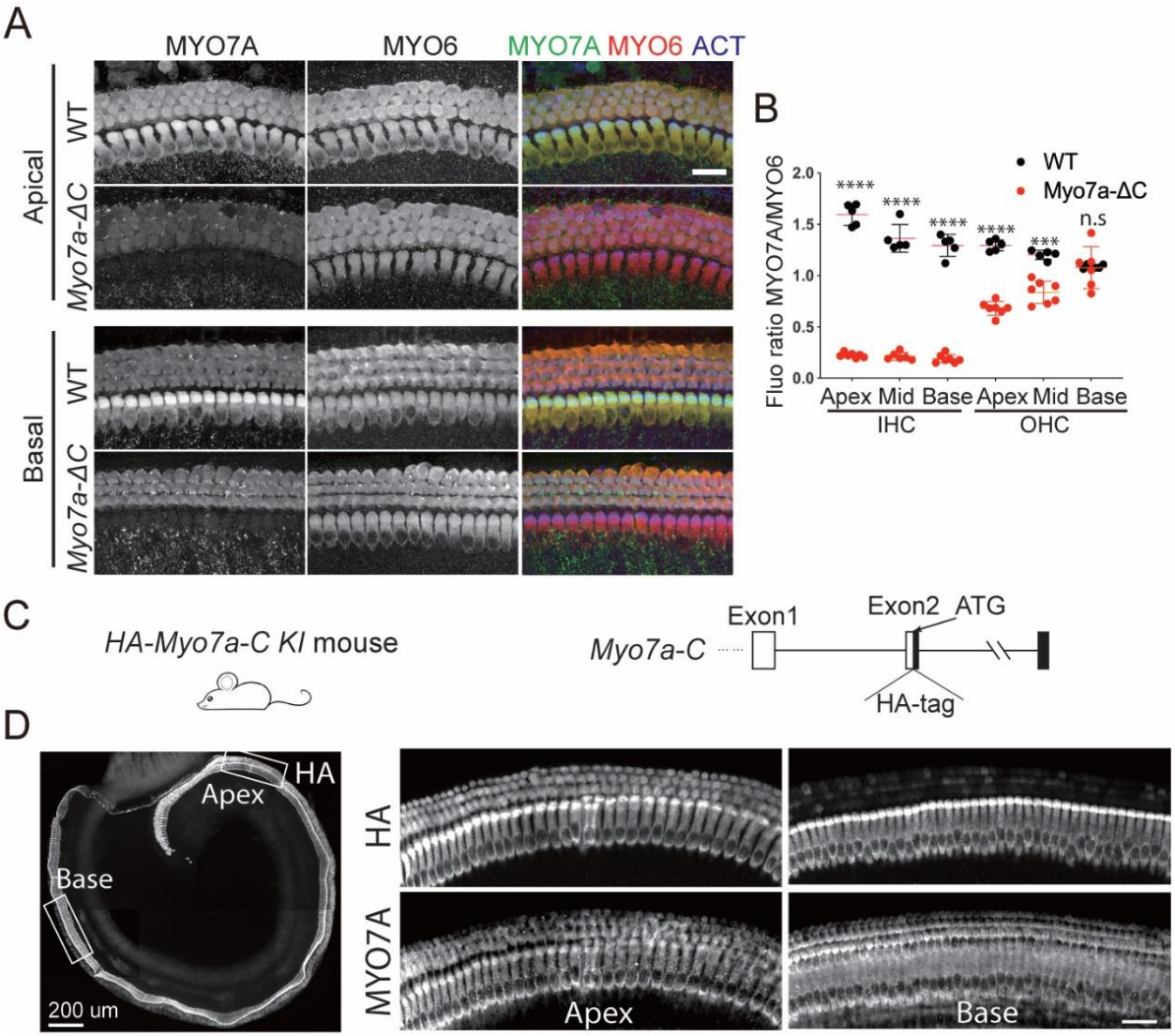

Figure 3-3. MYO7A-C is expressed primarily in IHCs and in a tonotopic gradient in OHCs, with decreasing expression towards the cochlear base.

A. MYO7A and MYO6 immunoreactivity in apical and basal turns of organ of Corti of P5 *Myo7a-ΔC* and WT mice (scale bar: 10 μm). **B**. MYO7A immunoreactivity was quantified in apical, middle, and basal turns by normalizing to MYO6 immunoreactivity. Compared to WT, MYO7A levels in *Myo7a-ΔC* mice were reduced by ~85% (p <1e-4) in all IHCs, and by ~30% and 52% (p <1e-3 and <1e-4) in middle and apical-turn OHCs. Each data point in b corresponds to a mean MYO7A/MYO6 immunofluorescence ratio (mean of ~12 IHCs and ~36 OHCs per organ and position). n (animals) = 5 in WT and 7 in *Myo7a-ΔC*. The plot was shown as mean±SD. **C**.

Design of the *HA-Myo7a-C* KI mouse. An HA-tag was knocked-in after the ATG of *Myo7a-C* by CRISPR-mediated gene editing. **D**. Organ of Corti of an *HA-Myo7a-C* mouse, stained with an HA-specific antibody. The white boxes indicate the approximate positions of the apical and basal cochlear regions shown on the right. HA immunoreactivity, representing the expression of MYO7A-C, is strong in all IHCs. In OHCs, HA immunoreactivity is readily detected at the cochlear apex but decreases towards the base (scale bar: 20 μm).

3.3. Reduced MYO7A levels at the UTLD and stereocilia base of *Myo7a-ΔC* IHCs

MYO7A was reported to localize to several sites within the hair cell in addition to the diffuse staining throughout the cytosol, including the stereocilia base and the UTLD. The localization at the UTLD is believed to be essential for MYO7A's proposed function as the tip-link motor[57], while at the stereocilia base, MYO7A is involved in establishing the ankle link complex[106–110]. Using a previously characterized antibody[57], we examined the localization of MYO7A at the UTLD and the stereocilia base. At the UTLD of *Myo7a-ΔC* IHCs, MYO7A immunoreactivity was detected but reduced by 68% at P7 ($p<1e-3$) and 58% at P16 ($p<1e-3$) compared to WT. At the stereocilia base, the MYO7A signal was reduced by 81% at P7 ($p<1e-3$) and 69% at P16 ($p<1e-3$) (Fig. 3-4A-D). Compared to the 85% ($p<1e-4$) reduction of cytosolic MYO7A (Fig. 3B, for middle region IHCs), the degree of MYO7A reduction was therefore comparable at the stereocilia base but less pronounced at the UTLD, suggestive of MYO7A sequestration through high-affinity binding sites at the UTLD.

In our hands, the localization of MYO7A at the UTLD could only be visualized with the antibody developed by Grati et al.[57], while commercially available MYO7A antibodies failed to reproduce this staining. The *HA-Myo7a-C* KI mouse model represented an opportunity to independently validate MYO7A's localization at the UTLD, which is of high significance for its proposed role as the tip-link motor. Immunofluorescence imaging using a commercially available HA antibody resolved the membrane-adjacent localization of HA-MYO7A-C, as well as MYO7A enrichment at the predicted site of the UTLD and the stereocilia base. In a subset of stereocilia, MYO7A signal was also observed at the stereocilia tips (Fig. 3-4E). The significance of the tip localization is unknown and remains to be investigated in future studies.

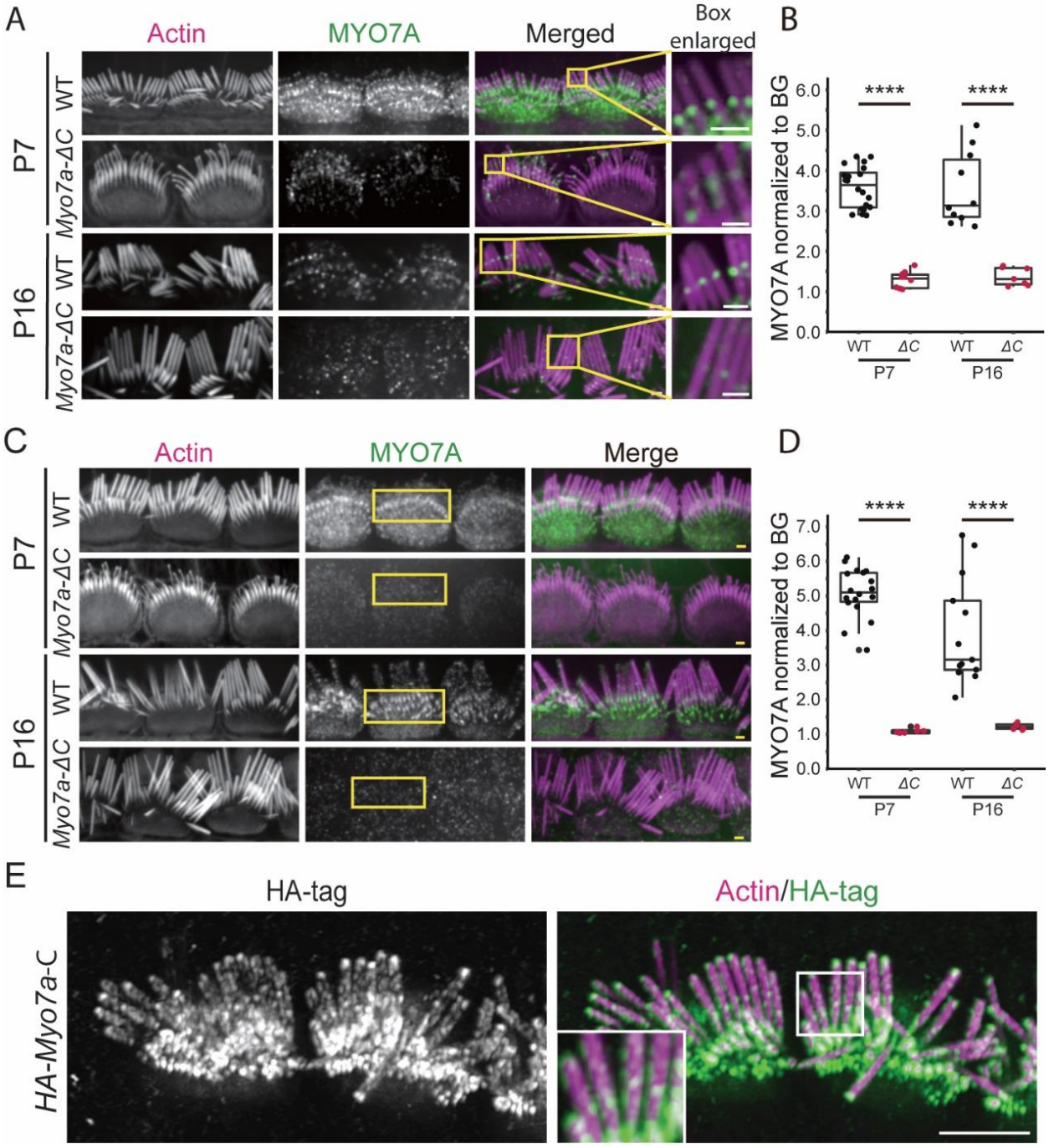

Figure 3-4: Reduced, but detectable levels of MYO7A at the UTLD and stereocilia base of *Myo7a-ΔC* mice

A. MYO7A immunoreactivity at the UTLD in WT and *Myo7a-ΔC* mice at P7 and P16. MYO7A immunoreactivity is detected in the UTLD of *Myo7a-ΔC* IHCs, but the intensity is reduced compared to WT counterparts. Scale bar=1μm. **B**. MYO7A immunoreactivity in the UTLD of

Myo7a-ΔC mice decreased by 68% at P7 (p<1e-3) and 58% at P16 (p<1e-3) compared to WT. The fluorescence intensity of MYO7A puncta was normalized against a dark background near the UTLD staining in the same image and z-section. Mean normalized intensities of MYO7A at UTLD: P7: WT=3.58, *Myo7a-ΔC*=1.28±0.51, p = 2.73e-16±0.21; P16: WT=3.59±1.00, *Myo7a-ΔC*=1.37±0.23, p = 4.30e-05. Number of analyzed UTLD (# of cells; animals): WT: P7=157 (20; 4), P16=73 (10; 4); *Myo7a-ΔC*: P7=62 (10; 4), P16= 35 (7; 4). For statistical analysis, each data point represents the mean normalized UTLD immunofluorescence per cell. P-values were derived from two-tailed, unpaired t-tests. Boxplots show medians, 25th, and 75th percentiles as box limits, and minima and maxima as whiskers. **C**. MYO7A immunoreactivity at the stereocilia base of IHCs of WT and *Myo7a-ΔC* at P7 and P16. Scale bar 1 μm. **D**. Quantification of MYO7A fluorescence intensity at the stereocilia base. The fluorescence intensity of MYO7A puncta was normalized against a dark background in the image. P7: WT=5.09±0.71, *Myo7a-ΔC*=1.093±0.068, p = 6.98e-15; P16: WT=3.96±1.54, *Myo7a-ΔC*=1.23±0.089, p = 3.35e-05. Number of analyzed stereocilia base (# of cells; animals): WT: P7=406 (18; 4), P16=187 (13; 4); *Myo7a-ΔC*: P7=64 (6; 4), P16=79 (6; 4). For statistical analysis, each data point represents the mean normalized immunofluorescence per cell. P-values were derived from two-tailed, unpaired t-tests. Boxplots show medians, 25th, and 75th percentiles as box limits and minima and maxima as whiskers. **E**. Immunofluorescence imaging with an HA-specific antibody resolved the membrane-adjacent localization of HA-MYO7A-C in the HA-MYO7A-C KI mice, as well as MYO7A enrichment at the predicted site of the UTLD and the stereocilia base. In some stereocilia, the MYO7A signal was also observed at the stereocilia tips. The inset shows the HA-tag signal at the UTLD at higher magnification. Scale bar 5 μm.

3.4. Harmonin and ADGRV1 localization is not decreased in *Myo7a-ΔC* IHCs

A tripartite complex consisting of MYO7A, sans and harmonin was shown to constitute the major protein components of the UTLD. Harmonin, the most abundant protein of the UTLD[57], is required for UTLD formation and its hypofunction affects tip-link tension[100,111]. Furthermore, a previous study showed that its localization to the UTLD depends on MYO7A[55]. We therefore investigated whether the reduced levels of MYO7A in *Myo7a-ΔC* IHCs affect the localization of harmonin. Consistent with previous studies[57], harmonin localization in WT IHC and OHC stereocilia was readily detected at the presumed position of the UTLD (Fig. 5A, B). Interestingly, despite a 68% reduction of MYO7A levels at the UTLD, harmonin immunoreactivity was not reduced, but rather slightly elevated in *Myo7a-ΔC* IHCs (Fig. 5A-C). Furthermore, the average number of harmonin puncta per cell was not significantly different between *Myo7a-ΔC* IHCs and WT counterparts (11.1 +/- 3.16 in WT and 12.3 +/- 2.62 in *Myo7a-ΔC*, t-test p=0.271). This contrasts with the severe mislocalization of harmonin (formation of aggregates in the cuticular plate) that was observed in *Myo7a full KO* hair cells (Fig. 5A), consistent with a previous study[55]. A previous study also demonstrated that the localization of the ankle-link component ADGRV1 (also known as VLGR1, GPR98, MASS1) was disturbed in *Myo7a* null Shaker-1 mice[106]. Immunolocalization of ADGRV1 using a previously described antibody[101] demonstrated that ADGRV1 at the stereocilia base was not significantly altered in *Myo7a-ΔC* IHCs (Fig. 5D, E). We conclude that the residual level of MYO7A in *Myo7a-ΔC* IHCs is sufficient to mediate the targeting of harmonin and ADGRV1 to the UTLD and the ankle-link complex, respectively.

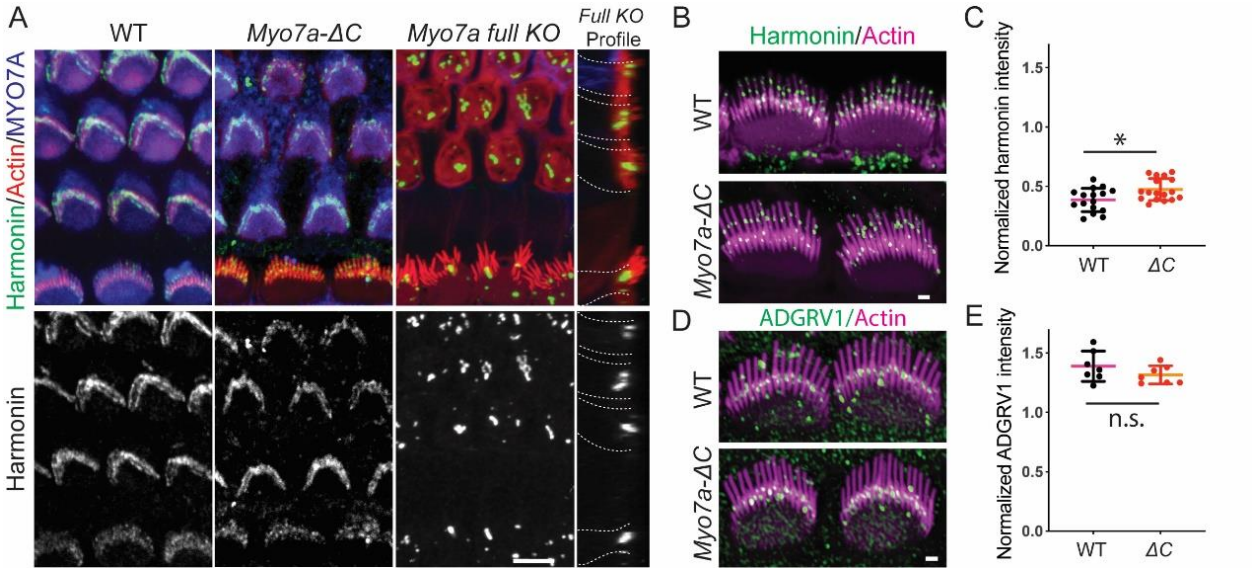

Figure 3-5: Harmonin and ADGRV1 localization at the UTLD and the stereocilia base are not decreased in *Myo7a-ΔC* mice

A. WT and *Myo7a-ΔC* organ of Corti immunostained for harmonin, F-actin, and MYO7A. Harmonin staining was indistinguishable between WT and *Myo7a-ΔC*, while severe mislocalization (formation of aggregates in the cuticular plate) was observed in *Myo7a full KO* mice. Scale bar=10 μm. **B-C**. Harmonin immunoreactivity at the UTLDs in WT and *Myo7a-ΔC* IHCs at P7. Compared to WT, the harmonin signal is slightly increased at the UTLD of *Myo7a-ΔC* IHCs. For quantification, harmonin fluorescence intensities in ~8 stereocilia per cell (longest stereocilia UTLD only) were measured using ImageJ, normalized to phalloidin-reactivity at the same site, and a mean intensity was determined for each cell. Mean normalized intensities of harmonin at the UTLD of the stereocilia: WT=0.40±0.092, *Myo7a-ΔC*=0.47±0.093, p = 2.34e-2. P-values were derived from two-tailed, unpaired t-tests. Number of UTLD (cells; animals): WT= 167 (16; 3), *Myo7a-ΔC*= 209 (17; 4). For statistical analysis, each data point represents the mean normalized harmonin immunofluorescence per cell. Error bars indicate SD. Scale bar=10 μm. The plot is shown as mean±SD. **D, E**. ADGRV1 immunoreactivity at the stereocilia base was not significantly changed in *Myo7a-ΔC* IHCs at P7 compared to WT. ADGRV1 immunofluorescence intensity (from the middle cochlear region) was determined for each cell and normalized to

background immunofluorescence in the cuticular plate region of the same cell. For statistical analysis, an average of ~6 cells per animal were analyzed. Each data point represents normalized ADGRV1 immunofluorescence per cell, averaged per animal (n=7 animals for both WT and *Myo7a-ΔC*). Scale bar=1μm. P-values were derived from two-tailed, unpaired t-tests. The plot is shown as mean±SD.

3.5. Reduced MET resting open probability and slowed MET current kinetics in *Myo7a-ΔC* IHCs

Despite an 85% reduction in total MYO7A levels, IHCs in *Myo7a-ΔC* mice exhibited WT-like hair bundle morphology in the first two postnatal weeks as observed by light and scanning electron microscopy (Fig. 3-2D, E). Furthermore, harmonin localization was not affected in *Myo7a-ΔC* IHCs (Fig. 3-5B, C), suggesting that the reduction of MYO7A did not affect the overall composition and integrity of the tip link motor complex at the UTLD. The *Myo7a-ΔC* IHCs therefore provided a powerful tool to directly and specifically test the role of MYO7A in hair cell MET, without the confounding effects arising from defects in hair bundle development or MET complex integrity.

To examine the potential contribution of MYO7A-C to MET characteristics, we conducted whole-cell voltage-clamp recordings in the middle-apical turn of WT and *Myo7a-ΔC* IHCs with a fluid jet to deflect the hair bundle. Using a high-speed imaging system, we could also measure the hair bundle deflection during the fluid-jet stimulation (Fig. 3-6A). We chose fluid jet stimulation as opposed to stiff probe stimulation since the fluid jet can stimulate all the stereocilia in IHC hair bundles without biasing stereocilia. These are problems the stiff probe has due to the bulky shape to stimulate IHCs and the necessity of touching the stereocilia. To determine if MYO7A-C is involved in set-point regulation of the MET channel, we used sinusoidal hair bundle stimulation to quantify the MET channel resting open probability (P_o). To increase the sensitivity of our assay, we used an intracellular solution containing 10 mM BAPTA, a calcium chelator, which increases the WT resting open probability (Fig. 3-6B)[112,113]. The resting P_o of the MET channel in IHCs was severely affected in *Myo7a-ΔC* mice, decreasing from 8.6 ± 3.9% in WT to 3.3 ± 1.2% in *Myo7a-ΔC* IHCs (p = 5.7e-5) (Fig. 3-6B, C, arrowheads indicate near absent negative current in IHC *Myo7a-ΔC*). In basal OHCs, in which MYO7A levels were unaffected in

Myo7a-ΔC mice, we would not expect a change in resting open probability. Indeed, we found no change in resting P_o (Fig. 3-6D, p = 0.60). Next, to examine changes to the current vs displacement (activation) curves, we measured MET currents in response to fluid-jet step stimuli (Fig. 3-6D). Peak currents showed no significant change between WT and mutant IHCs (p = 0.43) (Fig. 3-6F), but the activation curves between the WT and mutant IHCs showed a rightward shift (x_o, p = 0.011) and the resting P_o was significantly reduced (Fig. 3-6D, E, G; p = 6.0e-4). No significant differences were observed with similar experiments in basal OHCs, which served as an additional control (x_o, p = 0.39 and resting P_o, p = 0.67). Of note, the resting P_o of ~15% in WT OHCs (as opposed to 50% in some reports[112–114]) is due to the high extracellular calcium concentration and high intracellular calcium buffer used for the present recordings. We ensured that all measurements have clamp time constants that are two-fold shorter than the process measured. These data are consistent with MYO7A-C having a role in setting tip-link tension.

Decreases in tip-link tension in OHCs have been connected with the slowing of MET activation[100]. To determine whether MET channel activation is altered in IHCs of *Myo7a-ΔC* mice, we analyzed the step response kinetics. We determined the $t_{10\%}$, which is the time for the current and motion to reach 10% of their maximum value (in Fig. 3-6H-J). Across the entire stimulus range (50, 75, 100% P_o), *Myo7a-ΔC* IHCs exhibited a significant delay in the $t_{10\%}$ of the onset of the current (two-way ANOVA, p=4.4e-6) (Fig. 3-6J), but not the motion (two-way ANOVA, p=0.48) (Fig. 3-6I). Since there is no delay in the motion, the hair bundle begins its movement at the same time. Even though the fluid jet stimulus has a rise time of ~0.5ms[115], it was fast enough to dissect differences in current onset between WT and *Myo7a-ΔC* hair cells. The delay in the current onset is consistent with the tip link tension being slack prior to the onset of the stimulus requiring extra time to engage and provide tension on the MET channel.

The opposite effect occurred for the t_{10-90}, which is the time for the current and motion to go from 10% to 90% of their maximum value. Here, the rise of the current was comparable between WT and mutant IHCs, but the rise of motion was prolonged significantly (two-way ANOVA, current: p = 0.24, motion: p = 4.0e-4). The effect on the kinetics of the hair bundle motion suggests some mechanical changes in the hair bundle due to the loss of MYO7A-C. We previously determined that the fluid-jet force plateaus ~0.5ms after stimulus onset, and the hair bundle will continue to move even after the force has plateaued[115]. The continued motion, which we term “creep”, allows us to measure mechanical changes in the hair bundle. We fit the creep with a double-exponential decay function, which we previously found to provide a better fit than a single exponential decay[115]. Comparing WT and *Myo7a-ΔC* mice, we found that the creep was greater in *Myo7a-ΔC* mice with a larger contribution of the slower creep component (2-way ANOVA: A2 – the magnitude of the slower creep component p = 0.043; (A2 / (A1 + A2) – relative magnitude of the slower creep component, p = 2.2e-4; (A1 + A2)/y0 – relative magnitude of the creep compared to the total displacement of the hair bundle, p = 1.0e-4). The differences in motion suggest that the mechanical properties of the hair bundle are altered in *Myo7a-ΔC* mice.

All taken together, the characteristics of both the MET current and hair bundle motion in *Myo7a-ΔC* IHCs are consistent with the hypothesis that MYO7A-C generates tension within the IHC MET complex.

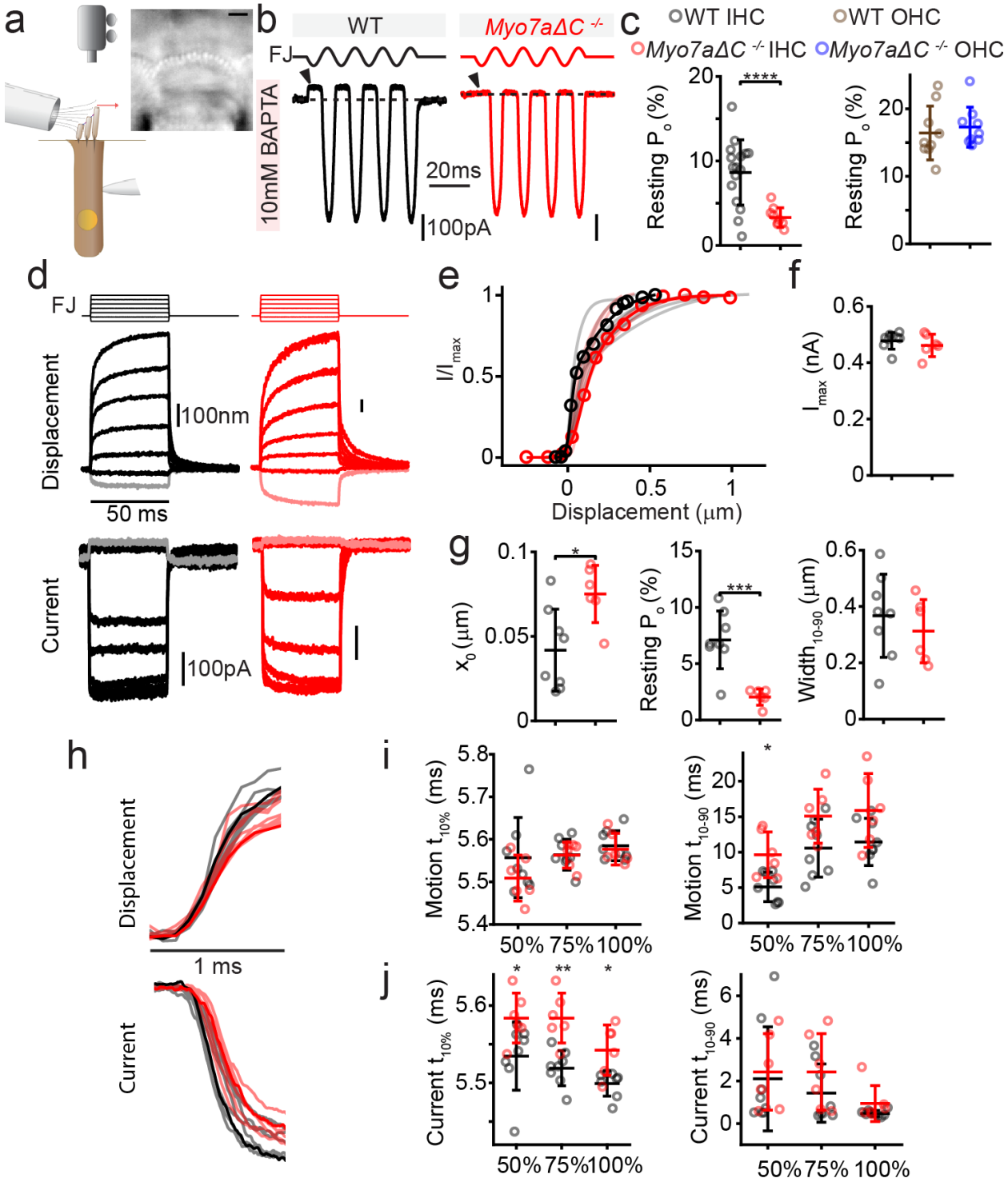

Figure 3-6. Reduced MET resting open probability and slowed MET current kinetics in *Myo7a-ΔC* IHCs

A. Schematic illustration of the experimental approach. A fluid jet was used to deflect the hair bundle. MET currents and hair bundle movements were analyzed by patch-clamp

electrophysiology and high-speed imaging, respectively (see methods). A sample image from a recorded video is also shown. Scale bar = 2 μm. **B**. MET responses of middle-apical IHCs to sinusoidal bundle stimulation with a 10 mM intracellular BAPTA solution. Arrowheads point to amount of current shut off during the negative phase of the stimulation. The current between the dotted line and the arrowhead represents the resting current. We defined the maximum MET current as the difference between the maximum and minimum recorded current. Resting P_o is estimated by resting current divided by the maximum MET current. Cells were held at -80 mV holding potential. **C**. Resting P_o summary data from sine wave experiments in b. Resting P_o is significantly decreased (p = 5.7e-5, WT = 8.6 ± 3.8%, n = 16; *Myo7a*-ΔC= 3.3 ± 1.2%, n = 9) in *Myo7a-ΔC* IHCs. Raw data is shown as light-colored circles (gray = WT, red = *Myo7a-ΔC*), with the mean and SD overlaid as solid color bars. Similar experiments in OHCs in the basal turn of the cochlea where no major difference in *Myo7a* expression was observed showed no significant change in resting P_o (p = 0.60, WT = 16.4 ± 4.0%, n = 9; *Myo7a-ΔC*= 17.3 ± 3.0%, n = 9). **D**. MET responses of middle-apical IHCs to step-like force stimulation in 10 mM intracellular BAPTA solution. FJ indicates the driving voltage waveform delivered by the fluid jet. Displacement traces were extracted by analysis of the high-speed imaging data, and current traces were recorded in voltage clamp. The largest negative stimuli are shaded lighter to show the MET current on at rest. **E**. Current vs displacement plots (activation curves) for the data from d. Light colored traces show all the activation curve fits of all cells recorded. f. Summary data of peak currents for cells recorded in 10 mM BAPTA showed no significant change (p = 0.43). **G**. Summary data for parameters describing the activation curves in *Myo7a-ΔC* mice are right shifted as compared to controls (p = 0.011), which is consistent with the reduced resting P_o (p = 6e-4). **H**. When zooming in on the onset (1 ms timeframe), the there was no difference in the initial rise of the hair bundle displacement, but there was a delay in the current onset. The step eliciting ~75% peak currents are shown for all cells with the data from panel d shown with darker colors. **I**. The motion and the current onsets were analyzed for the steps eliciting close to 50%, 75%, and 100% peak current.

When analyzing the rise time for the motion, there was no difference in the onset time (time to reach 10% of the maximum motion, t10%) but there was a difference in the time to go from 10% to 90% of the maximum value (t10-90). **J**. On the other hand, the time for the current to reach 10% of the maximum value was delayed in *Myo7a-ΔC* mice by about 0.05 ms (p = 3.3e-2, 2.6e-3, and 2.1e-2 for steps that were closest to 50%, 75%, and 100% peak current, respectively). The current rise time (t10-90) was not significantly affected. The motion rise time was slowed (p=4.0e-3). The summary plot of panels **C, F, G, I**, and j was represented as mean±SD.

3.6. *Myo7a-ΔC* mice exhibit progressive elevation of ABR thresholds, while DPOAE output is unaffected.

We next examined the hearing performance in the *Myo7a-ΔC* mice at various ages. Auditory brainstem response (ABR) thresholds at early ages (P17) were only mildly affected (ABR thresholds were shifted between 10-30 dB depending on test frequency). However, thresholds increased with age, leading to near profound deafness at the age of nine weeks (Fig. 3-7A). In contrast, distortion product otoacoustic emissions (DPOAEs), a measure of OHC function, were unaffected at all ages tested (Fig. 3-7B). Despite a significant reduction of MYO7A in vestibular utricles (by 63%) (Fig. 3-2B), the *Myo7a-ΔC* mice exhibited no obvious circling behavior at four weeks of age, which contrasts with the *full Myo7a KO* mice which exhibited extensive circling and head bobbing behavior.

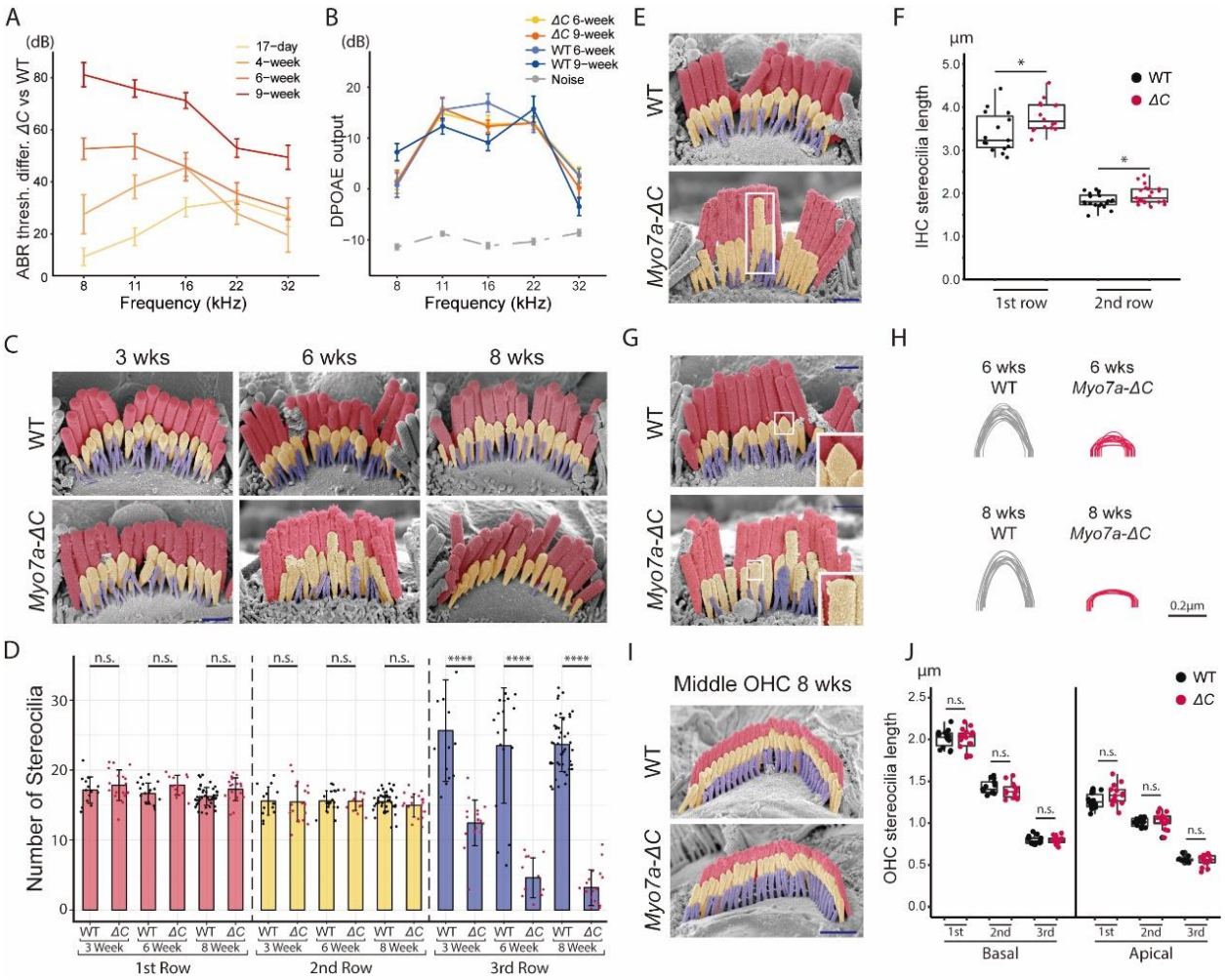

Figure 3-7. Progressive hearing loss and IHC stereocilia degeneration in *Myo7a-ΔC* mice

A. Auditory brainstem response (ABR) thresholds between *Myo7a-ΔC* and age-matched WT controls. Threshold differences increase progressively. Error bars represent standard error (SEM). 2-way ANOVA analyses were performed between *Myo7a-ΔC* and age-matched WTs (p for 17 days=3.38e-29, 4 wks =1.62e-21, 6 wks =5.68e-44, and 9 wks =2.22e-54). Number of mice for ABR measurements: WT: 17 days=13, 4 wks=7, 6 wks=14, 9 wks=13. *Myo7a-ΔC*: 17-day=17, 4-wks=22, 6-wks=18, 9-wks=11. **B**. Distortion product otoacoustic emissions (DPOAE) of *Myo7a-ΔC* and WT controls at 6 wks and 9 wks of age. No significant difference in DPOAE output between WT and *Myo7a-ΔC* by 2-way ANOVA (p = 0.69 at 4 wks and 0.83 at 9 wks). The number of mice for DPOAEs: 6 wks: WT=9, *Myo7a-ΔC*=20; 9 wks: WT=16, *Myo7a-ΔC*=13. **C-D**. SEM analysis of *Myo7a-ΔC* and WT IHCs at 3 wks, 6 wks, and 8 wks of age. The longest, middle and

shortest row of stereocilia are shown in red, yellow, and blue, respectively. The third row of stereocilia degenerates in *Myo7a-ΔC* IHCs and is nearly abolished at 8 wks of age. Quantification of the stereocilia numbers of *Myo7a-ΔC* and WT IHCs shows that the number of the third-row stereocilia in *Myo7a-ΔC* IHCs decreases significantly compared to WT at 3 wks: p = 7.33e-06, average stereocilia number: WT=25.64±7.25, *Myo7a-ΔC*=12.44±3.26; the number of cells (animals): WT=14 (5), *Myo7a-ΔC*=18 (6); 6-weeks: p = 7.28e-23, the average of stereocilia number: WT=23.50±8.26, *Myo7a-ΔC*=4.61±2.84. Number of cells (animals): WT=36 (6), *Myo7a-ΔC*=20 (5); at 8-weeks: p = 9.41e-26, average of stereocilia number: WT=23.66±3.86, *Myo7a-ΔC*=3.21±2.57; number of cells (animals): WT=35 (3), *Myo7a-ΔC*=31 (3). Error bars represent mean±SD. P-values were derived from two-tailed, unpaired t-tests. Scale bar 1μm. **E**. The first and second-row stereocilia of *Myo7a-ΔC* IHCs are more irregular and, on average longer than the WT counterparts. The IHC images are collected from the middle turn of the cochlea. The white box indicates second-row stereocilia in *Myo7a-ΔC* IHC with irregular lengthening. **F**. Quantification of the lengths of the first and second row stereocilia at 6 wks: Lengths of the first row (averaged per cell): WT=3.41±0.47, *Myo7a-ΔC* =3.78±0.35, p = 0.021; the number of stereocilia (WT: 95; *Myo7a-ΔC*=86), number of cells (WT=15; *Myo7a-ΔC*=16), number of animals (WT=5, *Myo7a-ΔC*=5). Lengths of second row: WT=1.83±0.17, *Myo7a-ΔC* =1.96±0.21, p = 0.033. The number of cells (WT=20, *Myo7a-ΔC*=21), the number of animals (WT=3, *Myo7a-ΔC*=3). P-values were derived from two-tailed, unpaired t-tests. Scale bar 1μm. Boxplots show medians, 25th, and 75th percentiles as box limits and minima and maxima as whiskers. **G-H**. The second-row stereocilia in 6 wks old *Myo7a-ΔC* IHC have rounded tips, while the age-matched WT controls have the characteristic prolate tips. For better visualization, the tips of the second-row stereocilia were traced and superimposed. Scale bar 1μm. **I-J**. OHC bundles at 8 wks were not affected in *Myo7a-ΔC* mice. Quantification of stereocilia lengths using SEM images: Basal OHCs: Lengths of first row: WT=1.27±0.094, *Myo7a-ΔC* =1.34±0.12, p = 0.089. Number of stereocilia (WT=188, *Myo7a-ΔC*=153), number of cells (WT=14, *Myo7a-ΔC*=12), number of animals (WT=5, *Myo7a-*

ΔC=4). Lengths of second row: WT=1.01±0.050, *Myo7a-ΔC* =1.032±0.096, p = 0.52. Number of stereocilia (WT=188, *Myo7a-ΔC*=153), number of cells (WT=14, *Myo7a-ΔC*=12), number of animals (WT=5, *Myo7a-ΔC*=4). Lengths of third row: WT=0.57±0.031, *Myo7a-ΔC* =0.55±0.069, p = 0.58. Number of stereocilia (WT=188, *Myo7a-ΔC*=153), number of cells (WT=14, *Myo7a-ΔC*=12), number of animals (WT=5, *Myo7a-ΔC*=4). Apical OHCs: Lengths of first row: WT=2.01±0.10, *Myo7a-ΔC* =1.99±0.13, p = 0.688. Number of stereocilia (WT=131, *Myo7a-ΔC*=137), number of cells (WT=13, *Myo7a-ΔC*=18), number of animals (WT=3, *Myo7a-ΔC*=4). Lengths of second row: WT=1.43±0.082, *Myo7a-ΔC* =1.39±0.082, p = 0.21. Number of stereocilia: (WT=99, *Myo7a-ΔC*=94), number of cells (WT=13, *Myo7a-ΔC*=14), number of animals (WT=4, *Myo7a-ΔC*=3). Lengths of third row: WT=0.80±0.049, *Myo7a-ΔC* =0.80±0.045, p = 0.95. Number of stereocilia (WT=99, *Myo7a-ΔC*=94), number of cells (WT=13, *Myo7a-ΔC*=14), number of animals (WT=4, *Myo7a-ΔC*=3). Scale bar 1μm. P-values were derived from two-tailed, unpaired t-tests. Boxplots show medians, 25th, and 75th percentiles as box limits and minima and maxima as whiskers.

3.7. Transducing rows of IHC stereocilia degenerate in *Myo7a-ΔC* mice

Myo7a-ΔC mice presented with a hearing loss phenotype that was consistent with the specific reduction of MYO7A in IHCs and not OHCs. We therefore used SEM analyses to investigate ultrastructural correlates of IHC dysfunction in mature mice. Previous studies have shown that loss of MET causes stereocilia regression[10,105]. We therefore predicted similar stereocilia phenotypes in the *Myo7a-ΔC* IHCs. At three weeks of age, when the ABR thresholds in the *Myo7a-ΔC* mice are shifted by 10-30 dB compared to WT, the stereocilia of IHCs appear similar to the WT controls, but a closer analysis revealed that the numbers of the shortest stereocilia (in the third row) were significantly reduced (Fig. 3-7C, D). This phenotype progressed with age, and at eight weeks, most third-row stereocilia were absent in the *Myo7a-ΔC* mice (Fig. 3-7C, D). No differences were detected in the numbers of the first and second row of IHC stereocilia (Fig. 3-7C, D).

We next measured the lengths of the longest and second row of stereocilia. Interestingly, both rows, as quantified at six weeks, were slightly longer than their WT counterparts (Fig. 3-7E, F). Importantly, the second row of stereocilia exhibited a marked loss of prolate tips at six and eight weeks of age (Fig. 3-7G, F), consistent with a reduction in tip-link tension[116]. At no time tested were OHC morphologies affected in *Myo7a-ΔC* mice (Fig. 3-7I, J). In summary, the morphological phenotype observed in the mechanosensory hair bundles of *Myo7a-ΔC* mice is consistent with a reduced function of the tip-link tensioning mechanism, specifically in IHCs.

4. Chapter 4: Identification of a novel isoform of Myo7a in sensory hair cells

4.1. Survey of novel *Myo7a* isoform:

Two major types of *Myo7a* isoforms are reported in multiple genomic databases: the canonical isoform (*Myo7a-C*) and the short isoform (*Myo7a-S*). These two isoforms differ in their transcriptional start sites and translational start sites (ATG), resulting in distinct N-terminus extensions (NTEs) of the motor domain (Fig. 4-1B). In the previous chapter, we have reported that *Myo7a-C* is predominantly expressed in the cochlear IHCs at all regions of the cochlea and displays a tonotopic gradient in OHCs. We also showed that MYO7A-C is essential in tensioning the mechano-electro transduction (MET) complex. However, the existence and the function of the reported *Myo7a*-S, and possibly other isoforms, remained to be elucidated. For a complete characterization of *Myo7a* isoforms with alternative NTEs, we therefore performed a 5' rapid amplification of cDNA ends (5' RACE) experiment on cDNA of P0. Surprisingly, we failed to identify *Myo7a-S* transcript from our 5' RACE cDNA libraries, suggesting that this isoform, if expressed at all, is of low abundance in cochlear hair cells. Instead, we identified a previously unreported isoform of *Myo7a*, which we termed *Myo7a-N* (Novel) (Fig. 4-1C).

Like *Myo7a-C* and *Myo7a-S*, *Myo7a-N* is generated by an alternative transcriptional start site. Sequencing showed that *Myo7a-N* has a unique first exon with a length of 145 bp: the first 31 nucleotides of this exon belong to an untranslated region, and the rest of the exon encodes a 36 amino acid sequence. In comparison, as previously reported, *Myo7a-C* has an 11-aa N-terminus extension compared with *Myo7a-S*. (Fig. 4-1B)

The 36 aa long NTE of MYO7A-N is conserved across multiple vertebrate species, including mouse and humans, suggesting that MYO7A-N has an important role in the

auditory system evolutionarily (Fig. 4-1D). Previous studies MYO1C and MYO15[70,71,117–119] indicated that NTEs fine-tune the motor activities of myosin motor domains. For a preliminary assessment of structural differences between the NTEs of MYO7A-C and MYO7A-N, we predicted the secondary structure of MYO7A-N NTE by using Alphafold2[120,121]. Our analysis showed that the MYO7A-N is rich in proline, valine, and leucine, which contributes to high hydrophobicity. The proline-rich property also might contribute to a higher structural rigidity [122]. However, Alphafold2 predicted the MYO7A-N NTE to be highly unstructured and we were not able to deduce functional clues from Alphafold2 analysis.

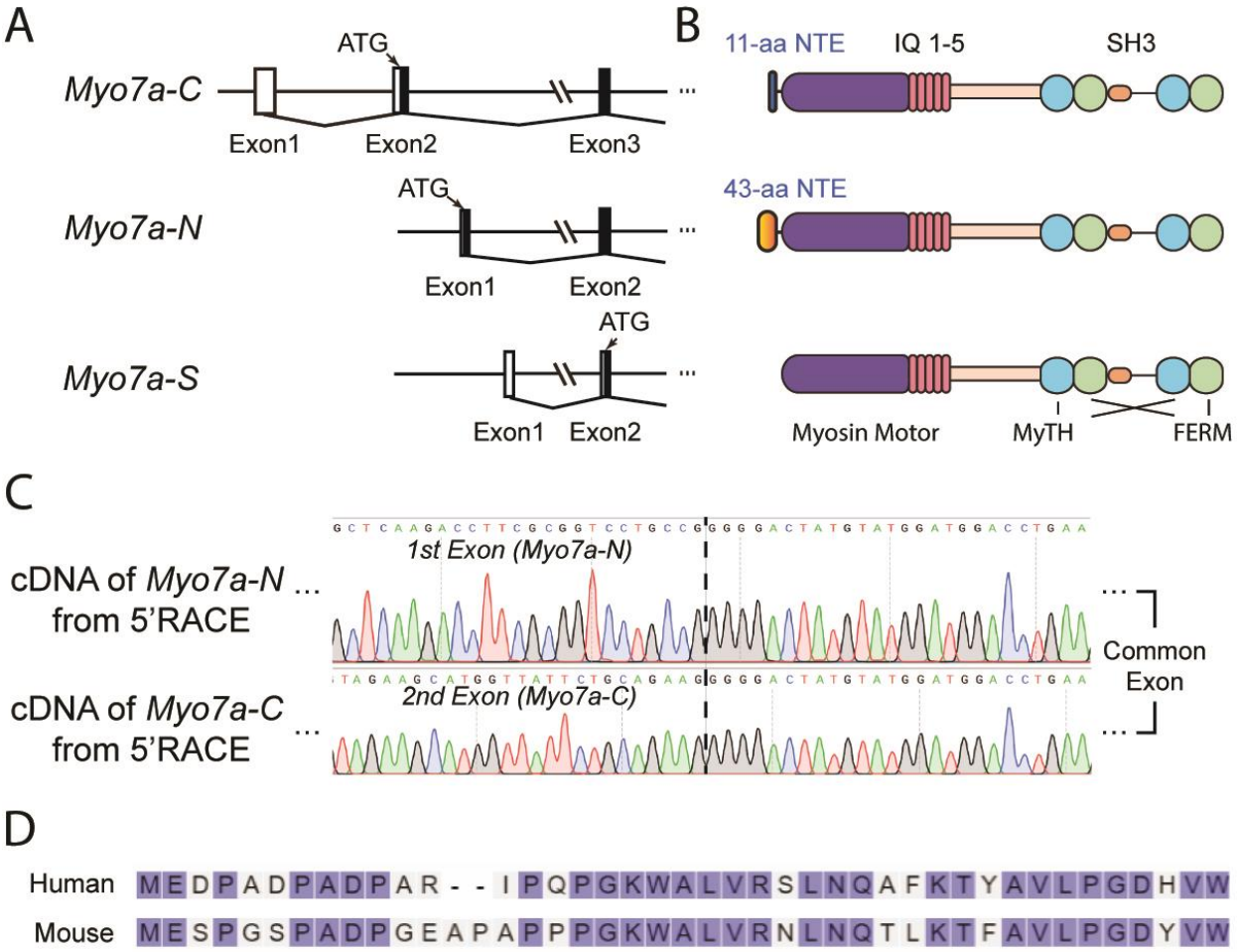

Figure 4-1: Identification of MYO7A-N by 5' RACE

A. A diagram of the 5' end of *Myo7a* isoforms. *Myo7a* has three different isoforms: *Myo7a-C* and *Myo7a-S* are reported in the genomic database. The function of MYO7A-C is described in the previous chapter, while the existence of *Myo7a-S* in the auditory system is not clear. *Myo7a-N* is a new isoform that is identified in the cochlea cDNA, which has a unique coding first exon. These three isoforms are generated by different transcriptional start sites and translational start sites (ATG). **B**. Illustration of protein domains of MYO7A isoforms. Compared to MYO7A-S, MYO7A-C has a 11-amino acid extension at N-terminus. The newly discovered isoform of MYO7A-N has a 43-aa N-terminus extension. **D**. Sequencing result of *Myo7a-C* and *Myo7a-N* transcript from 5' RACE cDNA library. *Myo7a-C* and *Myo7a-N* have unique first coding exon. These to isoforms begin to share common coding sequence from the 3rd exon of *Myo7a-C* (2nd exon of *Myo7a-N*).

E. Protein BLAST analysis shows that the N-terminus extension of MYO7A-N is converted between humans and mice.

4.2. MYO7A-C and MYO7A-N are major isoforms in the cochlea:

To quantify the transcript levels of the different *Myo7a* isoforms, we performed quantitative polymerase chain reaction (qPCR). To detect the *Myo7a-C*, *Myo7a-N*, and *Myo7a-S* transcripts separately, we designed qPCR primers that target their unique first exons. We collected cochlear mRNA at P0 and P20 to trace expression level changes of *Myo7a* isoforms at different developmental stages. Consistent with our 5' RACE result, *Myo7a-C* and *Myo7a-N* isoforms were the most abundant isoforms in the P0 cochlear cDNA. The transcript of *Myo7a-S* was detectable but with a substantially lower level than other isoforms (Fig. 4-2A)

We also observed changes in *Myo7a-C* and *Myo7a-N* expression levels during postnatal development (as assessed at P0 and P20). The total level of *Myo7a* transcript is not significantly changed between P0 and P20 (Normalized percentage: P0= 0.70, P20=0.74; p-value=0.82), while the ratio of different isoforms changed during hair cell maturation: the transcript level of *Myo7a-C* increased by approximately 2.5-fold from P0 to P20 (Normalized percentage: P0= 0.17, P20=0.42; p-value=0.011(*)). Contrastingly, the *Myo7a-N* decreased ~2.5 fold, although the T-test suggests that the level change is not significant (Normalized percentage: P0=0.14, P20=0.056; p-value=0.12). Finally, the transcript level of *Myo7a-S* further decreased (Normalized percentage: P0=0.0095, P20=0.0017; p-value=0.060). This result suggests that the *Myo7a-C* and *Myo7a-N* are the predominant isoforms in the cochlea, and that their expression levels are refined during cochlea maturation (Fig. 4-2A).

Although *Myo7a-S* is expressed at low levels, it is still possible that it has an indispensable role in hair cell development or function at early stages. We tested this using two mouse models. First, we generated a mouse line in which both *Myo7a-C* and *Myo7a-N* were deleted simultaneously. This mouse line was created by introducing a frameshift mutation

in the common reading frame of the *Myo7a-C* and *Myo7a-N*, but upstream of the start codon of *Myo7a-S*. This allowed us to disrupt the translation of the MYO7A-C and MYO7A-N, without affecting MYO7A-S expression. We named this mouse line *Myo7a-ΔCN* mouse (Fig. 4-2B). In addition, we sought to generate a mouse line in which only *Myo7a-S* is disrupted. Because the start codon of the *Myo7a-S* isoform is located in the shared reading frame of the *Myo7a-C* and the *Myo7a-N* isoforms, it was not possible to delete *Myo7a-S* without affecting other isoforms by introducing a frameshift mutation. As an alternative method, we deleted the entire non-coding first exon of *Myo7a-S*, which theoretically should prevent the transcription *Myo7a-S*. This mouse line was named *Myo7a-ΔS*. (Fig. 4-2B)

First, we characterized the expression pattern of MYO7A in the *Myo7a-ΔCN* and *Myo7a-ΔS* mouse lines using a pan-MYO7A antibody. At P5, MYO7A immunofluorescence was nearly abolished in all hair cells of *Myo7a-ΔCN* mice. In contrast, we did not observe a noticeable reduction of MYO7A immunoreactivity in *Myo7a-ΔS* cochlea hair cells. This result was consistent with our qPCR analysis and confirmed that MYO7A-C and MYO7A-N are the major isoforms in cochlear hair cells also at the protein level. (Fig. 4-2C)

Next, scanning electron microscopy (SEM) was used to examine the hair bundle morphology in *Myo7a-ΔCN* mice at P0 and P20 (Fig. 4-2D-E). Considering the near complete loss of MYO7A signal in P0 *Myo7a-ΔCN* hair cells, we were expecting these hair cells to show disorganized hair bundle morphology. Interestingly, compared with the *Myo7a-Full KO* mice, both IHCs and OHCs of *Myo7a-ΔCN* showed WT-like hair bundle development at P0 (Fig. 4-2D). This result suggests that the level of remaining isoforms of MYO7A, likely MYO7A-S, is sufficient for hair bundle development at early postnatal stages. However, by postnatal day 20, the hair bundle morphology in *Myo7a-ΔCN* mice had degenerated to a degree comparable to age-matched *Myo7a-Full KO* mice (Fig. 4-

2E). This morphological deterioration of the hair bundle suggests the level of remaining MYO7A was not sufficient to maintain the hair bundle morphology[94,123,124].

Finally, we tested whether MYO7A-S has a functional relevance in hearing performance. Auditory brainstem response (ABR) and distortion product otoacoustic emissions (DPOAE) were conducted on the *Myo7a-ΔCN* and *Myo7a-ΔS* mice at P20 (Fig. 4-2F). The *Myo7a-ΔS* mice did not show any significant change in ABR threshold or DPOAE response (statistical analysis result in Fig. 4-2F legend), suggesting that *MYO7A-S* does not have a specific role in hearing performance or cochlea amplification. In contrast, the *Myo7a-ΔCN* mice showed profound hearing loss at P20 (Fig. 4-2F), consistent with the disorganized hair bundle morphology shown by SEM (Fig. 4-2E).

We therefore conclude that *MYO7A-S* is expressed at low levels during early development but does not have a specific role in hair cell development, hair bundle maintenance, or hearing function. Correspondingly, we decided to focus on the functional differences between the MYO7A-C and the MYO7A-N in the remainder of our studies.

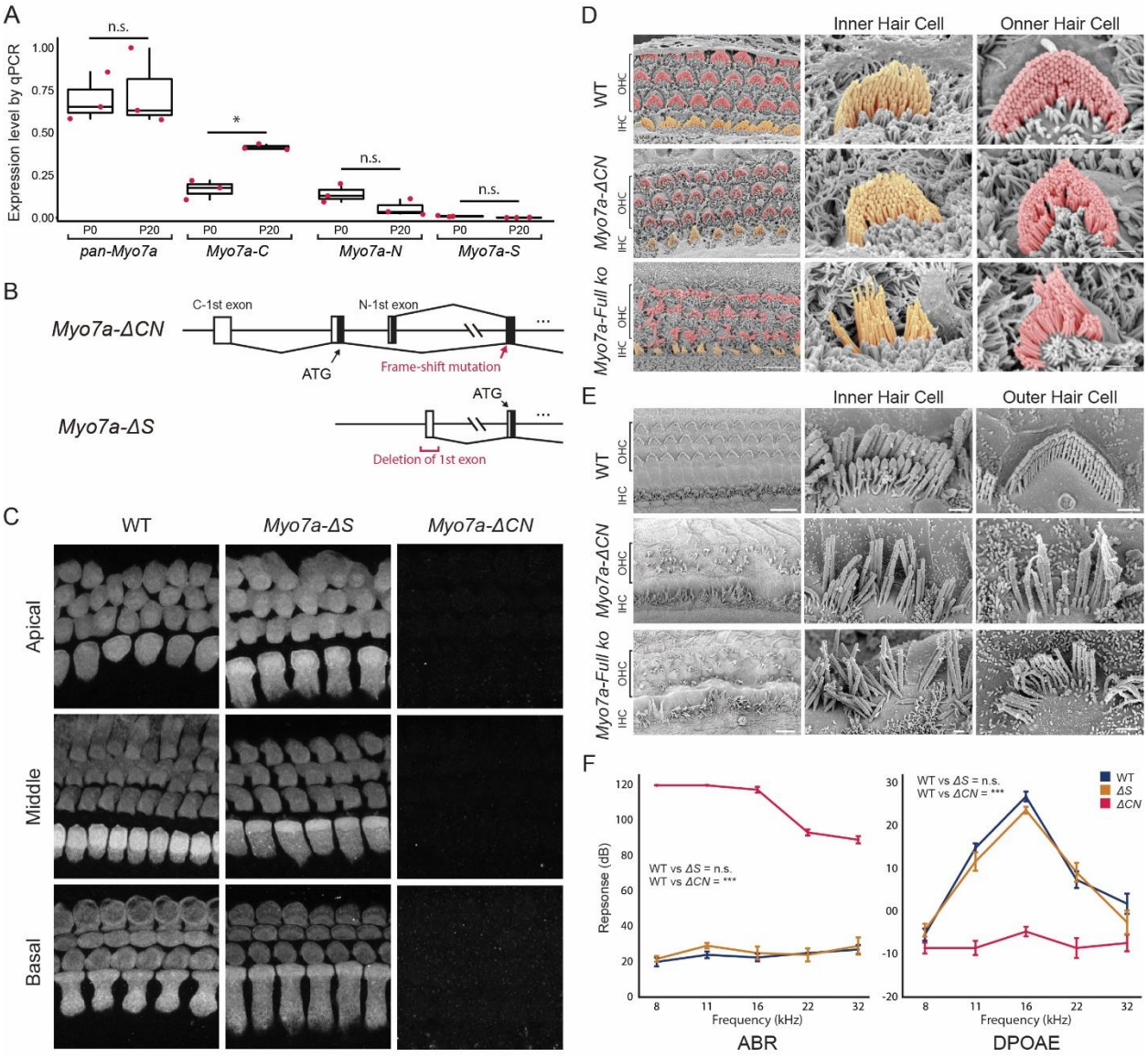

Figure 4-2: *Myo7a-C* and *Myo7a-N* are the major isoforms in cochlear hair cells.

A. Normalized expression level of *Myo7a* isoforms at P0 and P20 measured by qPCR. The transcript level is normalized to *Gapdh*. Compared to *Myo7a-C* and *Myo7a-N*, *Myo7a-S* has a low expression level in cochlea cDNA (Each datapoint represent an individual cDNA preparation. Each cDNA preparation has 8~9 cochleae. T-test p-value of each isoform P0 vs. P20: *pan-Myo7a*=0.82, *Myo7a-C*=0.011, *Myo7a-N*=0.1162, *Myo7a-S*=0.060). Boxplots show medians, 25th, and 75th percentiles as box limits and minima and maxima as whiskers. **B**. A Diagram of the generation of *Myo7a-ΔCN* and *Myo7a-ΔS* mice. To generate *Myo7a-ΔCN* mouse line, a single nucleotide deletion is introduced in the coding sequence of both *Myo7a-C* and *Myo7a-N* but not

Myo7a-S. To generate the *Myo7a-ΔS* mouse, the first non-coding first exon is mutated to GTG (ATG to GTG). **C**. Immunohistochemistry imaging of wildtype (WT), *Myo7a-ΔS*, and *Myo7a-ΔCN* mice at P0. *Myo7a-ΔS* has WT-like MYO7A immunofluorescent intensity in both IHCs and OHCs. In contrast, *Myo7a-ΔCN* mice showed a nearly abolished MYO7A signal, which is similar to *Myo7a-full KO mice*. **D**. SEM of WT, *Myo7a-ΔCN,* and *Myo7a full KO* mouse cochlea at P0. Although *Myo7a-ΔCN* cochlea showed a substantial reduction in MYO7A level, it retained WT-like hair bundle morphology at P0, while *Myo7a-full KO* mice showed disorganized hair bundle morphology. Scale bar: view of the organ of Corti: 10μm; view of the IHC or OHC: 1μm. **E**. SEM of WT, *Myo7a-ΔCN,* and *Myo7a* full KO mouse cochlea at P20. The reduction of MYO7A in *Myo7a-ΔCN* caused hair bundle disorganization and hair cell loss, which is comparable to *Myo7a-full KO* cochlea. Scale bar: view of the organ of Corti: 10μm; view of the IHC or OHC: 1μm. **F**. ABR and DPOAE test of WT, *Myo7a-ΔCN,* and *Myo7a-ΔS* mice at 4 weeks. *Myo7a-ΔCN* showed profound hearing loss with nearly abolished ABR and DPOAE. *Myo7a-ΔS* mice do not show a significant change in hearing performance. (ANOVA p-value: ABR: WT vs. *Myo7a-ΔCN*: 8.21e-38, WT vs. *Myo7a-ΔS*: 0.20. The number of animals: WT=6 vs. *Myo7a-ΔCN*=6, *Myo7a-ΔS*=6. DPOAE: WT vs *Myo7a-ΔCN*: 1.49e-12, WT vs *Myo7a-ΔS*: 0.19. Number of animals: WT=5 vs *Myo7a-ΔCN*=6, *Myo7a-ΔS*=6). Line-plots show means of the ABR or DPOAE response. Error bars represents standard errors.

4.3. Expression of *Myo7a-C* and *Myo7a-N* are inversely correlated in the cochlea.

Similar to *Myo7a-ΔC* mice, we created a mouse line in which we specifically knocked out *Myo7a-N* by deleting its entire first coding exon (Fig. 4-3A). With these two *Myo7a-ΔC* and *Myo7a-ΔN* mice, we were able to investigate the expression patterns and functional differences of the MYO7A-C and the MYO7A-N in the mouse cochlea. First, to check the expression pattern of these two isoforms, we performed side-by-side immunohistochemistry experiments on *Myo7a-ΔC* and *Myo7a-ΔN* P5 cochleae using a pan-MYO7A antibody. As described in the previous chapter, *Myo7a-ΔC* mice showed a substantial decrease in the MYO7A immunoreactivity in IHCs. (Fig. 4-3B, C). *Myo7a-ΔC* mice also exhibited a tonotopic reduction of MYO7A signal in OHCs, with a stronger reduction at the apical region and a more modest reduction at the cochlear base (Fig. 4-3D). In contrast, *Myo7a-ΔN* mice showed MYO7A reduction mainly in basal OHCs, and this reduction of MYO7A became less pronounced toward the apex of the cochlea. No significant MYO7A signal reduction was observed in *Myo7a-ΔN* IHCs. The analysis of isoform-specific KO mice thus suggested that the expression pattern of the *Myo7a-C* and *Myo7a-N* are inversely correlated in cochlea hair cells: IHCs predominantly express MYO7A-C in all regions of the cochlea. OHCs have a higher *Myo7a-N*/*Myo7a-C* ratio at the basal region of the cochlea, and this ratio inverts toward the apical part of the cochlea. Next, we tested whether this expression pattern persists in adult mice. Using the same immunohistochemistry strategy, we examined the expression pattern of the *Myo7a-C* and *Myo7a-N* at P20. *Myo7a-ΔC* and *Myo7a-ΔN* cochlea at P20 have similar MYO7A reduction patterns as the P5 cochlea. We therefore concluded that the inversely correlated pattern of the two *Myo7a* isoforms is not specific to a certain development stage.

It is well characterized that MYO7A is essential for hair bundle development, and the depletion of MYO7A results in hair bundle disorganization. We therefore investigated the morphology of hair cells and their hair bundles in *Myo7a-ΔN* mice (along with *Myo7a-ΔC* as a control) using SEM imaging. As reported in previous chapter, despite an approximately 80% reduction of MYO7A in IHCs, *Myo7a-ΔC* IHC hair bundles retain WT-like morphology at P7 (Fig. 4-3E). Similarly, *Myo7a-ΔN* basal OHCs, which show the most significant MYO7A reduction, did not show a substantial hair bundle morphological change. In brief, both *Myo7a-ΔC* and *Myo7a-ΔN* mice have WT-like hair bundle development, providing a powerful tool to study the functional differences between MYO7A-C and MYO7A-N isoforms in MET complexes without confounding developmental defects.

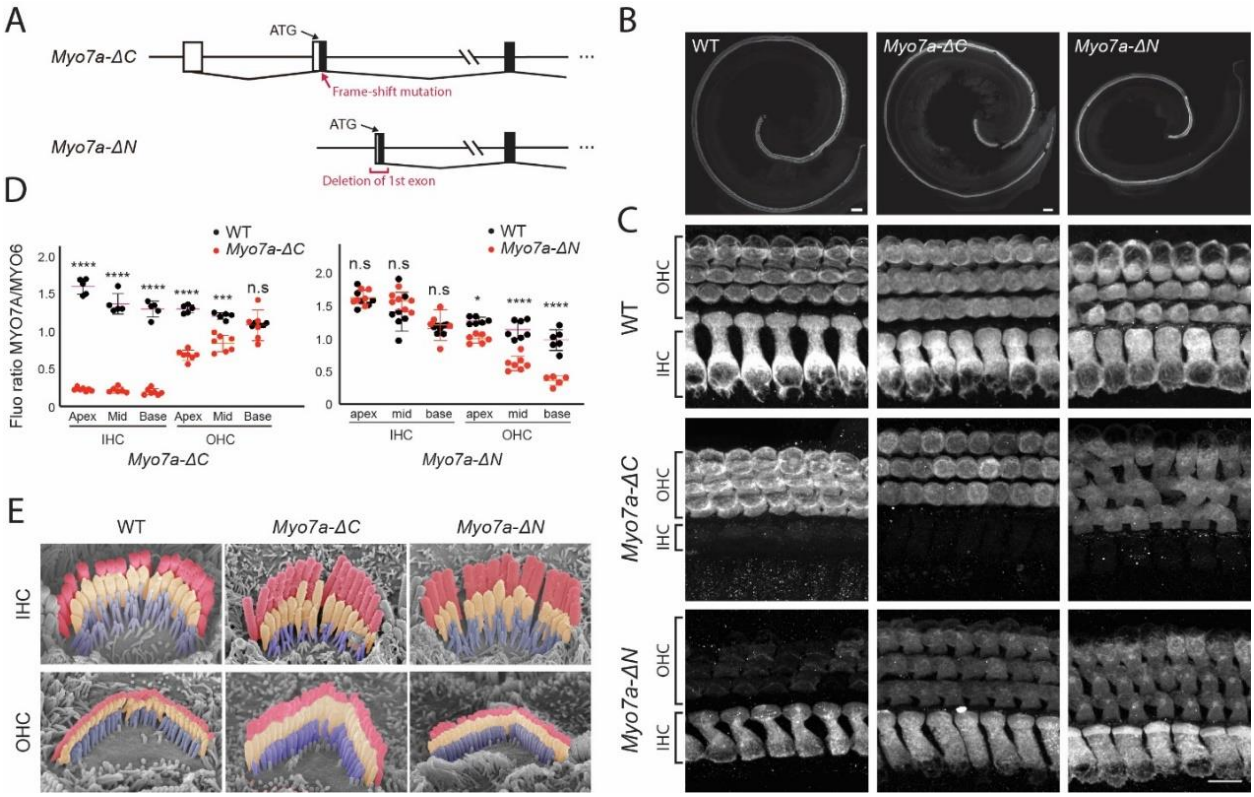

Figure 4-3: Expression of *Myo7a-C* and *Myo7a-N* are inversely correlated in the cochlea.

A. Diagram of the generation of *Myo7a-ΔC* and *Myo7a-ΔN* mice. the first coding exon of *Myo7a-N* is deleted to generate *Myo7a-ΔN* mice. **B**. Whole mount imaging of WT, *Myo7a-ΔC*, *Myo7a-ΔN* mice at P7. **C**. Zoomed-in images of WT, *Myo7a-ΔC*, *Myo7a-ΔN* ko mice at P7 at apical, middle, and basal region. Using a pan-MYO7A antibody. Scale bar=10μm. **D**. Quantification of MYO7A immunofluorescent reactivity of WT, *Myo7a-ΔC*, *Myo7a-ΔN* mice in P7 cochlea. The quantification of fluorescent intensity showed that MYO7A-C and MYO7A-N are inversely correlated in cochlea hair cells. MYO7A immunoreactivity is normalized to MYO6. Boxplots show medians, 25th, and 75th percentiles as box limits and minima and maxima as whiskers. **E**. SEM images of the IHC and OHC of WT, *Myo7a-ΔC*, and *Myo7a-ΔN* at P7. No substantial morphological changes are detected in *Myo7a-ΔC*, and *Myo7a-ΔN* hair cells.

4.4. MYO7A-C and MYO7A-N localize to UTLDs of IHCs and OHCs:

The inversely correlated expression pattern of the *Myo7a-C* and the *Myo7a-N* is inferred from isoform-specific deletion mice. We sought to confirm this expression pattern by direct detection of isoforms. We failed to generate isoform-specific antibodies due to the low antigenicity of the unique NTE sequences. As done for the detection of the *Myo7a-C* isoform, we inserted an HA-tag after the start codon of *Myo7a-N* (Fig. 4-4 A). Using this *HA-Myo7a-N* mouse line, and the previously generated *HA-Myo7a-C* mouse line, we were able to visualize the expression and localization of the two isoforms separately at both tissue and subcellular levels.

We first visualized HA-MYO7A-C and HA-MYO7A-N levels in the P5 cochlea. HA-MYO7A-C was predominantly expressed in IHCs in all regions of the cochlea. (Fig. 4-4 B) It also has a relatively high expression level in the apical OHCs compared to the cochlear base. In contrast, HA-MYO7A-N was mainly expressed in OHCs, with higher levels in the basal region and decreasing toward the apex (Fig. 4-4 B). This inversely correlated expression pattern of the HA-MYO7A-C and HA-MYO7A-N is consistent with the pattern we inferred from isoform-specific deletion mouse lines.

We next investigated the subcellular localizations of MYO7A-N, especially at the functionally important site of the UTLDs. As previously shown for the HA-MYO7A-C mice, we also detected HA-MYO7A-N immunoreactivity at the UTLD of OHCs (Fig. 4-4C). Quantification analysis showed that HA-MYO7A-C is the predominant isoform in IHC UTLDs, consistent with its high expression level in the cell body (Statistical analysis in Fig. 4-4D legend). We also observed a tonotopic gradient of MYO7A-C and MYO7A-N in UTLDs. OHCs have the highest HA-MYO7A-N/HA-MYO7A-C ratio in the basal region, decreasing toward the cochlear apex (Fig. 4-4D).

The pattern of the MYO7A-C and MYO7A-N in UTLDs strongly correlates with their differential expression patterns in the cell body (Fig. 4-3C). Thus, we conclude that both isoforms of MYO7A can be localized to the UTLD, and their amount in UTLDs is likely to be regulated by their expression levels in the cell body.

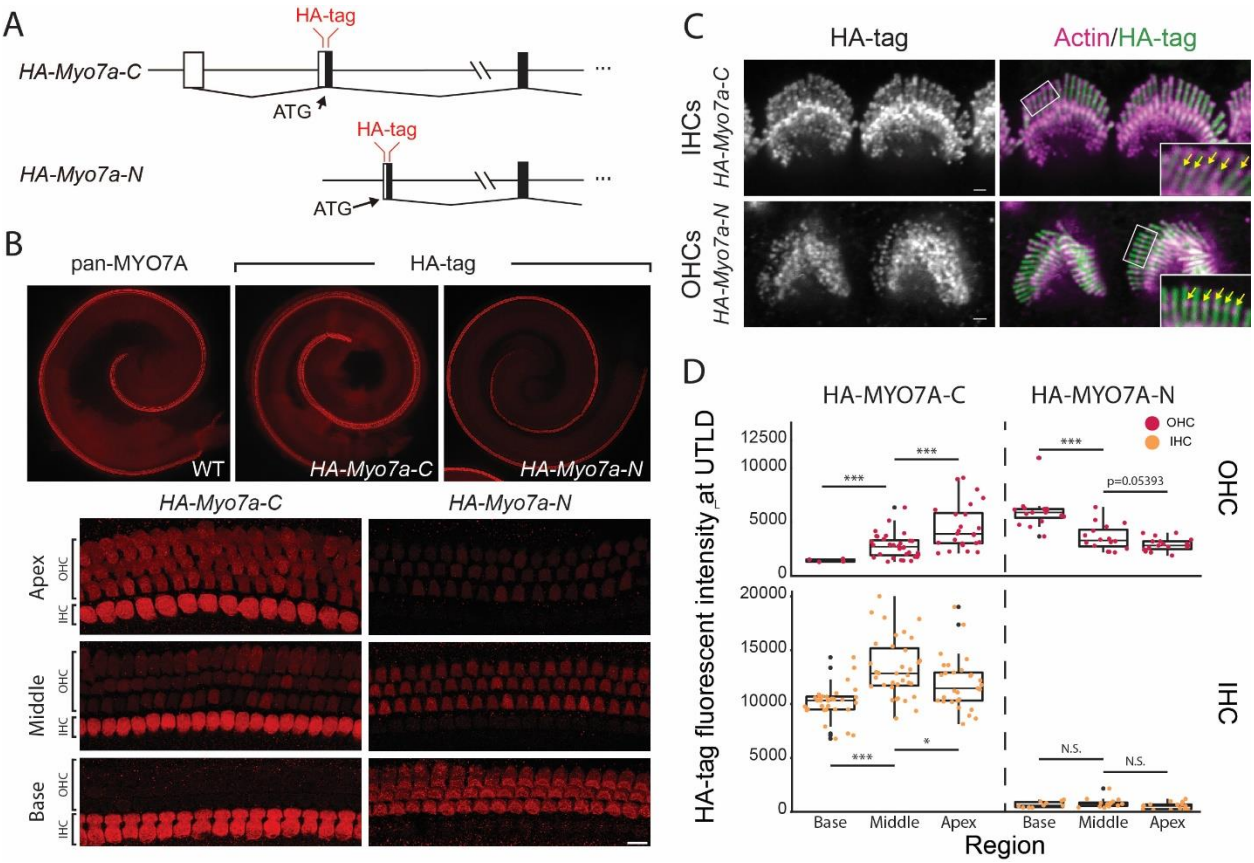

Figure 4-4: **Both MYO7A-C and MYO7A-N localize to UTLDs of IHCs and OHCs**

A. Diagram of the generation of *HA-Myo7a-C* and *HA-Myo7a-N* mice. HA-tag sequence is inserted after the translational start sites of *Myo7a-C* and *Myo7a-N*, respectively. **B**. Immunohistochemistry imaging of whole mount WT type, *HA-Myo7a-C* and *HA-Myo7a-N* mice at P5. A pan-MYO7A antibody is used on WT cochlea to show the overall expression pattern of MYO7A. The HA-tag specific antibody is used to visualize HA-MYO7A-C and HA-MYO7A-N in the KI mouse lines. (Scale bar=10μm) **C**. Immunohistochemistry image showing that HA-signal is also detected in the UTLDs of IHCs and OHCs of both HA-MYO7A-C and HA-MYO7A-N mice. (Scale bar=1μm) **D**. Quantification of HA signal in UTLDs of *HA-Myo7a-C* and *HA-Myo7a-N* mice. Similar with their expression pattern in the cell body, the HA signal also showed tonotopic pattern in UTLDs of OHCs. (Statistics: Number of cells (cochlea): OHC: HA-MYO7A-C: base=4 (1) (4 of the cochlea have nearly non-detectable value, which is excluded from T-test), middle=32 (5), apex=24 (5); HA-MYO7A-N: base=16 (4), middle=32 (4), apex =24 (4); IHC: HA-MYO7A-C:

base=32 (4), middle=35 (5), apex =29 (5); HA-MYO7A-N: base=8 (5) (1 of the cochlea have nearly non-detectable value, which is excluded from T-test), middle=16 (5), apex =15 (5). T-test p-value: OHC: HA-MYO7A-C: base vs middle= 4.06e-07, middle vs apex= 0.0007474; HA-MYO7A-N: base vs middle= 4.062e-05, middle vs apex= 0.05393; IHC: HA-MYO7A-C: base vs middle= 1.979e-07, middle vs apex= 0.03071; HA-MYO7A-N: base vs middle= 0.3507, middle vs apex= 0.05761). Boxplots show medians, 25th, and 75th percentiles as box limits and minima and maxima as whiskers.

4.5. Hearing function deterioration and hair cell loss of adult *Myo7a-ΔN* mice.

MYO7A is important for the hair cell and hair bundle morphology. So, we evaluated the effect of deletion of *Myo7a-N* on hair cell maintenance at 40-week. Since MYO7A-N has the highest expression level at the basal turn of the cochlea, we focused on analyzing the hair cell morphology at the basal 180-degree turn of the cochlea (Fig. 4-7A). The very basal portion of the cochlea, also known as the 'hook' region, is indicated as region A in our analysis. The center of the basal turn is indicated as region B, and the transition of basal-middle region is indicated at region C. Our immunofluorescence images showed that the OHCs are nearly abolished at the region A, and the IHCs also showed severe morphological deterioration. The region B showed a less severe damage that this region had fewer OHC loss. The morphology of IHC in the region B is also comparable to WT. Finally, no hair cell loss is observed in region C. These results showed that the deletion of MYO7A-N could cause hair cell damage, which is consistent with previous result that loss of MYO7A leads to hair bundle degeneration and hair cell death. This phenotype is more severe in the OHCs at the beginning of the basal region, which is also consistent with the expression pattern of MYO7A-N.

Finally, we tested the hearing function of *Myo7a-ΔN* mice at 10-week and 40-week. Our analysis showed that *Myo7a-ΔN* has mild hearing loss at 10-week, and slowly deteriorates with age. At 40-weeks, *Myo7a-ΔN* mice showed ABR threshold around 50~70dB (Fig. 4-7B), significantly higher than age-matched WT controls. More importantly, *Myo7a-ΔN* mice showed significant reduction in DPOAE response at 10-week and 40-week as compare to WT controls, and the DPOAE is close to noise level at 40-week, suggesting that the OHC function is severely damaged at this age.

We conclude that the deletion of MYO7A-N causes an overall mild hearing loss, resulting

from a deterioration of OHC function as evident in the reduction of DPOAE response. This is consistent with the expression pattern of MYO7A-N in OHCs.

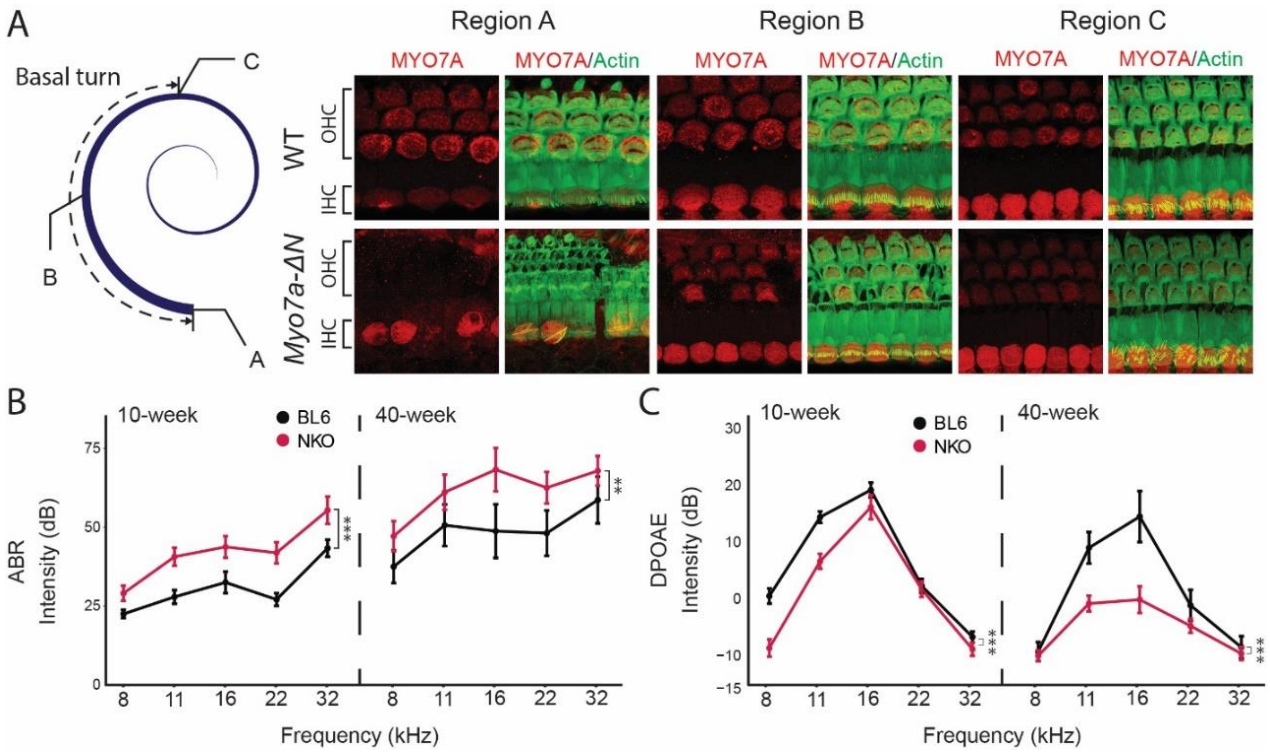

Figure 4-7: OHC loss and hearing function deterioration of *Myo7a-ΔN* mice.

A. Immunofluorescent images of the basal turn of cochlea of 40-week WT and *Myo7a-ΔN* mice. The beginning of the basal turn (Region A) of the *Myo7a-ΔN* mice shows abolished OHCs, which is shown by F-actin 'scars', a known marker for dead hair cells. The morphology of the IHC is also deteriorated. The middle part of the basal turn (Region B) also showed OHC loss. However, the OHCs and IHCs at the end of the basal turn (Region C) did not show a substantial difference between WT cochlea. **B**. ABR test of WT and *Myo7a-ΔN* mice at 10, and 40 weeks. Compared to WT mice, *Myo7a-ΔN* mice showed mild ABR threshold shifts at 10, and 40 weeks. (Number of animals: WT: 10-week: 12; 40-week: 8; *Myo7a-ΔN*: 10-week: 15, 40-week: 14. ANOVA p-value: 10-week: 6.64e-08; 40-week: 0.0028.) **C**. DPOAE of WT and *Myo7a-ΔN* mice at 10 and 40 weeks. Our results showed that the OHC function of *Myo7a-ΔN* deteriorated with age, which has the most significant DPOAE reduction at 40 weeks. (Number of animals: WT: 10-week: 9; 40-week: 8; *Myo7a-ΔN*: 10-week: 14, 40-week: 16. ANOVA p-value: 10-week: 3.80e-05; 40-week: 3.24e-05.)

5. Chapter 5: Identification of new regulatory mechanisms of *Myo7a*.

5.1. Revisiting published regulatory mechanisms of MYO7A

We discovered that multiple isoforms of *Myo7a* are differentially expressed in the cochlear hair cells. The major isoforms of *Myo7a*, *Myo7a-C* and *Myo7a-N* are generated by distinct transcriptional start sites, suggesting that the expression levels of these two isoforms are regulated by different regulatory elements (i.e., promoters, enhancers and transcription factors). However, the mechanisms that regulate *Myo7a* gene expression still need to be sufficiently understood. Historically, the first promoter region of *Myo7a* was identified by Batiste et al., which spans from 118bp upstream of the first exon of the *Myo7a-C*[125]. In their study, this promoter region drives the expression of the reporter gene eGFP predominantly in IHCs. In OHCs, eGFP expression has a higher level in the apex and decreased towards the base. This expression pattern is similar with the pattern of *Myo7a-C*.

We re-visited the activity of this *Myo7a* promoter in a transgenic mouse line in which this specific promoter sequence drives the expression of actin-GFP (Fig. 5-1A). In contrast to the general assumption, but consistent with the hypothesized expression pattern of MYO7A-C, *Myo7a* promoter-driven actin-GFP fluorescence was restricted to IHCs and apical OHCs (Fig. 5-1B). Occasional actin-GFP fluorescence was observed in OHCs of the middle turns as well. Therefore, we conclude that the expression driven by the widely used *Myo7a* promoter replicates the expression pattern of the canonical MYO7A-C isoform only. Line-plots show means of the ABR or DPOAE response. Standard error is presented as error bars.

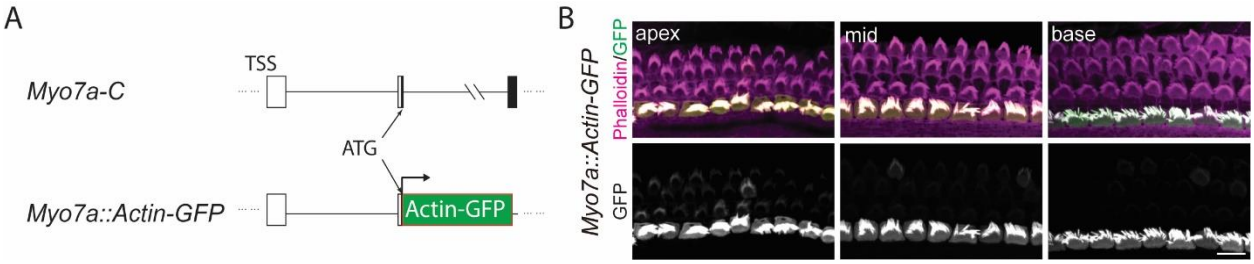

Figure 5-1. MYO7A-C is expressed primarily in IHCs and in a tonotopic gradient in OHCs, with decreasing expression towards the cochlear base.

A. The genomic position from which the *Myo7a* promoter used in the *Myo7a::Actin-GFP* transgenic mouse is derived. **B.** Actin-GFP signal and phalloidin reactivity in the organ of Corti of *Myo7a*::Actin-GFP transgenic mice at P6. The Actin-GFP signal was predominantly observed in the IHCs. Actin-GFP signal was detected at low levels in the apical OHCs and decreased tonotopically towards the basal end of the cochlea (scale bar: 10 μm).

5.2. The identification of new MYO7A gene regulatory units.

Previously, multiple enhancers and promoters of *Myo7a* have been identified, however, as elaborated in the previous paragraph, none of these elements could drive gene expression in all hair cells[125–128]. We hypothesized that additional regulatory elements regulate the tonotopic and possibly hair cell specific expression of *Myo7a*. On the search for such elements, we identified a new potent enhancer of *Myo7a*, a ~400bp region in the third intron of the gene. By mining ATAC-seq data from Neil Segil's Lab, we found an open chromatin region in the common intron of *Myo7a* (Fig5-2A). This ATAC-peak region had the highest peak in the *Myo7a* gene region, suggesting a potential role in regulating *Myo7a* expression. To test the function of this potential enhancer region, we named this ATAC-peak *EnhancerA* and created a mouse strain that has a ~300bp deletion of this region (*ΔEnhancerA* mice).

We then performed qPCR at P0 of *ΔEnhancerA* cochlear cDNA to evaluate the role of *EnhancerA* on different *Myo7a* isoforms (Fig5-2B). Our analysis showed that all *Myo7a* isoforms were reduced in *ΔEnhancerA* mice compared to control, suggesting that *EnhancerA* is essential for the expression of all *Myo7a* isoforms.

Next, we sought to test if *ΔEnhancerA* preferentially regulates *Myo7a* expression in a specific hair cell type or in a tonotopic pattern. Our immunofluorescent imaging showed that total MYO7A levels are reduced in both IHCs and OHCs of *ΔEnhancerA* mice tonotopically in the early postnatal stage. At P7, MYO7A was nearly absent from IHCs and OHCs in the basal region and had a 50% reduction in hair cells of the apical region. At P20, both IHCs and OHCs of *ΔEnhancerA* showed substantially reduced MYO7A in all regions. These data suggest that *EnhancerA* is crucial for Myo7a expression in a tonotopically and age-dependent manner.

Next, to evaluate the effect of the loss of *EnhancerA* on hearing function, we performed ABR and DPOAE tests on *ΔEnhancerA* mice. At three weeks, these mice showed early onset mild hearing loss shown by both ABR and DPOAE tests (Fig. 5-2G-H). However, their hearing condition rapidly deteriorated. At 8 weeks, *ΔEnhancerA* mice showed profound hearing loss with no ABR and DPOAE response, suggesting that functions of both IHCs and OHCs are impaired (Fig. 5-2G-H). Overall, we conclude that *EnhancerA* is necessary for regulating all isoforms of *Myo7a* in both IHCs and OHCs. It regulates *Myo7a* expression in a tonotopic manner at early postnatal stages, and the dependence on this enhancer increases in mature hair cells at all regions.

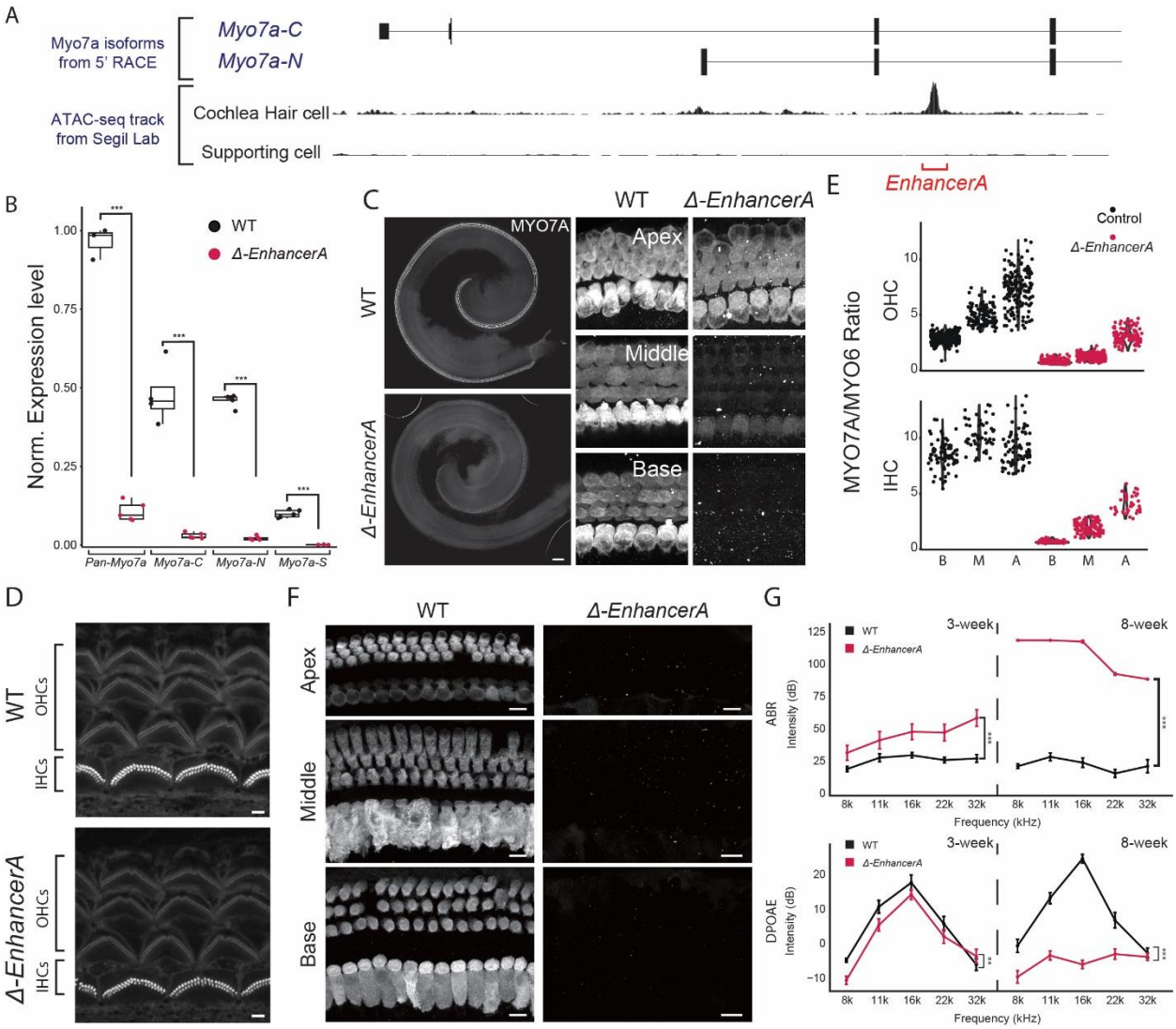

Figure 5-2: *EnhancerA* is necessary for *Myo7a* expression.

A. The diagram showing the transcriptional start sites of *Myo7a* isoforms. ATAC-seq tracks are from a publicly available dataset from Neil Segil Lab. *EnhancerA* is an around 400bp open chromatin region that locates in the third intron of *Myo7a-C*, which is indicated with red bracket. This region is specifically knocked out in *ΔEnhancerA* mice without affecting *Myo7a* exons. **B**. Normalized expression level of *Myo7a* isoforms measured by qPCR on P0 cochlear cDNA. *Myo7a* expression level is normalized to *Gapdh*. (WT vs. *ΔEnhancerA* mice T-test p-values of different isoforms: *pan-Myo7a*: 0.00013, *Myo7a-C*=0.002572, *Myo7a-N*=1.319e-07, *Myo7a-N*=5.588e-05. Number of Cochlea: WT=8, *ΔEnhancerA*=8. Pipetting repetition=5 per group.) Boxplots show medians, 25th, and 75th percentiles as box limits and minima and maxima as whiskers. **C**.

Immunofluorescent imaging of whole mount *ΔEnhancerA* cochlea at P5. A pan-MYO7A antibody is applied for immunostaining. Compared to WT cochlea, *ΔEnhancerA* mice showed tonotopic reduction of MYO7A immunoreactivity, with a stronger reduction in the basal region and less reduction at the apical region. (Scale bar: 10μm) **D**. Phalloidin staining of WT and *ΔEnhancerA* mice at P5. Images were taken at the beginning of the basal turn, which have strongest reduction of MYO7A immunoreactivity. *ΔEnhancerA* IHCs and OHCs do not show substantial difference in hair bundle morphology compared to WT. (Scale bar: 2μm) **E**. Quantification MYO7A immunoreactivity of cochlear hair cells at P5. MYO7A signals were normalized to MYO6. **F**. Immunofluorescent imaging of whole mount *ΔEnhancerA* cochlea at P20. In contrast with *ΔEnhancerA* P5 cochlea, which shows tonotopic MYO7A reduction, *ΔEnhancerA* cochlea showed nearly abolished MYO7A immunoreactivity at P20 at all regions. (Scale bar: 10μm) **G**. ABR test of WT and *ΔEnhancerA* at 3 weeks and 8 weeks old. *ΔEnhancerA* mice showed mild hearing loss, which deteriorated rapidly into profound hearing loss at 8 weeks (ANOVA p-value: 3-week=1.25e-08, 8-week<2e-16. Number of animals: WT: 3-week=8, 8-week=9; *ΔEnhancerA*: 3-week=8, 8-week=5). Lower panel shows that DPOAE test of WT and *ΔEnhancerA* at 3 weeks and 8 weeks old. Similar to ABR test, the *ΔEnhancerA* mice also show a rapidly progressive reduction in DPOAE, which is nearly abolished at 8 weeks. (ANOVA p-value: 3-week=0.0060, 8-week=1.12e-11. Number of animals: WT: 3-week=8, 8-week=10; *ΔEnhancerA*: 3-week=7, 8-week=5). Line-plots show means of the ABR or DPOAE response. Standard error is presented as error bars.

5.3. SIX2 – a transcription factor potentially regulates *Myo7a* expression

We have characterized the critical function of *EnhancerA* in regulating *Myo7a* gene expression. however, our immunohistochemistry imaging and qPCR assay indicate that the deletion of *EnhancerA* affects the expression of both *Myo7a-C* and *Myo7a-N* isoforms. Thus, we hypothesize that there might be another level of regulatory mechanism for the differential expression of *Myo7a* isoforms, potentially through the specific action of transcription factors that interact with *EnhancerA*. These transcription factors likely have a differential expression pattern in IHCs and OHCs, which then regulate the differential expression of *Myo7a* isoforms.

To identify the transcription factor that potentially interacts with *EnhancerA*, we searched Unbind2021 and Remap2022 tracks on the UCSC genome browser. We found a robust binding site for transcription factor SIX Homeobox 2 (SIX2) at the center of the ATAC-seq peak of the *EnhancerA*. The interaction between *EnhancerA* and SIX2 was also validated in ChIP-seq assays[129]. SIX2 is a member of SIX family of homeobox transcription factors. It is shown to have an essential function in the development of the kidney, craniofacial bones, and other organs[130–134], and the deletion of SIX2 in the mouse model causes early postnatal lethality. SIX1 is the paralogue of SIX2, which has been shown to have an essential function in the development of the auditory system[130,135,136]. Consequently, we hypothesized that SIX2 is important for the auditory system, and regulate the expression of *Myo7a* by interacting with *EnhancerA*.

First, we investigated the expression of SIX2 in the mouse cochlea. Previously, a group has reported that a widely used commercially available SIX2 antibody also interacts with SIX1[129]. To characterize the SIX2 expression level more specifically, our immunohistochemistry imaging was conducted on *Six2::Cre-egfp* mouse cochlea at P0, using the eGFP fluorescent signal as the reporter[137]. Our results showed that SIX2 is

highly expressed in a subgroup of supporting cells in the inner sulcus region (Fig. 5-3A-B). It is also highly expressed in OHCs and a minimal level in the IHCs (Fig. 5-3B). More importantly, the eGFP signal also shows a tonotopic gradient in the cochlea, which is strongest at the base and decreases toward the apex. This expression pattern correlates well with the *Myo7a-N* pattern in the cochlea, suggesting its potential role in regulating the expression of *Myo7a-N* in the cochlea. (Fig. 5-3B)

SIX2 is also strongly expressed in the vestibular system. And there is more eGFP positive hair cells and supporting cells in the striola region comparing to extra striola region (Fig. 5-2C). The function of these eGFP positive cells remains to be characterized in the future study.

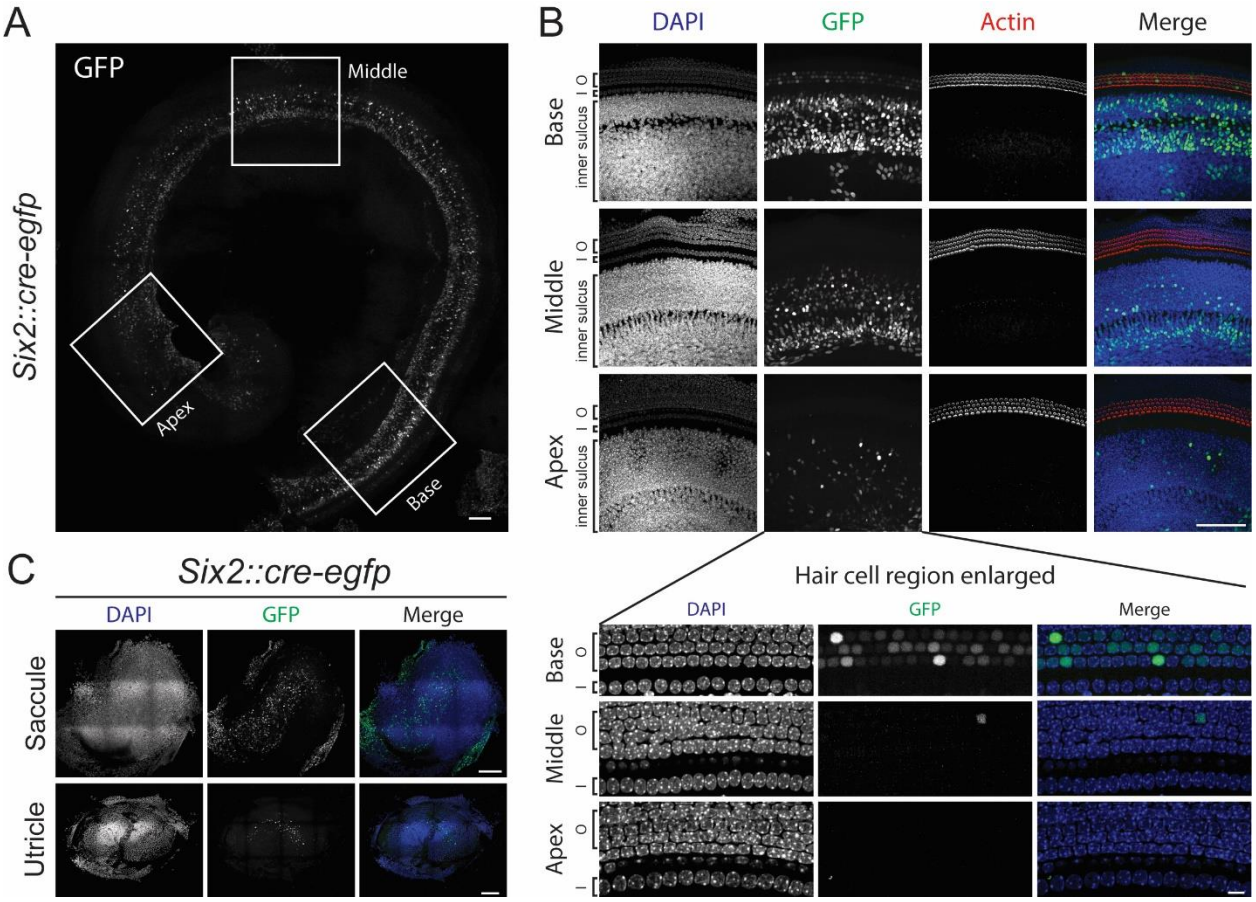

Figure 5-3: Expression pattern of SIX2 in the auditory system.

A, **B.** Whole-mount *Six2::Cre-egfp* mouse cochlea at P0. (A. Scale bar: 100μm. B. Scale bar: upper panel: 100μm, lower panel: 10μm). The box enlarged images are shown in panel B. eGFP positive cells are detected in the inner succus region and outer hair cells. *Six2* is also tonotopically expressed in OHCs, with a stronger signal at basal region and decrease towards the apex. Compared to OHCs, IHCs have nearly non-detectable signal of the eGFP. **C**. Immunofluorescent imaging of utricle and saccule at P0 (Scale bar: 10μm). Higher number of eGFP positive hair cells and supporting cells are detected in the striola region of both utricle and saccule.

5.4. SIX2 is important for hair cell maintenance.

Based on the expression pattern of SIX2 in the cochlea, especially in hair cells, we hypothesized that SIX2 has an important role in hair cells. We therefore tested the hair cell morphology in SIX2 deficient mice. Since the global deletion of SIX2 leads to early postnatal lethality, so we crossed *Atoh1-cre* mice and *Six2*$^{flox/flox}$ mice, deleting SIX2 in hair cells specifically. In these SIX2 conditional KO mice, we observed severe OHC loss at P0 (Fig. 5-4A). Although we did not observe inner hair cell loss, their hair bundles were also severely degenerated (Fig. 5-4B). More importantly, there was also a tonotopic gradient of OHC loss: OHCs were nearly abolished at the basal region, and and less cell loss toward the apex. This tonotopic hair cell loss is consistent with Six2 expression level in hair cells (Fig. 5-3B).

We also hypothesized that SIX2 promotes *Myo7a-N* expression by interacting with *EnhancerA*. Thus, we quantified the pan-MYO7A immunoreactivity of IHCs and OHCs at different regions at P0 (Fig. 5-4C). OHCs of *Atoh1-cre/Six2*$^{flox/flox}$ cochleae showed a tonotopic reduction of MYO7A signal. This reduction is most severe at the basal region and less severe at apical region. In contrast, consistent with the low expression level of SIX2 in IHCs, the MYO7A signal did not significantly reduced in IHCs of the *Atoh1-cre/Six2*$^{flox/flox}$ cochleae. This pattern of MYO7A reduction correlated with the expression pattern of SIX2, suggesting a correlation between SIX2 function and MYO7A expression level. However, it is important to note that the reduction of MYO7A could result from the overall hair cell deterioration. The direct interaction between SIX2 and *EnhancerA* will be tested in the future study.

It is also important to distinguish whether the hair cell loss in *Atoh1-cre/Six2*$^{flox/flox}$ mice resulted from developmental deficit or deficits in hair cell maintenance. To address this question, we also checked the hair cell number at P7. Comparing to SIX2 conditional

cochlea at P0, the P7 cochlea showed more severe OHCs loss, which suggests that SIX2 is essential for hair cell maintenance.

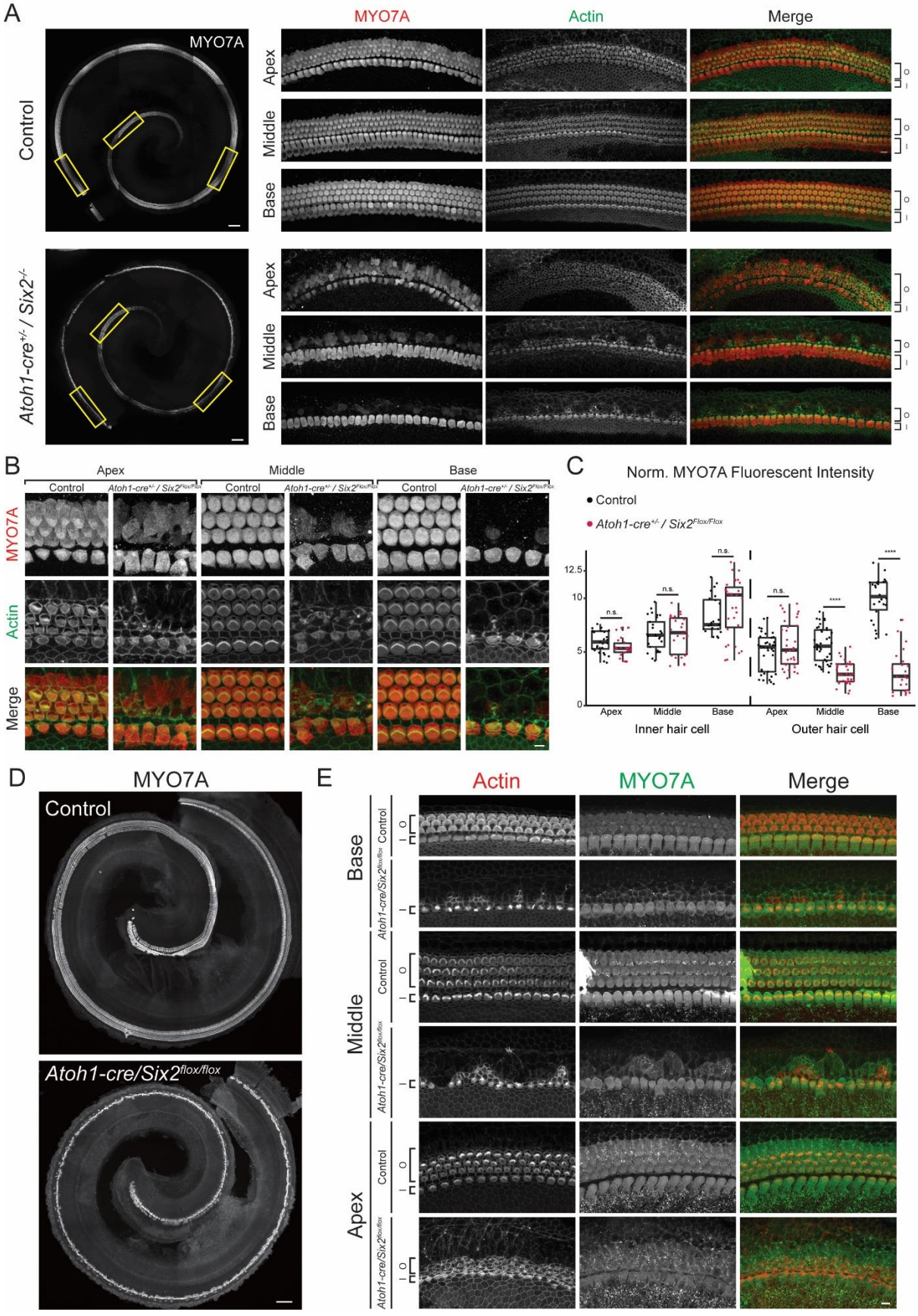
A
MYO7A
Actin
Merge
Control
Atoh1-cre+/- / Six2-/-
Apex
Middle
Base
B
Apex
Middle
Base
Control
Atoh1-cre+/- / Six2Flox/Flox
MYO7A
Actin
Merge
C
Norm. MYO7A Fluorescent Intensity
Control
Atoh1-cre+/- / Six2Flox/Flox
n.s.
****
Inner hair cell
Outer hair cell
D
MYO7A
Control
Atoh1-cre/Six2flox/flox
E
Actin
MYO7A
Merge
Base
Middle
Apex
Control
Atoh1-cre/Six2flox/flox

Figure 5-4: hair cell specific deletion of SIX2 leads to severe hair cell damages.

A. Whole-mount Immunofluorescent images of WT and *Atoh1-cre/Six2*$^{flox/flox}$ mouse cochlea at P0 (Scale bar: 100μm). Box enlarged images are shown on the right. This hair cell specific deletion of SIX2 caused a tonotopic OHC loss, which is more severe in the basal region. F-actin staining also indicates that hair bundles of *Atoh1-cre/Six2*$^{flox/flox}$ IHCs were severely damaged. **B**. Immunohistochemistry images of WT and *Atoh1-cre/Six2*$^{flox/flox}$ at apical, middle and basal turn of the cochlea at P0. MYO7A immunoreactivity decreased tonotopically in OHCs, with a higher amount of reduction in basal OHCs. (Scale bar: 10 μm) **C**. Quantification of MYO7A immunoreactivity at different regions of cochlea. The MYO7A signal is normalized to MYO6. Boxplots show medians, 25th, and 75th percentiles as box limits and minima and maxima as whiskers. **D, E**. Wholemount Immunofluorescent images of WT and *Atoh1-cre/Six2*$^{flox/flox}$ mouse cochlea at P7 (D. Scale bar: 100μm. E. Scale bar: 10μm).

6. Chapter 6: Discussion and future directions

6.1. Identification of MYO7A isoforms in cochlear hair cells.

This is the first study to report that multiple isoforms of MYO7A are differentially expressed in IHCs and OHCs. Analyses of KO and KI mouse models revealed that the canonical isoform MYO7A-C is predominantly expressed in IHCs. It is also expressed in OHCs in a tonotopic manner, with a higher level at the apex and decreases toward the base of the cochlea. We also identified a novel isoform of *Myo7a*, named *Myo7a-N*, whose expression is inversely correlated to that of *Myo7a-C*. Analysis showed that *Myo7a-N* is predominantly expressed in OHCs, highest in the basal region and decreases towards the apex.

Genomic databases indicate the existence of an alternative, short isoform (MYO7A-S) which lacks the NTE region. qPCR analysis indicated that the MYO7A-S has a very low expression level in cochlear hair cells. In addition, analysis of a mouse line in which the expression of *Myo7a-S* is specifically prevented by deleting its specific 5'UTR region (or removing the starting ATG) (*Myo7a-ΔS*) revealed WT-like MYO7A levels and hair bundle morphology.

We generated an additional mouse line in which the two major isoforms *Myo7a-C* and *Myo7a-N* were deleted (*Myo7a-ΔCN*), leaving *Myo7a-S* expression untouched. Interestingly, at P0, hair cells and hair bundles in *Myo7a-ΔCN* mice showed a near WT-like appearance, suggesting that the remaining level of MYO7A, likely *Myo7a-S*, can support the early development of hair bundles. However, during the course of postnatal development, *Myo7a-ΔCN* hair cells and hair bundles deteriorate rapidly, displaying a disorganized morphology comparable to *Myo7a-full KO* by P20. This is reflected in

severe loss of hair cells and hearing function at P20, comparable to the *Myo7a-full* KO mice.

This result is consistent with our qPCR analysis that showed *Myo7a-S* levels are low at P0 and further decline during postnatal development. A possible explanation for this phenotype is that hair cells have a higher general chromatin accessibility at early developmental stages. Thus, *Myo7a-S* is expressed as a redundant isoform at a background level. During the maturation of hair cell, *Myo7a-C* and *Myo7a-N* establish themselves as the dominant isoforms in hair cells. Meanwhile, the promoter of *Myo7a-S* becomes further closed, leading to its nearly abolished level in the mature hair cells. Taken together, we concluded that *Myo7a-C* and *Myo7a-N* are the major isoforms in the cochlea.

6.2. *Myo7a* is essential for tensioning the MET complex.

In *Myo7a-ΔC* IHCs, the expression of MYO7A happens to be at a critical level, high enough to enable normal hair bundle development, but sufficiently low to expose a hypomorphic phenotype in hair cell MET. In these hair cells, MET currents displayed a significant reduction in resting P_o and a rightward shift of the activation curve. Analyses of current kinetics and hair bundle motion revealed that the onset of motion was unchanged, while the onset of current was delayed, suggestive of impaired coupling between bundle displacement and MET activation. Taken together, the MET current phenotype in *Myo7a-ΔC* IHCs is consistent with a model in which MYO7A operates as the motor that tensions the tip link. Hypofunction of MYO7A causes a slackening of the tip link, leading to a reduction of Po. Upon stimulus onset, the initial bundle motion is used to make up for the slack in the tip ink, causing a delayed onset of the MET current. In addition to the changes in MET current, analysis of the bundle motion suggested that mechanical properties of the hair bundle are altered in *Myo7a-ΔC* mice. The source for

this difference remains to be investigated, but reduced hair bundle tension due to loss of tip links and ankle links are potential candidate mechanisms.

In our study, reduced resting P_o serves to indicate a less active tip-link motor. It is important to discuss the validity and robustness of this connection. In the *Myo7a-ΔC* IHCs, MYO7A is not only reduced at the UTLD, but also at the stereocilia base. Although we did not detect significant changes in the level or localization of the ankle link component ADGRV1[106], it is possible that the stiffness of the stereocilia base, thus pivot stiffness, is affected in the *Myo7a-ΔC* IHCs. In fact, analysis of stereocilia motion in response to fluid jet stimuli suggest that the mechanical properties, and potentially stiffness of the hair bundle, are altered in *Myo7a-ΔC* mice. The crucial question is whether changes in such additional "springs" in the system might influence tip-link tension and resting P_o indirectly. A judgment on this depends on the interpretation of the existing hair cell MET model. According to a generally accepted assumption, the tip link is tensed by a motor protein that pulls with a certain force (e.g., the term F_m in[138–141]). This force is maintained (force-clamped) regardless of the stiffness of other springs in the system. Mechanistically, this might be achieved by the motor climbing up the actin ladder until its stall force is reached. Experimentally, this interpretation is supported by the phenotype of the Triobp KO mice, in which, even though the pivot stiffness is severely reduced, hair cell MET currents show no signs of reduced resting P_o (e.g., changes in the activation curve)[142]. Based on this reasoning, we suggest that resting Po, regardless of changes in overall hair bundle stiffness, serves as a reasonably robust proxy for tip-link motor activity. The hair bundle however is a complex mechanical system, and present assumptions about the tip-link motor might be simplistic. For example, the tip-link motor might not be able to adjust to severe reduction of the bundle stiffness if its upward mobility is limited, as was previously suggested[57]. Direct mechanical measurements of tip-link tension, using previously described

methods[12,51], will provide more conclusive data on whether the reduction in resting P_o in *Myo7a-ΔC* IHCs is indeed accompanied by reduced tip-link tension.

One outstanding question in the hair cell field concerns the molecular correlation of slow adaptation. Several studies have advanced a model in which myosin motors, slipping down the F-actin core, might provide the mechanism for slow adaptation, adjusting tip-link tension to ensure an optimal sensitivity range[143–147]. While not addressed in our present study, the *Myo7a-ΔC* mice provide a suitable model to address this question for IHCs. If MYO7A is involved in tension generation and slow adaptation, we would expect slow adaptation to be affected in *Myo7a-ΔC* IHCs.

Two myosins, MYO1C and MYO7A, have been proposed to function as the tip-link motor. Evidence for MYO1C only applies to vestibular hair cells so far and does not prove conclusively that MYO1C directly tensions the tip link[144,147]. Recent localization evidence places MYO7A at the correct position, the UTLD[57]. Providing functional evidence implicating MYO7A in controlling tip-link tension has been more challenging, however, because complete loss-of-function impairs stereocilia development [95]. Experiments using a *Myo7a* KO mouse model were misinterpreted due to the unexpected presence of an additional mechanically gated current[147–149]. Our present study is consistent with a more recent study that used a conditional knockout approach to study MYO7A's role in MET in intact hair cells[96]. In $Myo7a^{fl/fl}Myo15\text{-}Cre^{+/-}$ mice, the *Myo15* promoter drives Cre-mediated *Myo7a* gene deletion in hair cells starting around P4, allowing hair cells to develop normally. MYO7A levels presumably reached critically low levels after P14 in IHCs, at which point electrophysiological recordings revealed a reduction in resting P_o, consistent with our results. Due to slow protein turnover after conditional deletion, functional experiments on MYO7A-depleted hair cells were limited to mice aged P14 and older. In comparison, our *Myo7a-ΔC* mice enable experiments at any age and importantly, allow the investigation of the functional significance of MYO7A

isoforms. The interpretation of the *Myo7a-ΔC* mouse phenotype needs to consider the fact that this mouse line is not a mere MYO7A hypomorph, but null for a specific isoform. It is therefore possible that some aspects of the described phenotype are caused by a combination of a depletion of overall MYO7A levels and the loss of isoform-specific functions. In summary, the conditional and isoform-specific KO mouse models are complementary tools in studying MYO7A's role in hair cell function.

With respect to the effect of MYO7A depletion on hair bundle morphology, it is noteworthy that *Myo7a-ΔC* IHCs display normal hair bundle development. We can therefore conclude that, at least during development, the remaining levels of MYO7A can compensate for the loss of MYO7A-C. Mature *Myo7a-ΔC* mice, however, develop a highly specific set of hair bundle defects in IHCs. Interestingly, the characteristics of those defects differ in the two transducing stereocilia rows: In the third row, stereocilia degeneration is evident, possibly consistent with previous studies showing stereocilia regression after loss of MET[105,116]. In contrast, the second row presents with a more complex phenotype, a reduction in prolate stereocilia tips and slightly longer stereocilia. The former is consistent with a reduction in resting tension[116], while the latter phenotype, although somewhat paradoxical compared to the phenotype of the third row, is consistent with previous studies reporting that stereocilia in *Myo7a*^{4626SB} mice are longer[97,150].

Myo7a-ΔC mice develop a progressive form of hearing loss. Based on the mild MET current phenotype in P7 *Myo7a-ΔC* IHCs, it is not surprising that hearing thresholds are not severely affected in wean age animals. With increasing age, MYO7A hypofunction might lead to significant MET dysfunction and/or broad defects in cellular homeostasis, both of which might affect hair bundle morphology and hearing. One must be cautious however to interpret the adult hearing loss phenotype solely from the angle of hair cell MET. MYO7A is widely localized in the hair cell, suggesting involvement in a range of

yet unknown cellular processes. It is therefore possible that MYO7A hypofunction causes cellular dysfunction that are MET-independent, and that those deficits contribute to the progressive hearing loss.

6.3. Function of MYO7A-N isoform in the auditory system.

Myo7a-ΔN mice show mild hearing at 40 weeks, contrasting to *Myo7a-ΔC* mice, which developed profound hearing loss at 8 weeks. One reason for this mild phenotype is that *Myo7a-N* is predominantly expressed in OHCs, which is responsible for cochlea amplification. Additionally, it should be noted that the highest frequency tested in our ABR study is 32kHz, which corresponds to best frequencies of hair cells located in the middle region of the cochlea, where MYO7A levels are only reduced by 30~40 percent. We suspect that the hearing loss at higher frequencies will be more severely affected. Notably, *Myo7a-ΔN* mice show an earlier deterioration of DPOAE response starting around 10 weeks, consistent with the OHC specific expression of Myo7a-N. In brief, hearing function in *Myo7a-ΔN* mice is affected in a manner that is consistent with our hypothesis that *Myo7a-N* is important for OHC function.

The reduction of MYO7A was shown to cause hair bundle deterioration, which best correlates with the hearing loss in *Myo7a-ΔN* mice. However, we have not evaluated the hair bundle morphology at middle and apical region of the cochlea. Previous studies have shown that the reduction of MYO7A could lead to hair bundle morphological changes, such as stereocilia degeneration and less prolate tips. Thus, I expect that *Myo7a-ΔN* mice will also show deteriorated stereocilia in the middle region of the cochlea. In future, we will apply SEM to evaluate the hair bundle morphology at 40-week.

6.4. Functional difference between MYO7A-C and MYO7A-N isoforms

Possibly the most important question arising from our study is why multiple isoforms of MYO7A are expressed in cochlear hair cells. Assuming MYO7A is indeed the tip-link tensioning motor, we propose that the differential expression of MYO7A may contribute to the shaping of MET properties, by modulating tip-link tension and resting Po. Several conclusions from previous studies are consistent with our hypothesis: First, it is well established that IHCs and OHCs have distinct MET current properties. Of most relevance for our study, MET in OHCs operates with a resting P_o of ~50%, while the resting P_o in IHCs is ~10-20%[112–114]. The tectorial membrane is unlikely to play a crucial role in this process, since the differences persist in recordings in which the tectorial membrane is removed. Differing expression levels of intracellular calcium buffers[113,151] and MET channel components[10] were proposed as potential mechanisms underlying these differences, but direct evidence was not provided. Second, a recent study in rats reported that tension in individual tip links is generally lower in IHCs compared to OHCs. Furthermore, tip-link tension in OHCs was found to increase sharply along the tonotopic axis[12].

We hypothesize that NTEs of MYO7A isoforms modify their motor functions, and that this feature enables differential fine-tuning of tip-link tension. The kinetics of MYO7A motors from various organisms have been studied, demonstrating that MYO7A is a slow-processive motor with a high duty ratio[152–155]. These are characteristics consistent with a role of MYO7A in mediating tonic tensioning of the tip-link complex. Moreover, N-terminus extensions are shown to modify the motor kinetics of myosins: The isoforms of MYO1C, also distinguished by short N-terminal extensions, were shown to exhibit differences in motor activity[118]. A similar N-terminal extension also affects mechanical tuning in MYO1B[119,156]. Taken together, it is tempting to hypothesize a model in which

the differential expression of the two MYO7A isoforms, each endowed with distinct motor properties, contributes to the differences in tip-link tension and resting P_o in IHCs and OHCs, and along the tonotopic axis in OHCs.

So far, our results do not provide direct evidence that MYO7A-C and MYO7A-N differs in motor activities. As a future plan, we will test the motor function of MYO7A-C and MYO7A-N in vitro by using purified protein. If the NTEs of these two isoforms indeed affect motor properties, we expect to observe modifications of their activities such as the ATPase activity, duty ratio, binding ability to actin etc. Furthermore, we will also test if the motor function differences between MYO7A-C and MYO7A-N contribute to the tip-link tension variability in mouse models. Our current isoform-specific deletion mouse lines (*Myo7a-ΔC* and *Myo7a-ΔN*) have reduced MYO7A level in hair cells, which makes it difficult to predict whether these two isoforms contribute to different tip-link tensions. To address this question, we generated two mouse lines in which the NTE of the MYO7A-C is replaced with MYO7A-N NTE coding sequence and vice versa (*Myo7a-CtoN* mice and *Myo7a-NtoC*) mice. Theoretically, these two mouse lines will express only *Myo7a-C* or *Myo7a-N* isoform at expression levels comparable to WT. The MET function will be tested with electrophysiology assays. According to our hypothesis, if the MYO7A-N isoform has a higher motor activity, we would observe an elevation of tip-link tension in the *Myo7a-CtoN* mice. Contrastingly, *MYO7A-NtoC* mice will have an overall reduced tip-link tension in hair cells. In brief, our future studies will provide a potential answer to the underling mechanism of tip-link tensions variability in different population of hair cells.

6.5. Expression regulation of *Myo7a* isoforms

6.5.1. Regulatory mechanism of MYO7A-C isoform

Our result indicates that MYO7A-C is predominantly expressed in IHCs, and in OHCs with a tonotopic gradient. This expression pattern mirrors the activity of a previously characterized *Myo7a* promoter, which was derived from a genomic region upstream of the translational start site of the canonical isoform[97,98]. In the initial study[125], this *Myo7a* promoter drove strong expression in IHCs, but weak expression in OHCs. This phenomenon has remained unexplained until now. Variants of this canonical *Myo7a* promoter have been widely used to drive transgene expression in hair cells, in both transgenic mice and viral constructs. Virally transduced OHCs exhibited inconsistent transgene expression and functional rescue[127,157]. Our findings of multiple isoforms and their promotors now explain these past inconsistencies.

Transcription factors that are important for initiating *Myo7a-C* transcription are understudied. Previously, a transcription factor, Yin Yang 1 (YY1)[128], was shown to repress the transcription of *Myo7a*, likely *Myo7a-C*, in hair cells. However, So far, with the currently available epigenomic databases, I could not confidently predict the transcription factor responsible for the expression of MYO7A-C in the auditory system, especially IHCs. Thus, the identification of the transcription factor for *Myo7a-C* transcription might provide a tool for driving gene expression in the IHCs.

6.5.2. Regulatory mechanism of MYO7A-N isoform

The newly discovered isoform *Myo7a-N* is expressed in OHCs in a tonotopic pattern, higher at the basal region and decreasing towards the apex. Previously, Ernest et.al reported a regulatory region in Zebrafish that drove expression of a GFP reporter gene in hair cells[126]. In their study, this regulatory region was described as “Block1” and “Block2”, which are two ~120 DNA sequences that are highly conserved across multiple

species. These two blocks are separated by a ~30bp spacer, and both blocks can drive the expression of the reporter gene. After identifying *Myo7a-N*, we found that Block2 corresponds to the first exon of *Myo7a-N* in the mouse genome, so we predict that Block1 is the promoter of the *Myo7a-N*. Interestingly, this predicted promoter region also harbors a binding site of SIX2, and their interaction has been validated in a ChIP-seq experiment[129]. Thus, I hypothesize that SIX2 binds to both *EnhancerA* and this promoter region to initiate the transcription of *Myo7a-N*. So far, we have not identified a cis- or trans-regulatory unit that specifically promotes the expression of *Myo7a-N*. However, a detailed characterization of the *Myo7a-N* regulatory mechanism is helpful for elucidating the formation of the *Myo7a-N* tonotopic gradient in OHCs, which might be a key factor for hair cells to maintain the tip-link tension among different populations of hair cells. In the future, we will test the chromatin interaction between *EnhancerA* and this predicted promoter of *Myo7a-N*. We will also test if SIX2 is necessary for the expression of *Myo7a-N*.

6.5.3. *EnhancerA*, a newly discovered enhancer of *Myo7a*.

In this study, we reported that *EnhancerA*, a cis-regulatory domain located at the intron region of *Myo7a*, is necessary for the expression of *Myo7a*. At early postnatal stages, the deletion of *EnhancerA* leads to a tonotopic reduction of *Myo7a*. This reduction progresses rapidly during the maturation of the cochlea, resulting in a near complete reduction of *Myo7a* immunoreactivity in all regions in mature mice. This suggests that *EnhancerA* is necessary for *Myo7a* expression, especially in adult mice.

So far, we have demonstrated the function of *EnhancerA* in cochlear hair cells; however, its function in vestibular hair cells remains to be explored. In the future, we will quantify the reduction of *Myo7a* in vestibular hair cells at different ages and characterize the change in the hair bundle morphology. Moreover, we will apply multiple tests for

evaluating vestibular system functions, including vestibular-ocular reflex, swimming test, and machine-learning-assisted animal behavior analysis.

Moreover, the deletion of *EnhancerA* caused MYO7A reduction in both IHCs and OHCs, suggesting that expressions of both isoforms are affected. Although evidence so far suggests that *EnhancerA* is necessary for the expression of both isoforms, *EnhancerA* might recruit different transcription factors in IHCs and OHCs, ultimately giving rise to the differential expression of MYO7A isoforms. By consulting publicly available ChIP-seq date, we predicted that SIX2 is one of the transcription factor candidates that regulates the expression of *Myo7a-N* in OHCs. Interestingly, we also found a SIX2 binding site in the promoter of the *Myo7a-N* isoform, suggesting that SIX2 promotes the transcription by binding to both promoter and the enhancer of *Myo7a-N*. More importantly, SIX2 is expressed predominantly in OHCs and has a tonotopic expression correlates with the *Myo7a-N*. Overall, SIX2 is a transcription factor candidate with the potential to regulate the expression of the *Myo7a-N*. However, which transcription factor might regulate the expression of *Myo7a-C* by interacting with *EnhancerA* is entirely unknown.

Taken together, the mechanism regulating *Myo7a* expression still remains to be explored, but the identification of such regulatory elements could be beneficial for expressing genes of interest in inner or outer hair cells specifically, or in a tonotopic manner.

6.5.4. The function of SIX2 in *Myo7a* expression and hair cell maintenance.

SIX2 is one of the transcription factor candidates that potentially regulates the differential expression of *Myo7a* isoforms. It is expressed in multiple types of cells in the cochlea, including OHCs and a subgroup of supporting cells in the inner sulcus region. More importantly, it is expressed in OHCs with a tonotopic gradient, which is highly

expressed in the basal hair cells and decreases towards the apex of the cochlea. This expression pattern correlates with the expression pattern of *Myo7a-N* isoforms. And as mentioned in the previous section, ChIP-seq databases have shown that they can interact with *EnhancerA* and the predicted promoter of *Myo7a-N*. Taken together, this evidence suggests that SIX2 might preferentially promote the expression of *Myo7a-N* in cochlea hair cells.

Hair cell specific deletion of SIX2 reduced MYO7A in OHCs more severely than in IHCs, consistent with a role of SIX2 in promoting *Myo7a-N* expression. However, we do not have direct evidence that the deletion of SIX2 preferably affects *Myo7a-N*, because the reduction of MYO7A could result from a general deterioration of hair cells. In the future, I would like to test if SIX2 can interact with *EnhancerA* or the putative *Myo7a-N* promoter region, by performing SIX2 ChIP-qPCR. I would also like to use an inducible CRE system to delete SIX2, which allows us to check *Myo7a* expression level before hair cell deterioration.

Other than MYO7A, my analysis showed that SIX2 might interact with promoter and enhancer regions of many other deafness genes, such as MYO15, Harmonin, LHFPL5, and promoters of multiple OHCs-specific genes, including prestin, and oncomodulin. These genes are especially important for mature hair cell functions, including the MET process, stereocilia length regulation etc. Considering the increase in Six2 expression level during maturation, I hypothesize that SIX2 is crucial for the maturation of hair cell function and maintenance, especially for OHCs. Overall, our result indicates SIX2 has an essential role in the cochlea.

So far, we are still in the preliminary stage of investigating SIX2 function in the auditory system, and our results suggest that it is a potential key factor of hair cell maintenance. This research raised many questions for future studies. Since SIX2 is also expressed in multiple supporting cells, I would like to characterize its function in supporting cells.

Furthermore, the expression and the function of SIX2 in the vestibular hair cells will be another direction I would like to pursue. And lastly, since the potential downstream targets of SIX2 that we identified might he important for the function of hair cells, I would like to apply single-cell RNA-seq and ChIP-seq to characterize the downstream targets of SIX2, which will be helpful to elucidate its function in the auditory system.

Abbreviations:

5’ RACE	Rapid amplification of cDNA ends
ABR	Auditory Brainstem Response
ADGRV1	Adhesion G Protein-Coupled Receptor V1
ANOVA	Analysis of Variance
ATAC-seq	Assay for Transposase-Accessible Chromatin using sequencing
ATOH1	Atonal Homolog 1
BSA	Bovine Serum Albumin
BLAST	Basic local alignment search tool
BMP7	Bone Morphogenetic Protein 7
Ca^{2+}	Calcium ions
$CaCl_2$	Calcium chloride
CAS9	CRISPR-ASsociated protein 9
CDH23	Cadherin 23
ChIP-seq	Chromatin immunoprecipitation sequencing
CIB2	Calcium And Integrin Binding Family Member 2
CMV	CytoMegaloVirus
CO2	Carbon Dioxide
CRISPR	Clustered Regularly Interspaced Short Palindromic Repeats
C-terminus	Carboxy-terminus
dB	Decibel
DMEM	Dulbecco’s Modified Eagle Medium

DNA	Deoxyribonucleic Acid
DNaseI	Deoxyribonuclease I
DPOAE	Distortion product otoacoustic emissions
EGFP	Enhanced Green Fluorescent Protein
EDTA	Ethylenediaminetetraacetic acid
F-actin	Filamentous actin
Floxed	Flanked by loxP sites
FBS	Fetal Bovine Serum
HA	Hemagglutinin epitope tag
HBSS	Hank's Buffered Saline Solution
HEPES	4-(2-HydroxyEthyl)-1-PiperazineEthaneSulfonic acid
Hz/kHz	Hertz/KiloHertz
LED	Light-emitting diode
IHC	Inner Hair Cell
ISL	ISL LIM Homeobox 1
I-X plots	Current–displacement plot
L/ml/µl	Litre/mililitre/microlitre
LHFPL5	LHFPL Tetraspan Subfamily Member 5
loxP	locus of X-over P1 Cre recognition site
MET	MechanoElectrical Transduction
$MgCl_2$	Magnesium Chloride
MYO7A	Myosin-VIIa

MYO7A-C	Canonical isoform of MYO7A
MYO7A-N	Novel isoform of MYO7A
MYO7A-S	Short isoform of MYO7A
μm	Microns
M/mM/μM	Molar/millimolar/micromolar
mm	millimeter
N-terminus	amino-terminus
NaCl	Sodium Chloride
NA	Numerical aperture
NIDCD	National Institute for Deafness and Other Communication Disorders
NIH	National Institutes of Health
N.S.	Not significant
NTE	N-terminus extension
OHC	Outer Hair Cell
OTOTO	Osmium Thiocarbohydrazide Osmium Technique
PBS	Phosphate-Buffered Saline
PCHD15	Protocadherin 15
PCR	Polymerase Chain Reaction
PFA	ParaFormAldehyde
P_o	Open probability
qPCR	Quantitative PCR
RNA	Ribonucleic Acid

RNA-seq	RNA sequencing
SD	Standard deviation
SEM	Scanning Electron Microscopy
SEM	Standard Error of the Mean
sgRNA	single guide Ribonucleic Acid
SIX2	SIX Homeobox 2
TMC1/2	Transmembrane Channel Like 1/2
UTLD	upper tip link density
WT	Wild-Type
YY1	Yin-yang 1

References:

1. Schwander, M., Kachar, B. & Müller, U. The cell biology of hearing. *J. Cell Biol.* **190**, 9–20 (2010).

2. Howard, J. & Hudspeth, A. J. Compliance of the hair bundle associated with gating of mechanoelectrical transduction channels in the Bullfrog's saccular hair cell. *Neuron* **1**, 189–199 (1988).

3. Peng, A. W. & Ricci, A. J. Somatic motility and hair bundle mechanics, are both necessary for cochlear amplification? *Hear. Res.* **273**, 109–122 (2011).

4. Gummer, A. W. & Preyer, S. Cochlear amplification and its pathology: Emphasis on the role of the tectorial membrane. *Ear, Nose Throat J.* **76**, (1997).

5. Dallos, P. Cochlear amplification, outer hair cells and prestin. *Curr. Opin. Neurobiol.* **18**, 370–376 (2008).

6. Ashmore, J. Outer hair cells and electromotility. *Cold Spring Harb. Perspect. Med.* **9**, (2019).

7. Ge, J. *et al.* Molecular mechanism of prestin electromotive signal amplification. *Cell* **184**, 4669-4679.e13 (2021).

8. Bavi, N. *et al.* The conformational cycle of prestin underlies outer-hair cell electromotility. *Nature* **600**, 553–558 (2021).

9. Garfinkle, T. J. & Saunders, J. C. Morphology of inner hair cell stereocilia in C57BL/6J mice as studied by scanning electron microscopy. *Otolaryngol. Neck Surg.* **91**, 421–426 (1983).

10. Beurg, M. *et al.* Variable number of TMC1-dependent mechanotransducer channels underlie tonotopic conductance gradients in the cochlea. *Nat. Commun.* **9**, (2018).

11. Fettiplace, R. & Kim, K. X. The Physiology of Mechanoelectrical Transduction Channels in

Hearing. *Physiol. Rev.* **94**, 951–986 (2014).

12. Tobin, M., Chaiyasitdhi, A., Michel, V., Michalski, N. & Martin, P. Stiffness and tension gradients of the hair cell's tip-link complex in the mammalian cochlea. *Elife* **8**, 1–25 (2019).

13. Ruggero, M. A., Rich, N. C., Recio, A., Narayan, S. S. & Robles, L. Basilar-membrane responses to tones at the base of the chinchilla cochlea. *J. Acoust. Soc. Am.* **101**, 2151–2163 (1997).

14. Russell, I. J. & Nilsen, K. E. The location of the cochlear amplifier: Spatial representation of a single tone on the guinea pig basilar membrane. *Proc. Natl. Acad. Sci. U. S. A.* **94**, 2660–2664 (1997).

15. Rhode, W. S. & Recio, A. Study of mechanical motions in the basal region of the chinchilla cochlea. *J. Acoust. Soc. Am.* **107**, 3317–3332 (2000).

16. Ren, T. Longitudinal pattern of basilar membrane vibration in the sensitive cochlea. *Proc. Natl. Acad. Sci. U. S. A.* **99**, 17101–17106 (2002).

17. Kaltenbach, J. A., Falzarano, P. R. & Simpson, T. H. Postnatal development of the hamster cochlea. II. Growth and differentiation of stereocilia bundles. *J. Comp. Neurol.* **350**, 187–198 (1994).

18. Thiede, B. R. *et al.* Retinoic acid signalling regulates the development of tonotopically patterned hair cells in the chicken cochlea. *Nat. Commun.* **5**, (2014).

19. Mann, Z. F. *et al.* A gradient of Bmp7 specifies the tonotopic axis in the developing inner ear. *Nat. Commun.* **5**, (2014).

20. Son, E. J. *et al.* Conserved role of Sonic Hedgehog in tonotopic organization of the avian basilar papilla and mammalian cochlea. *Proc. Natl. Acad. Sci. U. S. A.* **112**, 3746–3751 (2015).

21. Bok, J., Zenczak, C., Hwang, C. H. & Wu, D. K. Auditory ganglion source of Sonic hedgehog regulates timing of cell cycle exit and differentiation of mammalian cochlear hair cells. *Proc. Natl. Acad. Sci. U. S. A.* **110**, 13869–13874 (2013).

22. Filova, I. *et al.* ISL1 is necessary for auditory neuron development and contributes toward tonotopic organization. *Proc. Natl. Acad. Sci.* **119**, (2022).

23. Pickles, J. O., Comis, S. D. & Osborne, M. P. Cross-links between stereocilia in the guinea pig organ of Corti, and their possible relation to sensory transduction. *Hear. Res.* **15**, 103–112 (1984).

24. Markin, V. S. & Hudspeth, A. J. Gating-spring models of mechanoelectrical transduction by hair cells of the internal ear. *Annu. Rev. Biophys. Biomol. Struct.* **24**, 59–83 (1995).

25. Hudspeth, A. J., Choe, Y., Mehta, A. D. & Martin, P. Putting ion channels to work: Mechanoelectrical transduction, adaptation, and amplification by hair cells. *Proc. Natl. Acad. Sci. U. S. A.* **97**, 11765–11772 (2000).

26. Howard, J., Roberts, W. M. & Hudspeth, A. J. Mechanoelectrical transduction by hair cells. *Annu. Rev. Biophys. Biophys. Chem.* **17**, 99–124 (1988).

27. Roberts, W. M., Howard, J. & Hudspeth, A. J. Hair cells: transduction, tuning, and transmission in the inner ear. *Annu. Rev. Cell Biol.* **4**, 63–92 (1988).

28. Duvall, A. J., Flock, A. & Wersäll, J. The ultrastructure of the sensory hairs and associated organelles of the cochlear inner hair cell, with reference to directional sensitivity. *J. Cell Biol.* **29**, 497–505 (1966).

29. Denk, W., Holt, J. R., Shepherd, G. M. G. & Coreytt, D. P. Calcium imaging of single stereocilia in hair cells: localization of transduction channels at both ends of tip links. *Neuron* **15**, 1311–1321 (1995).

30. Jaramillo, F. & Hudspeth, A. J. Localization of the hair cell's transduction channels at the hair bundle's top by iontophoretic application of a channel blocker. *Neuron* **7**, 409–420 (1991).

31. Beurg, M., Fettiplace, R., Nam, J.-H. & Ricci, A. J. Localization of inner hair cell mechanotransducer channels using high-speed calcium imaging. *Nat. Neurosci.* **12**, 553–558 (2009).

32. Pan, B. *et al.* TMC1 and TMC2 are components of the mechanotransduction channel in hair cells of the mammalian inner ear. *Neuron* **79**, 504–515 (2013).

33. Pan, B. *et al.* TMC1 Forms the Pore of Mechanosensory Transduction Channels in Vertebrate Inner Ear Hair Cells. *Neuron* **99**, 736-753.e6 (2018).

34. Zhao, B. *et al.* TMIE is an essential component of the mechanotransduction machinery of cochlear hair cells. *Neuron* **84**, 954–967 (2014).

35. Cunningham, C. L. *et al.* TMIE Defines Pore and Gating Properties of the Mechanotransduction Channel of Mammalian Cochlear Hair Cells. *Neuron* **107**, 126-143.e8 (2020).

36. Liang, X. *et al.* CIB2 and CIB3 are auxiliary subunits of the mechanotransduction channel of hair cells. *Neuron* **109**, 2131-2149.e15 (2021).

37. Giese, A. P. J. *et al.* CIB2 interacts with TMC1 and TMC2 and is essential for mechanotransduction in auditory hair cells. *Nat. Commun.* **8**, (2017).

38. Riazuddin, S. *et al.* Alterations of the CIB2 calcium-and integrin-binding protein cause Usher syndrome type 1J and nonsyndromic deafness DFNB48. *Nat. Genet.* **44**, 1265–1271 (2012).

39. Xiong, W. *et al.* TMHS is an integral component of the mechanotransduction machinery of

cochlear hair cells. *Cell* **151**, 1283–1295 (2012).

40. Beurg, M., Xiong, W., Zhao, B., Müller, U. & Fettiplace, R. Subunit determination of the conductance of hair-cell mechanotransducer channels. *Proc. Natl. Acad. Sci. U. S. A.* **112**, 1589–1594 (2015).

41. Yu, X. *et al.* Deafness mutation D572N of TMC1 destabilizes TMC1 expression by disrupting LHFPL5 binding. *Proc. Natl. Acad. Sci. U. S. A.* **117**, 29894–29903 (2020).

42. Choudhary, D. *et al.* Structural determinants of protocadherin-15 mechanics and function in hearing and balance perception. *Proc. Natl. Acad. Sci. U. S. A.* **117**, 4837–24848 (2020).

43. Shotwell, S. L., Jacobs, R. & Hudspeth, A. J. Directional Sensitivity of Individual Vertebrate Hair Cells To Controlled Deflection of Their Hair Bundles. *Ann. N. Y. Acad. Sci.* **374**, 1–10 (1981).

44. Goodyear, R. J. & Richardson, G. P. A novel antigen sensitive to calcium chelation that is associated with the tip links and kinocilial links of sensory hair bundles. *J. Neurosci.* **23**, 4878–4887 (2003).

45. Ahmed, Z. M. *et al.* The tip-link antigen, a protein associated with the transduction complex of sensory hair cells, is protocadherin-15. *J. Neurosci.* **26**, 7022–7034 (2006).

46. Alagramam, K. N. *et al.* The mouse Ames waltzer hearing-loss mutant is caused by mutation of Pcdh15, a novel protocadherin gene. *Nat. Genet.* **27**, 99–102 (2001).

47. Siemens, J. *et al.* Cadherin 23 Is a component of the tip link in hair-cell stereocilla. *Nature* **428**, 950–955 (2004).

48. Bolz, H. *et al.* Mutation of CDH23, encoding a new member of the cadherin gene family, causes Usher syndrome type 1D. **27**, (2001).

49. Kazmierczak, P. *et al.* Cadherin 23 and protocadherin 15 interact to form tip-link filaments in sensory hair cells. *Nature* **449**, 87–91 (2007).

50. Kachar, B., Parakkal, M., Kurc, M., Zhao, Y. D. & Gillespie, P. G. High-resolution structure of hair-cell tip links. *Proc. Natl. Acad. Sci. U. S. A.* **97**, 13336–13341 (2000).

51. Assad, J. A., Shepherd, G. M. G. & Corey, D. P. Tip-link integrity and mechanical transduction in vertebrate hair cells. *Neuron* **7**, 985–994 (1991).

52. Indzhykulian, A. A. *et al.* Molecular Remodeling of Tip Links Underlies Mechanosensory Regeneration in Auditory Hair Cells. **11**, (2013).

53. Gillespie, P. G. & Müller, U. Mechanotransduction by Hair Cells: Models, Molecules, and Mechanisms. *Cell* **139**, 33–44 (2009).

54. Maeda, R. *et al.* Tip-link protein protocadherin 15 interacts with transmembrane channel-like proteins TMC1 and TMC2. *Proc. Natl. Acad. Sci.* **111**, 12907–12912 (2014).

55. Grillet, N. *et al.* The mechanotransduction machinery of hair cells. *Sci. Signal.* **2**, 1–6 (2009).

56. Ricci, A. J., Kachar, B., Gale, J. & Van Netten, S. M. Mechano-electrical transduction: New insights into old ideas. *J. Membr. Biol.* **209**, 71–88 (2006).

57. Grati, M. & Kachar, B. Myosin VIIa and sans localization at stereocilia upper tip-link density implicates these Usher syndrome proteins in mechanotransduction. *Proc. Natl. Acad. Sci.* **108**, 11476–11481 (2011).

58. Yu, I.-M. *et al.* Myosin 7 and its adaptors link cadherins to actin. *Nat. Commun.* **8**, 15864 (2017).

59. Adato, A. *et al.* Interactions in the network of usher syndrome type 1 proteins. *Hum. Mol. Genet.* **14**, 347–356 (2005).

60. El-Amraoui, A. & Petit, C. Usher I syndrome: unravelling the mechanisms that underlie the cohesion of the growing hair bundle in inner ear sensory cells. *J. Cell Sci.* **118**, 4593–4603 (2005).

61. Sweeney, H. L. & Houdusse, A. Structural and Functional Insights into the Myosin Motor Mechanism. *Annu. Rev. Biophys.* **39**, 539–557 (2010).

62. Houdusse, A. & Sweeney, H. L. How Myosin Generates Force on Actin Filaments. *Trends Biochem. Sci.* **41**, 989–997 (2016).

63. Pollock, L. M., Chou, S. W. & McDermott, B. M. My oh my(osin): Insights into how auditory hair cells count, measure, and shape. *J. Cell Biol.* **212**, 135–137 (2016).

64. Friedman, T. B., Belyantseva, I. A. & Frolenkov, G. I. Myosins and Hearing. *Adv. Exp. Med. Biol.* **1239**, 317–330 (2020).

65. Block, S. M. Fifty ways to love your lever: Myosin motors. *Cell* **87**, 151–157 (1996).

66. Dominguez, R. & Holmes, K. C. Actin Structure and Function. *Annu. Rev. Biophys.* **40**, 169–186 (2011).

67. Hartman, M. A. & Spudich, J. A. The myosin superfamily at a glance. *J. Cell Sci.* **125**, 1627–1632 (2012).

68. Sellers, J. R. Myosins: A diverse superfamily. *Biochim. Biophys. Acta - Mol. Cell Res.* **1496**, 3–22 (2000).

69. Friedman, T. B., Sellers, J. R. & Avraham, K. B. Unconventional myosins and the genetics of hearing loss. *Am. J. Med. Genet. - Semin. Med. Genet.* **89**, 147–157 (1999).

70. Fang, Q. *et al.* The 133-kDa N-terminal domain enables myosin 15 to maintain mechanotransducing stereocilia and is essential for hearing. *Elife* **4**, 1–22 (2015).

71. Hadi, S., Alexander, A. J., Vélez-Ortega, A. C. & Frolenkov, G. I. Myosin-XVa Controls Both Staircase Architecture and Diameter Gradation of Stereocilia Rows in the Auditory Hair Cell Bundles. *J. Assoc. Res. Otolaryngol.* **21**, 121–135 (2020).

72. Belyantseva, I. A. *et al.* Myosin-XVa is required for tip localization of whirlin and differential elongation of hair-cell stereocilia. *Nat. Cell Biol.* **7**, 148–156 (2005).

73. Salles, F. T. *et al.* Myosin IIIa boosts elongation of stereocilia by transporting espin 1 to the plus ends of actin filaments. *Nat. Cell Biol.* **11**, 443–450 (2009).

74. Liu, H. *et al.* Myosin III-mediated cross-linking and stimulation of actin bundling activity of Espin. *Elife* **5**, (2016).

75. Ebrahim, S. *et al.* Stereocilia-staircase spacing is influenced by myosin III motors and their cargos espin-1 and espin-like. *Nat. Commun.* **7**, (2016).

76. Eatock, R. A., Corey, D. P. & Hudspeth, A. J. Adaptation of mechanoelectrical transduction in hair cells of the bullfrog's sacculus. *J. Neurosci.* **7**, 2821–2836 (1987).

77. Holt, J. R. *et al.* A chemical-genetic strategy implicates myosin-1c in adaptation by hair cells. *Cell* **108**, 371–381 (2002).

78. Hasson, T. *et al.* Unconventional myosins in inner-ear sensory epithelia. *J. Cell Biol.* **137**, 1287–1307 (1997).

79. Gillespie, P. G. & Cyr, J. L. Myosin-1c, the Hair Cell's Adaptation Motor. *Annu. Rev. Physiol.* **66**, 521–545 (2004).

80. Walker, R. G. & Hudspeth, A. J. Calmodulin controls adaptation of mechanoelectrical transduction by hair cells of the bullfrog's sacculus. *Proc. Natl. Acad. Sci. U. S. A.* **93**, 2203–2207 (1996).

81. García, J. A., Yee, A. G., Gillespie, P. G. & Corey, D. P. Localization of myosin-Iβ near both ends of tip links in frog saccular hair cells. *J. Neurosci.* **18**, 8637–8647 (1998).

82. Caprara, G. A., Mecca, A. A. & Peng, A. W. Decades-old model of slow adaptation in sensory hair cells is not supported in mammals. *Sci. Adv.* **6**, 1–13 (2020).

83. Melchionda, S. *et al.* MYO6, the human homologue of the gene responsible for deafness in Snell's waltzer mice, is mutated in autosomal dominant nonsyndromic hearing loss. *Am. J. Hum. Genet.* **69**, 635–640 (2001).

84. Ahmed, Z. M. *et al.* Mutations of MYO6 are associated with recessive deafness, DFNB37. *Am. J. Hum. Genet.* **72**, 1315–1322 (2003).

85. Avraham, K. B. *et al.* The mouse Snell's waltzer deafness gene encodes an unconventional myosin required for structural integrity of inner ear hair cells. *Nature* **11**, 369–375 (1995).

86. Mhatre, A. N., Li, J., Kim, Y., Coling, D. E. & Lalwani, A. K. Cloning and Developmental Expression of Nonmuscle Myosin IIA (Myh9) in the Mammalian Inner Ear. *J. Neurosci. Res.* **76**, 296–305 (2004).

87. Kunishima, S. & Saito, H. Advances in the understanding of MYH9 disorders. *Curr. Opin. Hematol.* **17**, 405–410 (2010).

88. Moreland, Z. G. & Bird, J. E. Myosin motors in sensory hair bundle assembly. *Curr. Opin. Cell Biol.* **79**, 102132 (2022).

89. Koenekoop, R. K., Arriaga, M. A., Trzupek, K. M. & Lentz, J. J. Usher Syndrome Type I. *GeneReviews* (2020).

90. Castiglione, A. & Möller, C. Usher Syndrome. *Audiol. Res.* **12**, 42–65 (2022).

91. Weil, D. *et al.* Usher syndrome type I G (USH1G) is caused by mutations in the gene

encoding SANS, a protein that associates with the USH1C protein, harmonin. *Hum. Mol. Genet.* **12**, 463–471 (2003).

92. Mustapha, M. *et al.* A novel locus for Usher syndrome type I, USH1G, maps to chromosome 17q24–25. *Hum. Genet. 2002 1104* **110**, 348–350 (2002).

93. Ouyang, X. M. *et al.* Mutations in the alternatively spliced exons of USH1C cause non-syndromic recessive deafness. *Hum. Genet. 2002 1111* **111**, 26–30 (2014).

94. Well, D. *et al.* Defective myosin VIIA gene responsible for Usher syndrome type IB. *Nat. 1995 3746517* **374**, 60–61 (1995).

95. Self, T. *et al.* Shaker-1 mutations reveal roles for myosin VIIA in both development and function of cochlear hair cells. *Development* **125**, 557–566 (1998).

96. Corns, L. F. *et al.* Mechanotransduction is required for establishing and maintaining mature inner hair cells and regulating efferent innervation. *Nat. Commun. 2018 91* **9**, 1–15 (2018).

97. Prosser, H. M., Rzadzinska, A. K., Steel, K. P. & Bradley, A. Mosaic Complementation Demonstrates a Regulatory Role for Myosin VIIa in Actin Dynamics of Stereocilia. *Mol. Cell. Biol.* **28**, 1702–1712 (2008).

98. Zhang, D. S. *et al.* Multi-isotope imaging mass spectrometry reveals slow protein turnover in hair-cell stereocilia. *Nature* **481**, 520–524 (2012).

99. Haeussler, M. *et al.* Evaluation of off-target and on-target scoring algorithms and integration into the guide RNA selection tool CRISPOR. *Genome Biol.* **17**, 1–12 (2016).

100. Grillet, N. *et al.* Harmonin Mutations Cause Mechanotransduction Defects in Cochlear Hair Cells. *Neuron* **62**, 375–387 (2009).

101. Zallocchi, M. *et al.* Role for a novel Usher protein complex in hair cell synaptic maturation.

PLoS One **7**, (2012).

102. Ramunno-Johnson, D., Strimbu, C. E., Fredrickson, L., Arisaka, K. & Bozovic, D. Distribution of frequencies of spontaneous oscillations in hair cells of the bullfrog sacculus. *Biophys. J.* **96**, 1159–1168 (2009).

103. Thiede, B. R. *et al.* Retinoic acid signalling regulates the development of tonotopically patterned hair cells in the chicken cochlea. *Nat. Commun.* **5**, (2014).

104. Lelli, A., Asai, Y., Forge, A., Holt, J. R. & Geleoc, G. S. G. Tonotopic Gradient in the Developmental Acquisition of Sensory Transduction in Outer Hair Cells of the Mouse Cochlea. *J. Neurophysiol.* **101**, 2961–2973 (2009).

105. Vélez-Ortega, A. C., Freeman, M. J., Indzhykulian, A. A., Grossheim, J. M. & Frolenkov, G. I. Mechanotransduction current is essential for stability of the transducing stereocilia in mammalian auditory hair cells. *Elife* **6**, 1–22 (2017).

106. Michalski, N. *et al.* Molecular characterization of the ankle-link complex in cochlear hair cells and its role in the hair bundle functioning. *J. Neurosci.* **27**, 6478–6488 (2007).

107. Morgan, C. P. *et al.* PDZD7-MYO7A complex identified in enriched stereocilia membranes. *Elife* **5**, 1–34 (2016).

108. Senften, M. *et al.* Physical and functional interaction between protocadherin 15 and myosin VIIa in mechanosensory hair cells. *J. Neurosci.* **26**, (2006).

109. Delprat, B. *et al.* Myosin XVa and whirlin, two deafness gene products required for hair bundle growth, are located at the stereocilia tips and interact directly. *Hum. Mol. Genet.* **14**, 401–410 (2005).

110. Hamann, J. *et al.* International union of basic and clinical pharmacology. XCIV. adhesion G protein-coupled receptors. *Pharmacol. Rev.* **67**, 338–367 (2015).

111. Boëda, B. *et al.* Myosin VIIa, harmonin and cadherin 23, three Usher I gene products that cooperate to shape the sensory hair cell bundle. *EMBO J.* **21**, 6689–6699 (2002).

112. Peng, A. W., Effertz, T. & Ricci, A. J. Adaptation of Mammalian Auditory Hair Cell Mechanotransduction Is Independent of Calcium Entry. *Neuron* **80**, 960–972 (2013).

113. Corns, L. F., Johnson, S. L., Kros, C. J. & Marcotti, W. Calcium entry into stereocilia drives adaptation of the mechanoelectrical transducer current of mammalian cochlear hair cells. *Proc. Natl. Acad. Sci.* **111**, 14918–14923 (2014).

114. Johnson, S. L., Beurg, M., Marcotti, W. & Fettiplace, R. Prestin-Driven Cochlear Amplification Is Not Limited by the Outer Hair Cell Membrane Time Constant. *Neuron* **70**, 1143–1154 (2011).

115. Caprara, G. A., Mecca, A. A., Wang, Y., Ricci, A. J. & Peng, A. W. Hair bundle stimulation mode modifies manifestations of mechanotransduction adaptation. *J. Neurosci.* **39**, 9098–9106 (2019).

116. Rzadzinska, A. K., Schneider, M. E., Davies, C., Riordan, G. P. & Kachar, B. An actin molecular treadmill and myosins maintain stereocilia functional architecture and self-renewal. *J. Cell Biol.* **164**, 887–897 (2004).

117. Giese, S. *et al.* Mechanochemical properties of human myosin-1C are modulated by isoform-specific differences in the N-terminal extension. *J. Biol. Chem.* **296**, 100128 (2021).

118. Zattelman, L. *et al.* N-terminal splicing extensions of the human MYO1C gene fine-tune the kinetics of the three full-length myosin IC isoforms. *J. Biol. Chem.* **292**, 17804–17818 (2017).

119. Greenberg, M. J., Lin, T., Shuman, H. & Ostap, E. M. Mechanochemical tuning of myosin-I by the N-terminal region. *Proc. Natl. Acad. Sci. U. S. A.* **112**, E3337–E3344 (2015).

120. Varadi, M. *et al.* AlphaFold Protein Structure Database: Massively expanding the structural coverage of protein-sequence space with high-accuracy models. *Nucleic Acids Res.* **50**, D439–D444 (2022).

121. Jumper, J. *et al.* Highly accurate protein structure prediction with AlphaFold. *Nature* **596**, 583–589 (2021).

122. Morris, A. L., MacArthur, M. W., Hutchinson, E. G. & Thornton, J. M. Stereochemical quality of protein structure coordinates. *Proteins Struct. Funct. Bioinforma.* **12**, 345–364 (1992).

123. Lopes, V. S. *et al.* The Usher 1B protein, MYO7A, is required for normal localization and function of the visual retinoid cycle enzyme, RPE65. *Hum. Mol. Genet.* **20**, 2560–2570 (2011).

124. Liu, X.-Z. *et al.* Autosomal dominant non-syndromic deafness caused by a mutation in the myosin VIIA gene. *Nat. Genet.* **17**, 268–269 (1997).

125. Boëda, B., Weil, D. & Petit, C. A specific promoter of the sensory cells of the inner ear defined by transgenesis. *Hum. Mol. Genet.* **10**, 1581–1589 (2001).

126. Ernest, S. & Rosa, F. M. A genomic region encompassing a newly identified exon provides enhancing activity sufficient for normal myo7aa expression in zebrafish sensory hair cells. *Dev. Neurobiol.* **75**, 961–983 (2015).

127. Park, S., Jang, S., Lee, J.-H., Kim, S.-H. & Ryoo, Z. Y. Attempted rescue of circling mice by hair cell-specific expression (Myo7a promoter) of tmie transgene. *Med. Weter.* **73**, 399–403 (2017).

128. Street, V. A., Li, J., Robbins, C. A. & Kallman, J. C. A DNA variant within the MYO7A promoter regulates YY1 transcription factor binding and gene expression serving as a potential dominant DFNA11 auditory genetic modifier. *J. Biol. Chem.* **286**, 15278–15286

(2011).

129. O'Brien, L. L. *et al. Transcriptional regulatory control of mammalian nephron progenitors revealed by multi-factor cistromic analysis and genetic studies*. *PLoS Genetics* vol. 14 (2018).

130. Wegert, J. *et al.* Mutations in the SIX1/2 Pathway and the DROSHA/DGCR8 miRNA Microprocessor Complex Underlie High-Risk Blastemal Type Wilms Tumors. *Cancer Cell* **27**, 298–311 (2015).

131. Walz, A. L. *et al.* Recurrent DGCR8, DROSHA, and SIX Homeodomain Mutations in Favorable Histology Wilms Tumors. *Cancer Cell* **27**, 286–297 (2015).

132. Weber, S. *et al.* SIX2 and BMP4 mutations associate with anomalous kidney development. *J. Am. Soc. Nephrol.* **19**, 891–903 (2008).

133. Li, J. *et al.* Chromatin remodelers interact with Eya1 and Six2 to target enhancers to control nephron progenitor cell maintenance. *J. Am. Soc. Nephrol.* **32**, 2815–2833 (2021).

134. Xu, J. *et al.* Eya1 interacts with Six2 and Myc to regulate expansion of the nephron progenitor pool during nephrogenesis. *Dev. Cell* **31**, 434–447 (2014).

135. Zhang, T., Xu, J., Maire, P. & Xu, P. X. Six1 is essential for differentiation and patterning of the mammalian auditory sensory epithelium. *PLoS Genet.* **13**, 1–23 (2017).

136. Ahmed, M. *et al.* Eya1-Six1 Interaction Is Sufficient to Induce Hair Cell Fate in the Cochlea by Activating Atoh1 Expression in Cooperation with Sox2. *Dev. Cell* **22**, 377–390 (2012).

137. Nagalakshmi, V. K. *et al.* Changes in cell fate determine the regenerative and functional capacity of the developing kidney before and after release of obstruction. *Clin. Sci.* **132**, 2519–2545 (2018).

138. Shepherd, G. M. G. & Corey, D. P. The extent of adaptation in bullfrog saccular hair cells. *J. Neurosci.* **14**, 6217–6229 (1994).

139. Vilfan, A. & Duke, T. Two adaptation processes in auditory hair cells together can provide an active amplifier. *Biophys. J.* **85**, 191–203 (2003).

140. Tinevez, J. Y., Jülicher, F. & Martin, P. Unifying the various incarnations of active hair-bundle motility by the vertebrate hair cell. *Biophys. J.* **93**, 4053–4067 (2007).

141. Beurg, M., Nam, J. H., Crawford, A. & Fettiplace, R. The actions of calcium on hair bundle mechanics in mammalian cochlear hair cells. *Biophys. J.* **94**, 2639–2653 (2008).

142. Kitajiri, S. I. *et al.* Actin-bundling protein TRIOBP forms resilient rootlets of hair cell stereocilia essential for hearing. *Cell* **141**, 786–798 (2010).

143. Assad, J. A. & Corey, D. P. An active motor model for adaptation by vertebrate hair cells. *J. Neurosci.* **12**, 3291–3309 (1992).

144. Holt, J. R. *et al. A Chemical-Genetic Strategy Implicates Myosin-1c in Adaptation by Hair Cells tion is direct: bundle deflections stretch 50 gating springs, which tug open 50-100 cation-selective trans-duction channels within microseconds and without sec-ond-messenger intervention (Corey and Hudspeth, 1983). Although transduction channels open and close sto-1*. *Cell* vol. 108 (2002).

145. Howard, J. & Hudspeth, A. J. Mechanical relaxation of the hair bundle mediates adaptation in mechanoelectrical transduction by the bullfrog's saccular hair cell. *Proc. Natl. Acad. Sci.* **84**, 3064–3068 (1987).

146. Stauffer, E. A. *et al.* Fast adaptation in vestibular hair cells requires Myosin-1c activity. *Neuron* **47**, 541–553 (2005).

147. Kros, C. J. *et al.* Reduced climbing and increased slipping adaptation in cochlear hair cells

of mice with Myo7a mutations. *Nat. Neurosci.* **5**, 41–47 (2002).

148. Marcotti, W. *et al.* Transduction without tip links in cochlear hair cells is mediated by ion channels with permeation properties distinct from those of the mechano-electrical transducer channel. *J. Neurosci.* **34**, 5505–5514 (2014).

149. Wu, Z. *et al.* Mechanosensory hair cells express two molecularly distinct mechanotransduction channels. *Nat. Neurosci.* **20**, 24–33 (2016).

150. Rhodes, C. R. *et al.* A Myo7a mutation cosegrates with stereocilia defects and low-frequency hearing impairment. *Mamm. Genome* **15**, 686–697 (2004).

151. Ricci, a J., Wu, Y. C. & Fettiplace, R. The endogenous calcium buffer and the time course of transducer adaptation in auditory hair cells. *J. Neurosci.* **18**, 8261–77 (1998).

152. Sato, O. *et al.* Human myosin VIIa is a very slow processive motor protein on various cellular actin structures. *J. Biol. Chem.* **292**, 10950–10960 (2017).

153. Heissler, S. M. & Manstein, D. J. Functional characterization of the human myosin-7a motor domain. *Cell. Mol. Life Sci.* **69**, 299–311 (2012).

154. Inoue, A. & Ikebe, M. Characterization of the motor activity of mammalian myosin VIIA. *J. Biol. Chem.* **278**, 5478–5487 (2003).

155. Watanabe, S., Ikebe, R. & Ikebe, M. Drosophila myosin VIIA is a high duty ratio motor with a unique kinetic mechanism. *J. Biol. Chem.* **281**, 7151–7160 (2006).

156. Mentes, A. *et al.* High-resolution cryo-EM structures of actin-bound myosin states reveal the mechanism of myosin force sensing. *Proc. Natl. Acad. Sci. U. S. A.* **115**, 1292–1297 (2018).

157. Kawashima, Y. *et al.* Mechanotransduction in mouse inner ear hair cells requires

transmembrane channel – like genes. *J. Clin. Invest.* **121**, 4796–4809 (2011).